

## A REVIEW OF FLIGHT SIMULATION TECHNIQUES

MAX BAARSPUL

*Delft University of Technology, Faculty of Aerospace Engineering,  
Kluyverweg 1, 2629 HS Delft, The Netherlands*

(Received 9 August 1989)

**Abstract**—After a brief historical review of the evolution of flight simulation techniques, this paper first deals with the main areas of flight simulator applications. Next, it describes the main components of a piloted flight simulator. Because of the presence of the pilot-in-the-loop, the digital computer driving the simulator must solve the aircraft equations of motion in 'real-time'. Solutions to meet the high required computer power of todays modern flight simulator are elaborated.

The physical similarity between aircraft and simulator in cockpit layout, flight instruments, flying controls etc., is discussed, based on the equipment and environmental cue fidelity required for training and research simulators.

Visual systems play an increasingly important role in piloted flight simulation. The visual systems now available and most widely used are described, where image generators and display devices will be distinguished. The characteristics of out-of-the-window visual simulation systems pertaining to the perceptual capabilities of human vision are discussed.

Faithful reproduction of aircraft motion requires large travel, velocity and acceleration capabilities of the motion system. Different types and applications of motion systems in e.g. airline training and research are described.

The principles of motion cue generation, based on the characteristics of the non-visual human motion sensors, are described. The complete motion system, consisting of the hardware and the motion drive software, is discussed. The principles of mathematical modelling of the aerodynamic, flight control, propulsion, landing gear and environmental characteristics of the aircraft are reviewed. An example of the identification of an aircraft mathematical model, based on flight and taxi tests, is presented.

Finally, the paper deals with the hardware and software integration of the flight simulator components and the testing and acceptance of the complete flight simulator. Examples of the so-called 'Computer Generated Checkout' and 'Proof of Match' are presented.

The concluding remarks briefly summarize the status of flight simulator technology and consider possibilities for future research.

## CONTENTS

|  |    |
|--|----|
| NOTATION   | 2  |
| ACRONYMS   | 5  |
| REFERENCE FRAMES   | 5  |
| 1. INTRODUCTION  | 6  |
| 2. HISTORY OF FLIGHT SIMULATION  | 6  |
| 3. FLIGHT SIMULATOR APPLICATIONS   | 16 |
| 3.1. General   | 16 |
| 3.2. Training simulators   | 17 |
| 3.3. Research and development simulators   | 18 |
| 3.3.1. Ground-based facilities   | 18 |
| 3.3.2. In-flight simulators  | 23 |
| 4. MAIN COMPONENTS OF A PILOTED FLIGHT SIMULATOR   | 25 |
| 4.1. General   | 25 |
| 4.2. Real-time digital computer  | 25 |
| 4.3. The flight simulator cockpit  | 31 |
| 4.4. Visual systems  | 33 |
| 4.5. Motion systems  | 37 |
| 5. MATHEMATICAL MODELS FOR FLIGHT SIMULATION   | 40 |
| 5.1. General   | 40 |
| 5.2. Equations of motion of an airplane  | 40 |
| 5.2.1. Small perturbation equations  | 41 |
| 5.2.2. Non-linear equations covering the complete flight envelope                              | 43 |
| 5.3. Mathematical modelling of flight in turbulence and windshear                              | 51 |
| 5.3.1. Coupling of the patchy turbulence simulation and the mathematical model of the airplane | 71 |
| 5.3.2. Wind shear and wind profiles  | 71 |
| 5.4. Ground handling   | 75 |
| 5.4.1. Transformation of the landing gear forces to body axes                                  | 79 |

|  |     |
|--|-----|
| 5.5. Mathematical model identification, based on flight and taxi tests | 80  |
| 5.5.1. A priori models   | 81  |
| 5.5.2. Flight test measurement system                                  | 83  |
| 5.5.3. Flight test program   | 84  |
| 5.5.4. System identification techniques                                | 84  |
| 5.5.5. Flight test data analysis                                       | 86  |
| 5.5.6. Final models  | 88  |
| 5.5.7. Evaluation and testing of the final models                      | 93  |
| 6. OUT-OF-THE-WINDOW VISUAL SIMULATION                                 | 96  |
| 6.1. General   | 96  |
| 6.2. Visual simulation system characteristics                          | 98  |
| 7. MOTION CUE GENERATION   | 104 |
| 7.1. General   | 104 |
| 7.2. Dynamic characteristics of the motion system hardware             | 105 |
| 7.3. Motion drive commands controlling simulator cockpit motion        | 108 |
| 7.4. Special motion effects  | 113 |
| 8. FLIGHT SIMULATOR INTEGRATION, TESTING AND ACCEPTANCE                | 113 |
| 8.1. General   | 113 |
| 8.2. Approval Test Guide (ATG)   | 114 |
| 8.3. Computer Generated Checkout (CGC)                                 | 115 |
| 8.4. Proof of Match (POM)  | 115 |
| 8.5. Flight Simulator Critical Maneuvers (FSCM)                        | 116 |
| 9. CONCLUDING REMARKS  | 116 |
| ACKNOWLEDGEMENTS   | 117 |
| REFERENCES   | 117 |

## NOTATION

|   |   |
|---|---|
| $a$ —acceleration   | $C_L = L/(1/2\rho V^2 S)$ lift coefficient, three dimensional flow  |
| $a$ —engine model parameter   |   |
| $a$ —constant depending on runway-condition   | $C_{L_a} = dC_L/d\alpha$ derivative of the lift coefficient with respect to angle of attack, three-dimensional flow |
| a.c.—aerodynamic center   |   |
| $a(t)$ —stochastic process, output of filter $F_a$ (Fig. 46)  | $C_{l_s} = C_L$ due to turbulence   |
| $A = b^2/S$ wing aspect ratio   | $C_{l_p} = \partial C_L / \partial (pb/2V)$   |
| $A_x, A_y, A_z$ —specific force along $X$ -, $Y$ - and $Z$ -axis respectively   | $C_{l_{p_w}} = \text{contribution to } C_{l_p} \text{ due to the wing}$   |
| $b$ —wing span  | $C_{l_r} = \partial C_L / \partial (rb/2V)$   |
| $b$ —engine model parameter   | $C_{l_{r_w}} = \text{contribution to } C_{l_r} \text{ due to the wing}$   |
| $b$ —tyre-width   | $C_{l_\beta} = \partial C_L / \partial \beta$   |
| $b(t)$ —stochastic process, output of filter $F_b$ (Fig. 46)  | $C_{l_\delta} = \partial C_L / \partial \delta$   |
| $B = b/2L_g$  | $C_{l_{\delta_a}} = \partial C_L / \partial \delta_a$   |
| $c$ —local wing chord   | $C_{l_{\delta_r}} = \partial C_L / \partial \delta_r$   |
| $c_f$ —chord wing flap  | $C_m = M/(1/2\rho V^2 S\bar{c})$ coefficient of the aerodynamic moment about the $y$ -axis, three-dimensional flow  |
| $c_{a, e, r, t}$ —chord of aileron, elevator, rudder or tab, aft of hinge line  | $C_{m_{a.c.}} = \text{coefficient of the moment about the aerodynamic center, three-dimensional flow}$              |
| $c_r$ —chord length in the plane of symmetry  | $C_{m_g} = C_m$ due to turbulence   |
| $c_t$ —chord length at wing tip   | $C_{m_h} = \text{contribution of the horizontal tail to } C_m$  |
| $c(t)$ —stochastic process, output of filter $F_c$ (Fig. 46)  | $C_{m_q} = \partial C_m / \partial (q\bar{c}/V)$  |
| $c_v$ —strut damping constant   | $C_{m_u} = 1/(1/2\rho VS\bar{c}) \cdot \partial M/\partial u$   |
| $\bar{c} = 2/S \int_0^{b/2} c^2 dy$ mean aerodynamic chord (m.a.c.)   | $C_{m_{u_s}} = 1/(1/2\rho V^2 S) \cdot \partial M_\theta / \partial \hat{u}_s$                                      |
| $\bar{c}_{w, h, v}$ —mean aerodynamic chord of wing, horizontal tailplane, or vertical tailplane  | $C_{m_{\hat{u}_s}} = \partial C_m / \partial (\hat{u}_s \bar{c}/V)$   |
| $\bar{c}_{a, e, r, t}$ —mean aerodynamic chord of control surfaces and tabs, aft of hinge line  | $C_{m_w} = \text{contribution to } C_m \text{ due to the wing plus fuselage}$                                       |
| $C$ —rate of climb  | $C_{m_0} = C_m \text{ at } C_L = \delta_e = 0$  |
| $C_D = D/(1/2\rho V^2 S)$ drag coefficient, three-dimensional flow  | $C_{m_{\alpha_{fix}}} = \partial C_m / \partial \alpha \text{ at } \delta_e = \text{constant}$                      |
| $c.g.$ —center of gravity   | $C_{m_{\alpha_{free}}} = \partial C_m / \partial \alpha \text{ at } F_e = 0$  |
| $C_{he} = H_e / (1/2\rho V_h^2 S_e \bar{c}_e)$ hinge moment coefficient of the elevator. The indices $a$ , $r$ or $t$ are used to indicate the hinge moment coefficients of the aileron, the rudder or a tab respectively | $C_{m_{\dot{\alpha}}} = \partial C_m / \partial (\dot{\alpha}\bar{c}/V)$  |
| $C_I = L/(1/2\rho V^2 Sb)$ coefficient of the aerodynamic moment about the $x$ -axis, three dimensional flow  | $C_{m_{\alpha_s}} = \partial C_m / \partial \alpha_g$   |
|   | $C_{m_{\dot{\alpha}_s}} = \partial C_m / \partial (\dot{\alpha}_g \bar{c}/V)$                                       |
|   | $C_{m_{\delta}} = \partial C_m / \partial \delta_e$ elevator effectivity  |
|   | $C_{m_{\delta_t}} = \partial C_m / \partial \delta_r$   |
|   | $C_{m_{\Delta p}} = \partial C_m / \partial (\Delta p_t / 1/2\rho V^2)$   |
|   | $C_n = N/(1/2\rho V^2 Sb)$ yawing moment coefficient  |
|   | $C_{n_g} = C_n$ due to turbulence   |
|   | $C_{n_p} = \partial C_n / \partial (pb/2V)$   |





|  |   |
|--|---|
| e—earth reference frame                                    | r—rudder                                  |
| e—elevator   | r—root of the wing                        |
| f—flap   | R—right gear                              |
| f—fuselage   | s—spring in the control mechanism         |
| fix— $\delta_e$ = constant                                 | s—stability reference frame               |
| free— $F_e = 0$ ( $C_{h_e} = 0$ )                          | t—tip                                     |
| h—horizontal tailplane                                     | t—trim tab                                |
| h—heading attached aircraft carried vertical axes<br>frame | T—tailwheel                               |
| i—inertia reference frame                                  | v—vertical tailplane                      |
| L—left gear  | w—static unbalance                        |
| l—landing gear   | w—wing or wing with fuselage and nacelles |
| mo—model axes frame  | x—along the X-axis                        |
| M—measurement reference frame                              | y—along the Y-axis                        |
| p—relating to the propulsive system                        | z—along the Z-axis                        |
|  | 0—initial, steady flight condition        |

## ACRONYMS

|  |   |
|--|---|
| ADA—modern computer language (standard software of U.S. DoD)           | FMS—flight management system                        |
| AEEC—Airlines Electronic Engineering Committee                         | FSAA—flight simulator for advanced aircraft         |
| AMUX—ARINC multiplexer   | FSCM—flight simulator critical maneuver             |
| AOM—aircraft operating manual  | IATA—International Air Transport Association        |
| ARINC—Aeronautical Radio Inc.  | IRS—inertial reference system                       |
| ATC—air traffic control  | MFLOPS—million floating point operations per second |
| ATG—approval test guide  | NASA—National Aeronautics and Space Administration  |
| ATM—acceptance test manual   | NLR—National Aerospace Laboratory                   |
| CAE—Canadian Aviation Electronics Ltd                                  | RAE—Royal Aircraft Establishment                    |
| CAT—clear air turbulence   | RLS—Government Civil Aviation School                |
| CGI—computer generated image   | RMDU—remote multiplexer digitizer unit              |
| CGC—computer generated checkout  | RSIS—rotorcraft system integration simulator        |
| CPU—central processing unit  | SST—supersonic transport                            |
| CRT—cathode ray tube   | STOVL—short take-off vertical landing               |
| DFVLR—Deutsche Forschungs- und Versuchsanstalt für Luft- und Raumfahrt | TAS—true air speed                                  |
| DHC—De Havilland of Canada   | TIFS—total in-flight simulator                      |
| DME—distance measuring equipment                                       | U.K.—United Kingdom                                 |
| DOF—degrees-of-freedom   | U.S.A.—United States of America                     |
| DUT—Delft University of Technology                                     | USAF—United States Air Force                        |
| EFIS—electronic flight instrument system                               | USN—United States Navy                              |
| FAA—Federal Aviation Administration                                    | VMS—vertical motion simulator                       |
|  | VSTOL—vertical, short take-off and landing          |

## REFERENCE FRAMES

**Body axes frame,  $F_b(O_b, X_b, Y_b, Z_b)$** —This is an aircraft-fixed, right-handed reference frame with the origin in the center of gravity of the airplane, see Fig. 61. The  $X_b$ -axis is in the plane of symmetry, parallel to the centerline of the cylindrical part of the fuselage (which is parallel to the cabin floor) and is defined positive in the forward direction. The  $Z_b$ -axis is in the plane of symmetry, perpendicular to the  $X_b$ -axis and positive pointing downward. The  $Y_b$ -axis is perpendicular to the  $X_b, Z_b$ -plane, positive to the right (starboard).

**Stability axes frame,  $F_s(O_s, X_s, Y_s, Z_s)$** —This is an aircraft fixed system defined as the body axes frame with the difference that the  $X_s$ -axis coincides with the velocity vector of the center of gravity projected on the  $X_s, Z_s$ -plane in a reference flight condition.

**Earth axes reference frame,  $F_e(O_e, X_e, Y_e, Z_e)$** —This right handed frame has its origin fixed relative to the earth, coinciding with the

airplane's center of gravity at the start of the motion studied. The positive  $Z_e$ -axis points to the center of the earth. The  $X_e$ -axis is perpendicular to the  $Z_e$ -axis, positive to North. The  $Y_e$ -axis is perpendicular to the  $X_e, Z_e$ -plane, positive to the East.

**Model axes frame,  $F_{mo}(O_{mo}, X_{mo}, Y_{mo}, Z_{mo})$** —This is a reference frame, which is not body-fixed. The origin is situated in the center of gravity of the aircraft. The  $X_{mo}$ -axis coincides with the projection of the velocity vector of the center of mass on the plane of symmetry and is defined positive forward. The other two axes are defined as in the stability axes frame.

**Heading attached aircraft carried vertical axis frame,  $F_h(O_h, X_h, Y_h, Z_h)$** —This frame has its origin in the center of gravity of the aircraft. The  $Z_h$ -axis coincides with the local g-vector. The  $X_h$ -axis is perpendicular to the  $Z_h$ -axis and is defined as the projection of the airplane's longitudinal body axis on the horizontal plane (see Fig. 60). The  $Y_h$ -

axis is perpendicular to the  $X_hZ_h$ -plane, positive in the direction of the right wing.

*Measurement axes frame,  $F_M(O_M, X_M, Y_M, Z_M)$* —This is an aircraft fixed, *left-handed* orthogonal reference frame (see Fig. 61). The origin  $O_M$  lies in a point resulting from the perpendicular projection of the foremost point of the wing chord, parallel to the aircraft's plane of symmetry, situated in the starboard wing 1.400 m from the aircraft's plane of symmetry, on this plane of symmetry. The  $X_MO_MZ_M$ -plane coincides with this plane of symmetry and the

$X_M$ -axis points rearward. The positive  $Y_M$ -axis points to the left and the positive  $Z_M$ -axis points upwards.

*Inertial reference frame,  $(O_i, X_i, Y_i, Z_i)$* —This is a Newtonian frame with the origin situated in the earth center. The  $Z_i$ -axis coincides with the rotation axis of the earth, positive in the direction of the North Pole. The  $X_i$ -axis lies in the equatorial plane perpendicular to the  $Z_i$ -axis. The  $Y_i$ -axis is perpendicular to the  $X_iZ_i$ -plane, positive according to a right-handed system.

## 1. INTRODUCTION

When reviewing the progress in aerospace science with regard to the evolution of flight simulation techniques, huge advances can be observed in the research and application of flight simulation since the bellows-driven 'Link' Trainer.

The purpose of flight simulation in the context of this paper, is to reproduce on the ground the behavior of an aircraft in flight, as sensed by the pilot. The objective of this article is to provide an overview of the techniques used in flight simulation.

Subjective fidelity, or a sense of realism in the flight simulator is essential for productive use in the subsequent four main areas of flight simulator applications:

- flight crew training;
- research on the man-machine interface;
- aircraft and equipment design, development, test and evaluation;
- licensing, certification and accident investigations.

The creation of subjective fidelity requires varying degrees of engineering similarity to the actual flight situation, depending on the task and the objectives of the simulator application. Dynamic mathematical models of the aerodynamic, propulsion and inertia characteristics of the aircraft can now be implemented in order to represent actual aircraft in-flight characteristics. Cockpit displays and controls can be faithfully duplicated. However, in two main areas of aircraft-state feedback to the pilot, the ground-based flight simulator can never actually duplicate the aircraft's behavior in flight. These are the generation of:

- the visual scenery of the outside world;
- the simulator cockpit motion.

As a consequence an engineering compromise for visual and motion cueing is inevitable.

In addition to the description of flight simulator applications and the main components of a piloted flight simulator, the paper presents a review of flight simulation techniques, i.e.

- mathematical modelling for flight simulation;
- out-of-the-window visual simulation;
- motion cue generation;
- flight simulator integration, testing and acceptance.

The paper will be restricted to mainly civil applications of fixed wing airplane simulation.

## 2. HISTORY OF FLIGHT SIMULATION

Since the beginning of manned flight, the importance of pilot training has been realized. The pilots of the first powered airplanes trained by proceeding through a graded sequence of exercises on real aircraft. After some familiarization flights, as a passenger, a student would attempt taxiing, using a low powered machine enabling rudder control to be practiced. Next, he would graduate to a higher powered aircraft and would first make short

hops using elevator and aileron control. After longer hops, he would eventually achieve flight. The following presentation on the evolution of the ground-based flight simulator is based largely on Ref. 1.

The first proposals for truly ground-based trainers were based on aircraft attached to the ground, but capable of responding to aerodynamic forces. The 'Sanders Teacher' (1910) was an example of such a device. It was an aircraft mounted on a universal joint in an exposed position and facing into the prevailing wind. As an actual airplane of the type, it was able to respond in attitude to the elevator, aileron and rudder controls. Unfortunately, because of the unreliability and irregular nature of the wind, the 'Sanders Teacher' and many similar devices (Billing,<sup>(6)</sup> see Fig. 1; Gabardini<sup>(2)</sup>) were not very successful.

The first truly synthetic flight training device, the Antoinette trainer (Fig. 2), consisted of two half-sections of a barrel. The device was moved manually by instructors to present the pitch and roll motion of an airplane. The prospective pilot, sitting in the top-section, was required to line up a reference bar with the horizon, using his controls.

The replacement of the human actuators in Antoinette type machines with mechanical or electrical actuators, linked to the trainer controls, was the next step in the evolution of the synthetic flight trainer. These actuators rotate the fuselage of the trainer into an attitude corresponding with that of the real aircraft in response to the pilot's control inputs. Usually a provision was made for an instructor to introduce disturbances, to simulate the effect of turbulence, and to present control problems to the student. The Link Trainer was, of course,

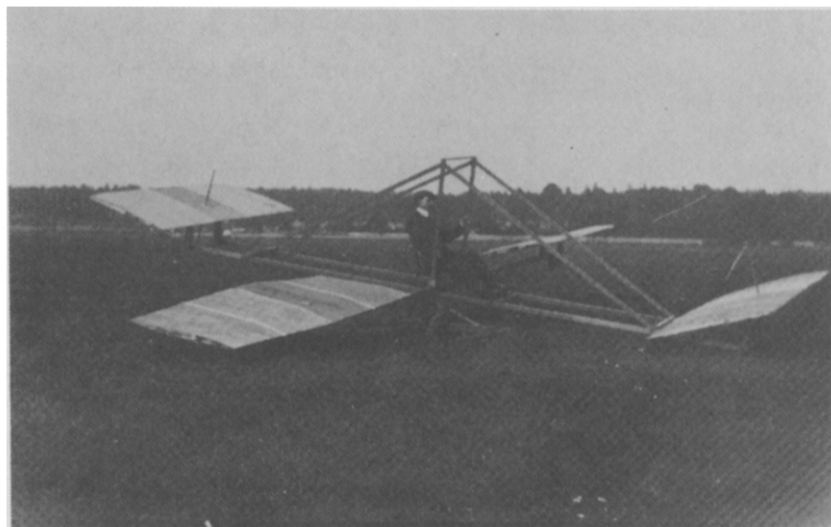


FIG. 1. A trainer of the Billing type. Reproduced with permission from Cambridge University Press, U.K.



FIG. 2. Antoinette trainer. Reproduced with permission from Cambridge University Press, U.K.

the most successful and well-known device of this type. Its designer, Edwin Link, gained his early engineering experience with his father's firm, the Link Piano and Organ Company of Binghamton, New York. The trainer was developed in the period 1927–1929 in the basement of the Link factory and made use of pneumatic mechanisms, familiar in the organ business. The first Link Trainer, advertized as an "efficient aeronautical training aid", was described in a patent filed in 1930.<sup>(15)</sup> Roll, pitch and yaw movements were initiated using pneumatic bellows for actuation. The various control valves, operated by the stick and rudder, were fed by an electrically driven suction pump, mounted in a fixed base. Another motor-driven device produced a repeated sequence of attitude disturbances. The performance of the trainer was adjusted by trial and error until a satisfactory 'feel' was obtained. Figure 3 presents an illustration of the Link Trainer in one of its later forms. The first description of the trainer made no reference to flight instruments and the simulated effects of the ailerons, elevator and rudder were independent. They did not represent the interactions of an aircraft's coordinated behavior. The Link Trainers were soon being fitted with 'flight' instruments as standard equipment.

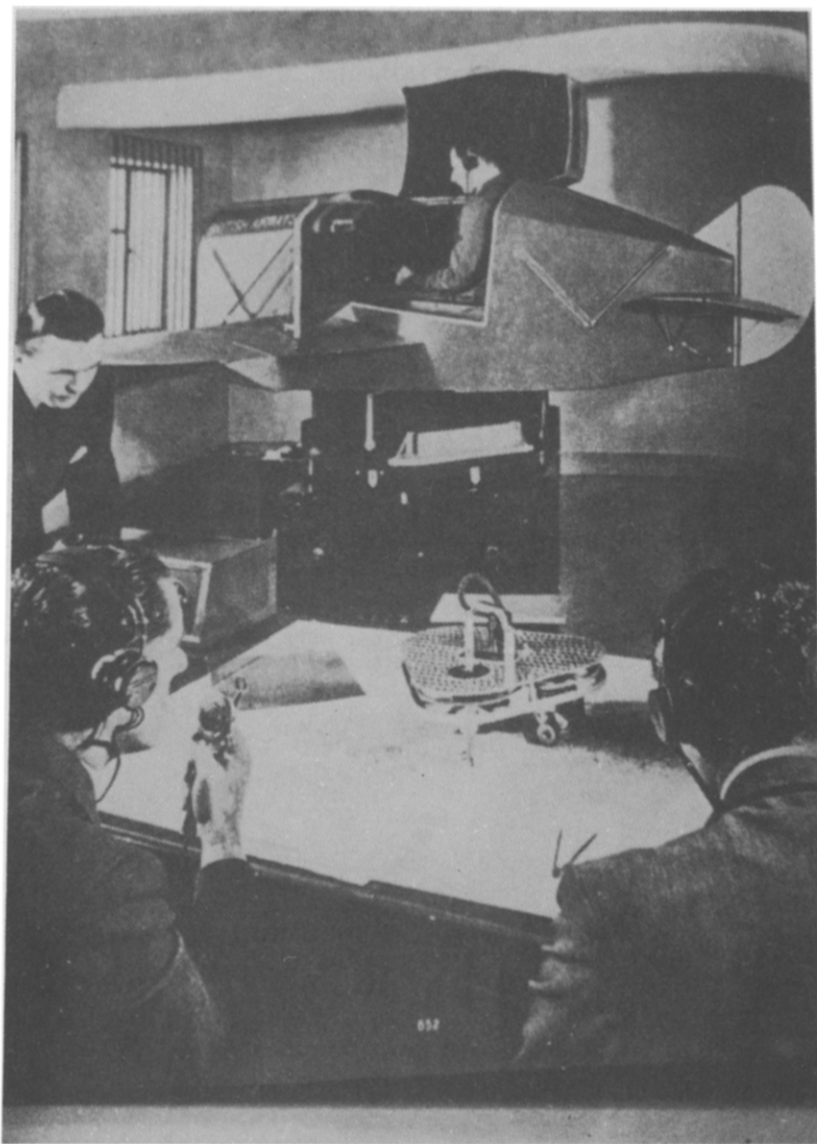


FIG. 3. Link-trainer, showing 'Crab' plotter. Reprinted with permission from Cambridge University Press, U.K.

In the early 1930s blind flying training was started by the Link Flying School. As the importance of this type of training was fully realized, the sales of Link Trainers increased.

The newer versions of the Link Trainer were able to rotate in yaw through 360 degrees, which allowed a magnetic compass to be installed. The various instruments were operated either mechanically or pneumatically. Altitude, for example, was represented by the pressure of air in a tank, directly connected to an altimeter. The interaction of rudder and ailerons was provided in the more advanced trainers, as was a stall feature. However, the simulation of aircraft behavior was still achieved in an empirical way. The benefit of the trainers was further increased with the attachment of a course plotter, to enable the instructor to monitor the maneuvers of the student inside the trainer. This well-known 'crab' device, which was self-propelled and steerable, traced the course of the simulated flight on a chart by an inked wheel. The instructor was able to manually control the transmission of simulated radio beacon signals to the trainer, by relating the position of the student's aircraft to marks on the chart.

The 1930s were certainly the years of the Link Trainer. It was produced in various versions and was exported to many countries, including the U.S.S.R., Japan, France and Germany.

In 1937, the first Link Trainer to be sold to an airline was one delivered to American Airlines. In that year, the Royal Air Force (RAF) in Britain also took delivery of their first Link Trainer. By the beginning of the Second World War, many of the major air forces were doing their basic instrument flight training on 'Links' or derivatives.

Developments in aircraft, such as variable pitch propellers, retractable landing gears and higher speeds, made training in cockpit drill essential.<sup>(4)</sup> The mock-up fuselage was introduced as an aid to training in these procedures. One such device was the Hawarden Trainer, made of the centre section of a Spitfire, which enabled training in the procedures of a complete operational flight.<sup>(3)</sup> The Link Trainers too, were developed to the stage where the instrument layout of specific airplanes was duplicated. The U.S. Army–Navy Trainer, Model 18 (ANT-18), for example, was designed for introduction to flying in 'Harvard' (AT-6 and SNJ) aircraft.

In 1939 the British requested Link to design a trainer, which could be used to improve the celestial navigation capabilities of their crews, who were ferrying 'surplus' U.S. aircraft across the Atlantic. This trainer could also be used to improve bombing accuracy during night raids over Europe.<sup>(14)</sup> Edwin Link, together with the aerial navigation expert, P. Weems, worked out the design of a large trainer, suitable for use by an entire bomber crew. This was the Celestial Navigation Trainer to be located inside a 45 foot high silo-shaped building (Fig. 4). This trainer incorporated a larger version of the conventional Link Trainer fuselage, which could accommodate the pilot, navigator and bomber. The pilot flew the trainer, which included all the normal Link facilities, and instruments. A bomb aimer's station provided the appropriate sight and an image of targets over which the trainer 'flew'. The navigator was provided with radio aids and, in addition, was provided with a very elaborate celestial view from which he could take his 'astro sights'. The 'stars', of which twelve were collimated, were fixed to a dome which was given a movement to correspond with the apparent motion of the stars with time and with changes in the bomber's longitude and latitude.

The first Celestial Navigation Trainer was completed in 1941, and the RAF placed an order for sixty, of which only a limited number were installed. Hundreds of these devices, however, were installed and operated in the U.S.A.<sup>(16)</sup>

Throughout the war many 'home-made' devices for training were constructed, as a consequence of the long delivery times and low priority given to the manufacture of training aids. An early development was the 'instructional fuselage' of a certain type, mounted on stands inside a hangar. All the hydraulic, electric, and pneumatic services, and their recording instruments were made to work in the normal manner, so the various drills carried out by the crew during training, were realistic.

The so-called 'Silloth Trainer' was an example of this type of device, which had a broader success (Fig. 5). The basic flying behavior, and all engines, electrical and hydraulic systems

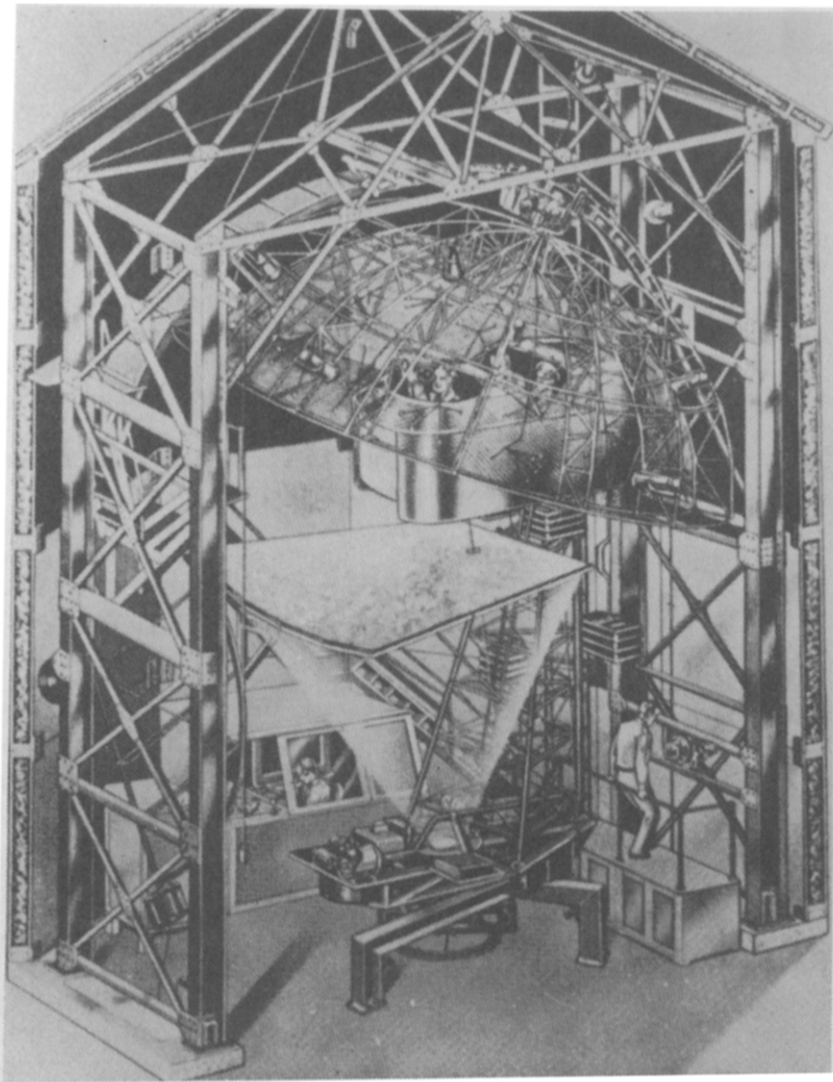


FIG. 4. The celestial navigation trainer. Reprinted with permission from Cambridge University Press, U.K.

were simulated and sounds were generated. An instructors panel (Fig. 5) was provided to enable monitoring the crew and insertion of malfunctions. Like the Link Trainer, all computation was pneumatic. Silloth Trainers were manufactured for many types of 2- and 4-engined aircraft throughout the war, while 14 were in existence or on order in 1945.

During World War II, a major advance in simulation was the use of a type of analogue computer, the differential analyzer, to solve the equations of motion of an aircraft. These analogue computers enabled simulation of the aircraft response to aerodynamic forces as opposed to an empirical reproduction of these effects.

The first known discussion on the computer method for flight simulation is that of H. A. Roeder in his German Patent Specification in 1929. Roeder treated the general problem of the control by instruments of vehicles, freely moveable in space, such as airplanes, airships and submarines. His outlines of the requirements of a simulator for such a task could almost refer to a modern flight simulator (Fig. 6). As an example of this technique, Roeder described the dynamic simulation of an airship height control system, using a fluid operated analogue computer. Figure 6 shows the interaction of variables in a dynamic model of an aircraft. No successful training devices are known to have resulted from this work.

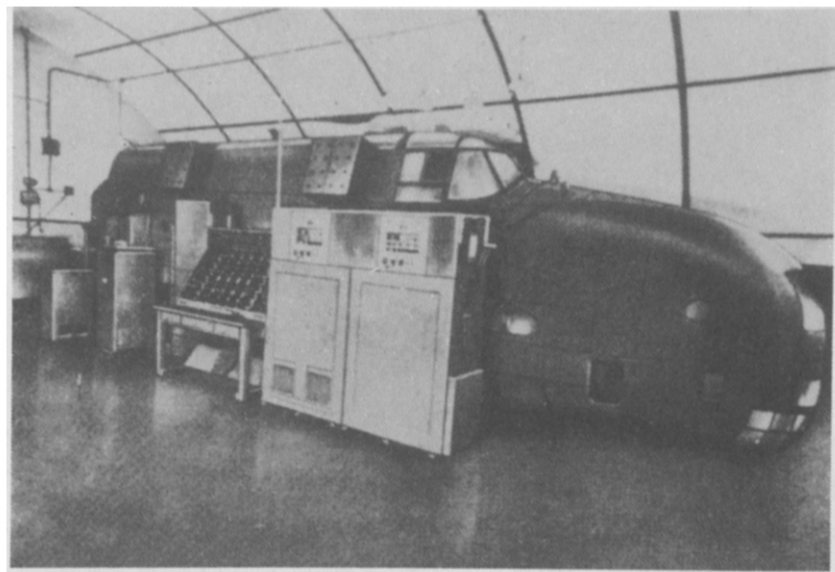


FIG. 5. A Silloth trainer for a Halifax aircraft. Reprinted with permission from Cambridge University Press, U.K.

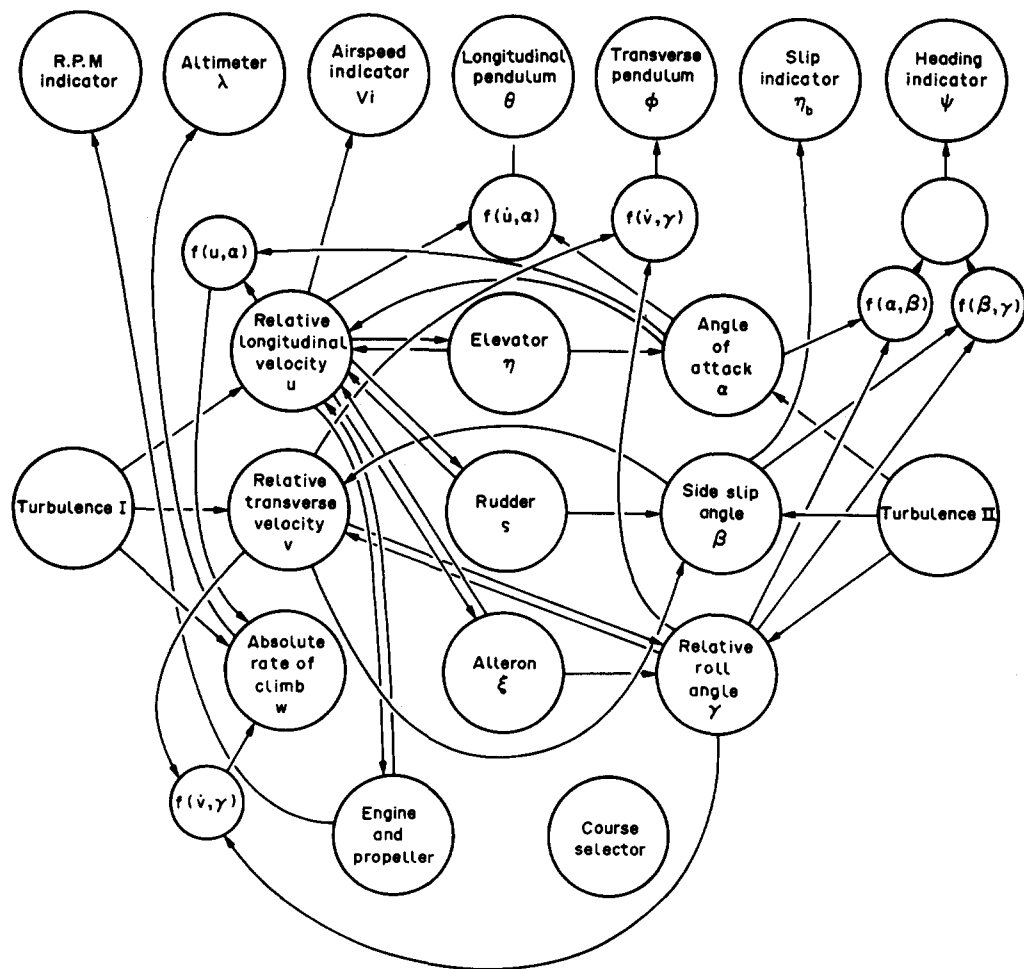


FIG. 6. Roeder's aeroplane model. Reprinted with permission from Cambridge University Press, U.K.

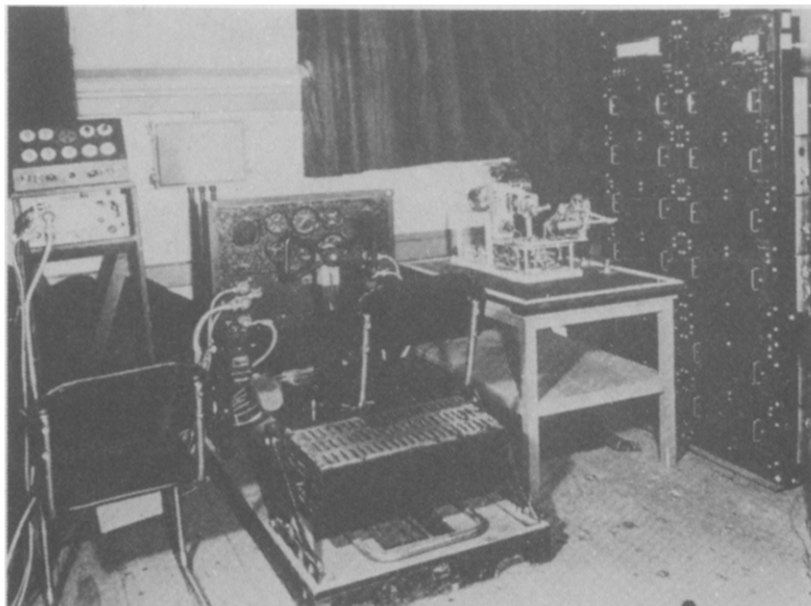


FIG. 7. A TRE flying unit. Reprinted with permission from Cambridge University Press, U.K.

At the Telecommunications Research Establishment (TRE) in Britain, an electronic simulator, which solved aircraft equations of motion, was designed and built in 1941 (Fig. 7). This simulator was the 'flying unit' for the TRE aerial interception radar trainers.<sup>(9)</sup> Dynatron Radio Ltd constructed the first model of the analogue (d.c.) computer of the trainer and many were used throughout the war.

Also in 1941 a U.S. Navy commander wrote a "Report on British Synthetic Training".<sup>(11)</sup> This highly significant report led to the establishment of the Special Devices Division of the Bureau of Aeronautics, the forerunner of the present Naval Training Equipment Center.<sup>(17)</sup> In the same year the Silloth Trainer concept was brought to the U.S., but after evaluation it was decided to build an electrical version of this trainer. The new trainer was produced by Bell Telephone Laboratories for the Navy's PBM-3 aircraft. A total of 32 of these electronic flight trainers for seven aircraft types were built by Bell and the Western Electric Company during the war.

After the development of his electrical flight trainer,<sup>(8)</sup> Dr R. C. Dehmel, an engineer of Bell, applied analogue computing techniques to the design of an instrument flight simulator. This trainer, called the Z-1 (Fig. 8) was manufactured by Curtiss-Wright for the AT-6 aircraft. The U.S. Air Force ordered two of them and these were followed by production examples, indicated as the Z-2, Z-3 and Z-4.

Competition from Curtiss-Wright stimulated Link to develop his own electronic simulators after World War II. It was argued in those days, that the modern pilot should not fly "by the seat of his pants", but by instruments.<sup>(14)</sup> Edward Link disagreed with this idea and held the view that trainer motion was needed, even if incorrect, since motion was present in flying. Customer pressure caused Link, however, to follow the trend to fixed-base flight simulators. Therefore, the company developed their own electronic analogue computer, which was used in their C-11 jet trainer (Fig. 9). In 1949, the U.S. Air Force awarded a contract, and over a thousand of these trainers were produced and sold.

In the mean time, Pan American Airways had contracted Curtiss-Wright to develop a full simulator for its Boeing 377 Strato Cruisers. This flight simulator, installed in 1948, was the first full aircraft simulator to be owned by an airline. No motion or visual systems were installed, but in all other respects the simulator duplicated the appearance and behavior of the Boeing 377 cockpit. This forerunner of present day procedure trainers was especially useful to practice emergency conditions and also complete routes could be flown, using the same navigational aids as in real flight.

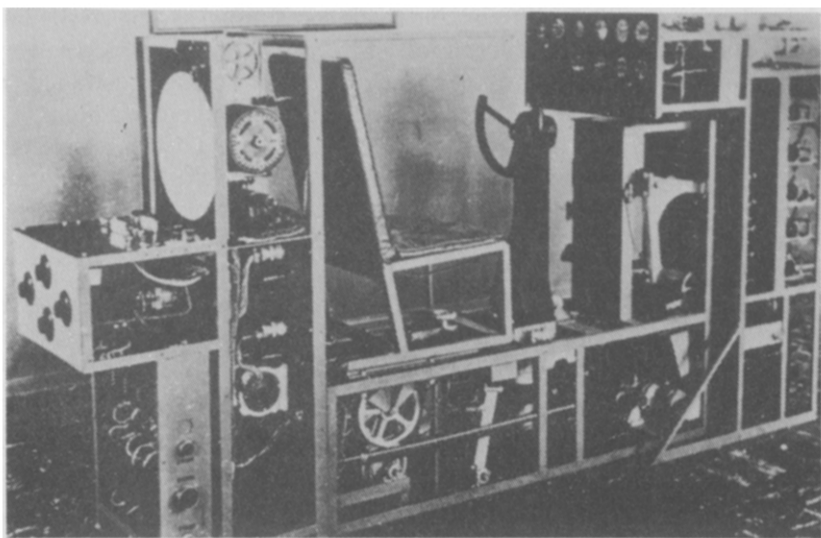


FIG. 8. A Curtiss-Wright Z-1 without cover. Reprinted with permission from Cambridge University Press, U.K.

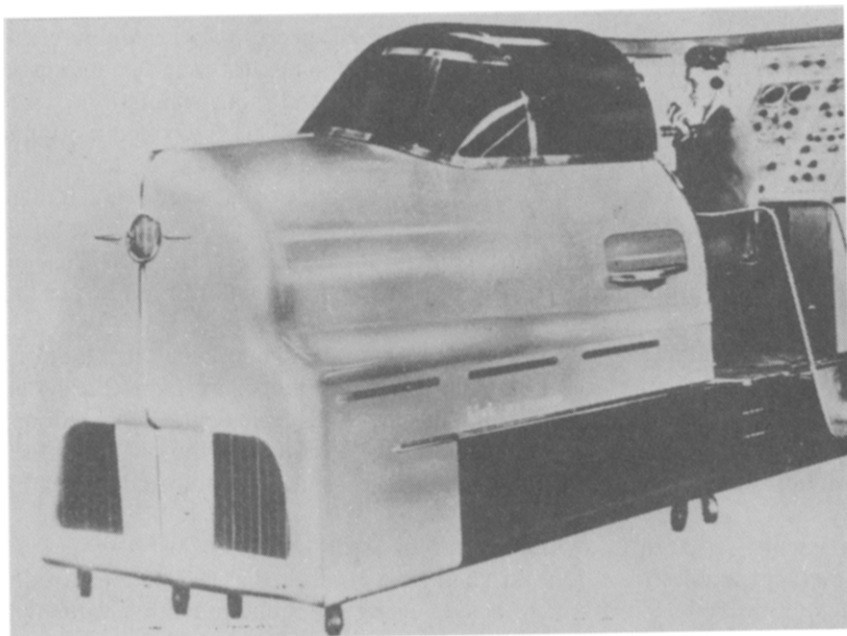


FIG. 9. A Link C-11. Reprinted with permission from Cambridge University Press, U.K.

A similar simulator was built for BOAC by Rediffusion (Redifon) in Britain, under license to Curtiss-Wright. Before the final acceptance of the Strato Cruiser simulator in 1951, Rediffusion received an order to build a Comet I simulator for BOAC. This was to become the first jet transport simulator in the world.

One of the restrictions in flight simulation in the early 1950s was that aircraft manufacturers did not have much analytical information on the performance and dynamic characteristics of their airframes and engines. The simulator manufacturers were therefore required to use trial and error methods and pilot evaluations, to make the simulator 'fly' as much as possible like the aircraft. This situation changed fortunately, when more and more data became available from flight testing programmes. Later on, even special flight tests were carried out, to generate a flight simulator data-base.

Together with requirements for driving the motion and visual systems being introduced, and pressure from the operators for improved accuracy (resulting hopefully in better transfer of training), significant increases in the amount of analogue computer hardware became necessary. However, the cumulative errors of all this interacting circuitry exceeded the improved accuracy implied by the data now available. Also a decrease in reliability was observed, despite improved component technology. The latter effect was multiplied by the increased utilization of simulators for training (at that time typically 8–10 hr per day for 5 days per week).

From the earliest days of programmable electronic digital computers, it was realized that a potential application would be in real-time digital simulation. The second generation of digital computers, introduced in the early 1950s, had the potential of solving the accuracy and reliability problems of their complex analogue counterparts. In 1950, the U.S. Navy initiated a research program on real-time digital simulation at the University of Pennsylvania. The Universal Digital Operational Flight Trainer (UDOFT), the computer of which was manufactured by the Sylvania Corporation, resulted from this research program and was completed in 1960. The UDOFT project demonstrated the flexibility of real-time digital simulation.

In the early 1960s Link developed a special purpose digital computer, the Link Mark I, designed for real-time simulation. This computer had three parallel processors for arithmetic, function generation, and radio station selection. In the late 1960s general purpose computers, designed for process control applications, were found to be also suitable for real-time simulation. As a result, the use of special purpose computers declined. Today special purpose digital computers are only used in applications demanding very high speed processing, such as computer image generation and radar simulation.

Up to the mid 1950s, nearly all the simulators produced had no cockpit motion systems. This was often justified by the statement—as mentioned before—that modern pilots did not fly “by the seat of their pants”. However, the fact remained that fixed-base simulators did not ‘fly’ like airplanes. The lack of motion was partly compensated by adjustment of the aircraft dynamics simulation and the control loading characteristics. The simulator manufacturers made proposals for motion systems, but it was not until the late 1950s that the airlines decided to purchase them.

Rediffusion received a contract from BOAC for the production of a pitch motion system, as part of a Comet IV simulator in 1958 (Fig. 10). Later more complex motion systems were developed, capable of producing motions in two- and three-degrees-of-freedom (DOF). With the introduction of large wide-body transport aircraft, like the 747, lateral simulator cockpit motion was required, which led to the development of four- and six DOF motion systems.

At the Faculty of Aerospace Engineering of Delft University of Technology (DUT), research on flight simulator motion started in 1964. It resulted in 1969 in the introduction of a 3 DOF motion system (roll, pitch, heave), using hydraulic actuators with hydrostatic bearings.<sup>(5)</sup> It was the first motion system using this now well-known and accepted technique to improve the dynamic characteristics of motion systems. Responsibility for the design of this motion system (Fig. 11) was with the Faculty of Mechanical Engineering of DUT, where T. J. Viersma<sup>(19)</sup> and P. Blok<sup>(7)</sup> started development work on hydrostatic bearings for this application in 1966. Results of these efforts are reported in Viersma and Baarspul.<sup>(20)</sup> The first commercially available 6 DOF motion system, using hydraulic actuators with hydrostatic bearings, was developed by LMT (Thompson CSF) in 1977.

Visual systems to simulate the out-of-the-window visual scene have been proposed and constructed for almost as long as flight simulators. Realistic and flexible visual attachments, however, are a fairly recent development. Due to the large number of visual systems which have been developed, only the most commonly applied types will be mentioned here.

The shadowgraph, or point-light source projection method, was popular in the 1950s, in particular for helicopter simulators.<sup>(13)</sup> However, the short-comings of the shadowgraph-based visual system seems to have limited the success of this concept. The first visual system achieving widespread use on civil aviation training as well as on research and development



FIG. 10. Comet IV with pitch motion. Reprinted with permission from Cambridge University Press, U.K.

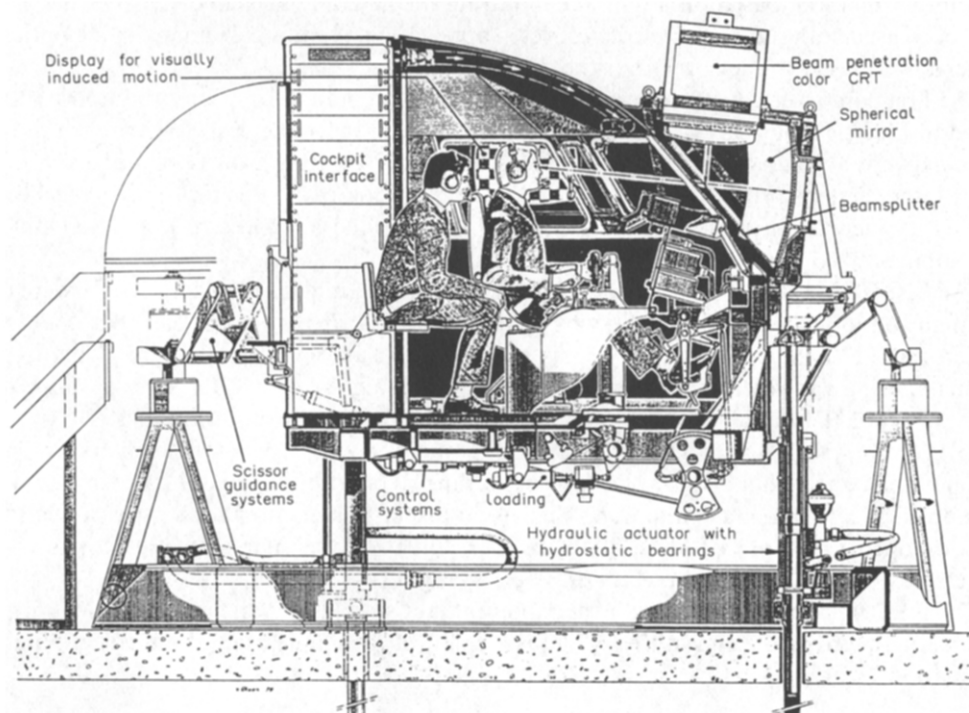


FIG. 11. DUT moving-base visual flight simulator.

simulators was based on the Closed Circuit Television (CCTV) method. In this case the view of a scale model of an airport was presented to the pilot by a moving television camera. In the mid 1950s serious development of CCTV visual systems began with monochrome systems, being produced by Curtiss-Wright, Link and General Precision Systems<sup>(12)</sup> (Fig. 12). The first colour CCTV visual system was produced by Rediffusion in 1962.

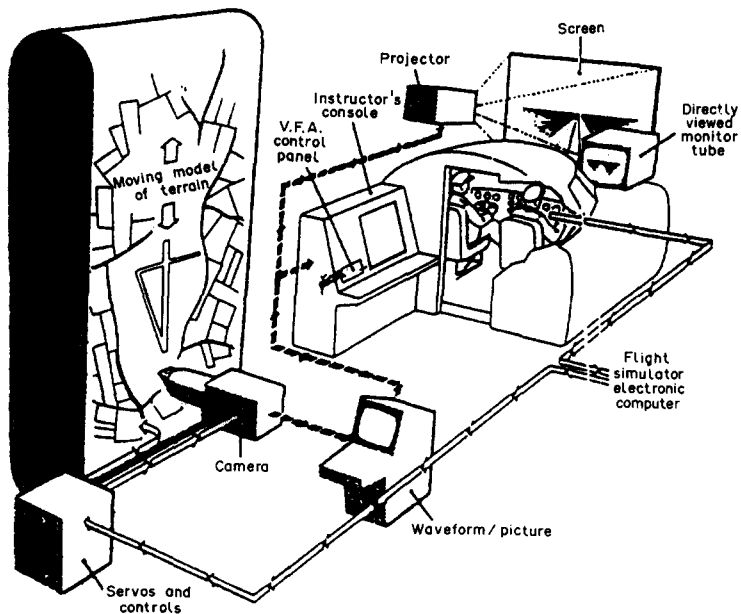


FIG. 12. The G.P.S. CCTV visual system.

Another method, based on a film, taken during the actual approach of an airplane, has also been used with success for more restricted applications. In this case anamorphic optical systems were used to 'deviate' from the nominal approach path.

The first computer generated image (CGI) systems for simulation were produced by the General Electric Company in the U.S.A. for the space programme. Early versions of these systems were able to generate a two-dimensional (2D) 'pattern ground plane' image,<sup>(10)</sup> while later versions produced 3D images in real-time. Progress in this technology has been fast as its increase in performance is closely linked to the advances in microelectronics development.<sup>(18)</sup>

The first CGI systems, economically feasible for airline crew training simulators, were of the night-only type using the stroke-writing or calligraphic display method, rather than the raster scan (TV) method of display. This resulted in a superior reproduction of the light points of e.g. a runway and its surroundings. The first night-only CGI system of this type was the 'Vital II', manufactured by the McDonnell-Douglas Corporation in 1971.

In 1967 the DUT flight simulator, developed since 1962, was provided with a so-called contact analogue visual display of a runway outline,<sup>(5)</sup> providing the possibility for studies on approach and landing simulation. This visual display, using a high-intensity projection oscilloscope, was replaced in 1980 by a CGI night-only visual system, using beam-penetration color CRTs and collimating optics (Fig. 11).

The following chapters deal with the modern flight simulator, which in its present form probably arrived at the end of the 1970s, as a result of the application of the current flight simulation techniques.

### 3. FLIGHT SIMULATOR APPLICATIONS

#### 3.1. GENERAL

The most important and frequent application of the flight simulator is its use for the training of aircrew. Over 100 airlines all over the world operate more than 400 flight simulators for the skill development, licensing and proficiency maintenance of their cockpit crews. An overview of the extent to which airline simulators are used for training can be

obtained from e.g. the Aviation Journal *Flight International* in their "Simulator Census", appearing about once per year.

A similar acceptance of flight simulation for training has taken place in military aviation. The airforces of most countries in the world use a range of simulators for pilot training and also for airplane maintenance tasks. Military use of flight simulators starts as a part of *ab initio* pilot training and continues with advanced training, including type conversion and training for specific tasks. Examples are: air-to-air refuelling, airborne surveillance and air-to-air combat.

Astronautics is another area where flight (space) simulation has an invaluable training function. No other means than simulation exists for astronaut training for the manned space programme. The Mercury, Gemini, Apollo, Skylab and Space Shuttle missions depended entirely on simulators for engineering, development of flight procedures and for the space flight training of astronauts and flight control personnel. How close these simulations were to the actual missions is illustrated by the recovery of the Apollo 13 in 1970. When the Apollo 13 spacecraft was 200,000 miles out in space, a liquid oxygen tank exploded in the service module. By hooking up a coast-to-coast network of simulators, computers and experts, providing the possibility to simulate every action to be taken in advance, a successful return to Earth was achieved for the three astronauts, Lovell, Haise and Swigart, by making use of the ascent-stage of the 'Lunar Module'.

Research and development simulators are used in the design and development of modern aircraft, research on the man-machine interface and for licensing, certification and accident investigations.

A distinction should be made here, between ground-based facilities and in-flight simulators. An indication of the range of simulators for research and development is presented in,<sup>(36)</sup> the largest ground-based facilities in the Western hemisphere being available at NASA-Ames (U.S.A.) and RAE Bedford (U.K.), see Section 3.3.

The scope of research work done on flight simulators is reflected by the variety in size and cost of the research and development facilities, ranging from about \$10,000 to more than \$100 million.

### 3.2. TRAINING SIMULATORS

The most common use of simulators—as mentioned before—is undoubtedly training. Airlines as well as the airforces use part-task trainers, cockpit procedure trainers and full flight simulators, of which the latter, being the most complicated, are treated here. The aim of the use of a flight simulator for training is to reproduce the aircraft behavior in all flight phases synthetically, so the cockpit crew-members by flying the simulator can (1) acquire and maintain the skills necessary to safely and efficiently operate the real aircraft; (2) prove their proficiency to a check-pilot or examiner (prof-check, to be performed every six months).

Simulators are used for initial (military only), continuation, and recurrent training of cockpit crew, maintenance personnel, and command and supervisory staff. Simulators trying to duplicate all or part of actual equipment or systems are used extensively for purposes like familiarization, acquiring procedural and continuous control skills, learning part- or whole-task performance, and the practice of complete or segments of missions. A simulator that duplicates the behavior of an aircraft can be used for training purposes in much the same way as the real aircraft. However, most training simulators incorporate instructional features to simplify and control the training process.

The way a simulator is used for training and the availability of instructional support facilities, are as important as the handling characteristics of the simulator. A training simulator does not train by itself, but is only a tool to carry out and support a training program. Instructional support features usually include, as a minimum:

- means for instructional control of the simulation process, providing performance feedback to the trainee, and supplying performance information to the instructor;
- a situational context or scenario for the training session.

Modern instructor stations carry out most of the manual, time-consuming tasks required to operate the simulator automatically. This enables the instructor to concentrate on his main task, managing the training exercises. Such automated instructional features may include:<sup>(24)</sup>

- *Automatic Demonstrations*, meant to achieve standardized performance of maneuvers and procedures.
- *Programmed Missions*, meant to establish standard problems with standard performance measurement approaches.
- *Automated Malfunction Insertion*, where malfunction insertion is tied to programmed missions.
- *Performance Record/Playback*, where the trainee afterwards can observe control movements, cockpit indications, visual and motion cues, enabling the learning principle known as self-confrontation.
- *Performance Measurement*, meant to define the performed flight in detail, and to monitor how student performance fares with respect to predefined standards.

With the instructional capability provided by advanced instructor stations, the role of the simulator in a flight training program will continue to change from that of a mere substitute airplane to that of a more encompassing training tool.

The advantages of ground-based 'flight' training over airborne flight training include reduced costs (the 747 costs in the order of \$12,500/flight-hr, while the 747-simulator costs only some \$750/hr), fuel savings, no pollution and noise, less risk and, as may be clear from the above, *more efficient* training. For the use of flight simulators for civil cockpit-crew training, the US Federal Aviation Administration (FAA) issued its Advanced Simulation Plan.<sup>(21)</sup> The allowances and requirements for Phase I, II, and III simulator approval levels may be cited here:

— *Phase I:*

*Allowances:* Training and proficiency checks of qualified airline pilots, including take-off and landing, and ground handling.

*Requirements:* Night/dusk visual system, field of view (FOV) 48 degrees horizontally and 30 degrees vertically (FOV 48/30); 3DOF motion system with a maximum latency of 300 msec.

— *Phase II:*

*Allowances:* Upgrade from first officer to captain and transition from aircraft type.

*Requirements:* Dusk visual system, able to generate texture (FOV 75/30); 6 DOF motion system, maximum latency of 150 msec.

— *Phase III:*

*Allowances:* Total simulation, which means that the new captain may make his first real flight with passengers under the supervision of a check-captain.

*Requirements:* Day/dusk/night visual system (FOV 75/30); 6 DOF motion system, latency as for Phase II.

Most of the civil training simulators, acquired these days, are Phase II approved. This means that a pilot could qualify from one type of aircraft to another, or upgrade from first officer to captain with *total training* on the flight simulator.

### 3.3. RESEARCH AND DEVELOPMENT SIMULATORS

#### 3.3.1. *Ground-Based Facilities*

Research and development simulation has emerged as an essential tool in aircraft and equipment design, development, test, and evaluation. Real-time engineering simulation provides the possibility of introducing the human element interactively at various phases into the design process. As a first benefit, realistic system performance requirements can be

established in various operational situations before the manufacturer commits to further system development.

The development of advanced aircraft and their flight critical subsystems follows a classical, hierarchical design validation process.<sup>(22)</sup> This process consists of analysis, off-line and 'pilot-in-the-loop' simulation, followed by flight testing (Fig. 13). Each phase of development achieves increasing fidelity and confidence in the design, however at significantly increasing costs. The elimination of major design deficiencies early in the development process may result in tremendous cost savings. As a consequence piloted engineering simulation is a powerful, cost-effective tool for the verification of a design before hardware manufacturing. It is equally useful for the validation of hardware/software integration, prior to first flight of a newly designed or upgraded aircraft.

Next to performance, stability and control, and subsystems considerations, real-time engineering simulation provides an early opportunity to bring experienced flight crews into the development program to assess and insure in particular proper man/machine interfaces and workload levels. In this manner these flight crews are able to contribute to control system design and flight deck layout and to the integration/operation of complex subsystems, like an integrated flight management system (FMS).

In earlier aircraft developments, many of the subsystems were dedicated electro-mechanical devices. In today's aircraft, with the emergence of integrated avionic information systems, these independent devices have been replaced by networks of embedded computers and multiplexed buses. Therefore, the total integrated design, dynamic operation and safety are completely dependent on the embedded software design. This integrated system software must be verified in dynamic, real-time, multi-mode conditions. Pilot-in-the-loop engineering simulation is the only way to provide the crucial validation of the total embedded hardware/software package in a modern aircraft, before first flight.

In terms of equipment, research and development simulators run the full spectrum from fixed-based cockpits, without even a visual system, to full 6 DOF motion-base visual flight simulators. The visual systems range from simple one window infinity displays, affording take-off and landing imagery, to domes completely enclosing the crew station providing imagery for air-to-air combat, see Section 4.4.

Examples of the successful use of ground-based flight simulators for research and development are:<sup>(37)</sup>

- The investigation of the inertia coupling problem of fighter aircraft, at North American Aviation in 1954, following the loss of a F-100 'Super Sabre'. The inertia coupling caused the aircraft, during fast rolling maneuvers, to end up perpendicular to the airstream. Using flight records of the control inputs, a very good match between simulation and flight was achieved.
- In the late 1950s and early 1960s a major achievement in R & D simulation was the X-15 program at North American. The first powered flight of the X-15 occurred on September 17 1959, when this rocket powered aircraft was launched from a B-52. Heights greater

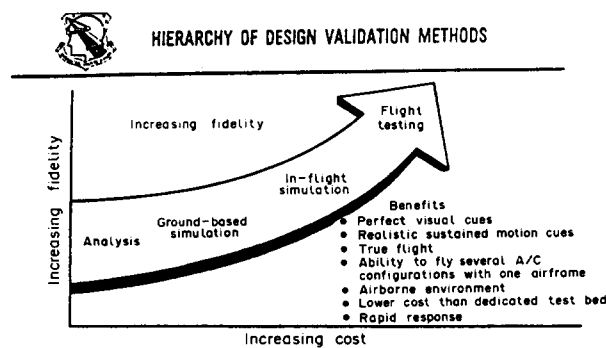


FIG. 13. Hierarchy of design validation methods.

than 200,000 ft, and speeds above MACH 6 had been achieved by the end of 1961. An essential part of this program was the preparation on the flight simulator. Pilots, like Scott Crossfield and Chuck Yeager, spent 8–10 hr in the X-15 simulator before making a 10–12 min research flight.

- In February 1964, a prototype BAC 1-11 was lost in stall-testing. The piloting aspects of the so-called 'Deep Stall' were explored on the Research Simulator at Warton, U.K. and the inherent stability problem, posed by the T-tail configuration was recognized. The implications of the accident were understood within weeks and recommendations for a change to a fully powered elevator, and the installation of a 'stick pusher' were proposed. Both airworthiness authorities and the aircraft customers were convinced, by use of the simulator, that the problem was solved. Similar circumstances arising on other designs were prevented, using simulators by manufacturers and research establishments in Europe and the USA.
- Control difficulties on the large jet transports, cruising at high altitude, were experienced in the mid 1960s. These incidents resulted in the loss of several thousands feet of height and were caused by so-called 'Clear Air Turbulence' (CAT). During CAT, pilots easily exceeded the critical MACH number, and retrimming in attempting a recovery resulted in a serious danger of overstressing the aircraft. NASA and RAE research simulators were used to investigate these incidents, and to demonstrate to pilots the best operational procedures to minimize the impact of CAT.
- A forerunner of the use of a training simulator for accident investigations was the contribution of the Trident simulator, following the loss of a BEA Trident aircraft in 1972. The entire sequence of events of the aircraft, which entered a deep stall following premature retraction of the leading-edge flaps, was reconstructed on the simulator.
- In the design, development and certification of the 'Concorde',<sup>(32)</sup> the first and, until now, only Supersonic Transport (SST), extensive use was made of flight simulation (ground-based as well as in-flight simulation). The range of problems, studied on simulators at Aerospatiale (Toulouse), B.A.C. (Bristol) and R.A.E. (Bedford), was large: system development, stability and control, failures, operating techniques, and crew workload. The predictions, resulting from the use of the research simulators, were largely confirmed in flight and illustrated the important role that simulators play in industry.

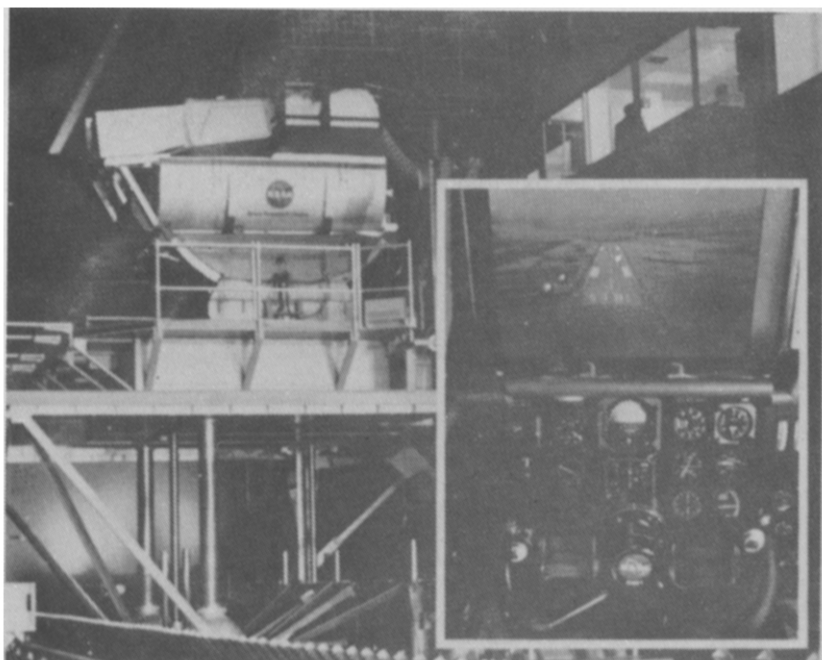


FIG. 14. FSAA facility. Reprinted with permission. © The American Institute of Aeronautics and Astronautics.

Later a joint FAA/NASA program was conducted on Concorde,<sup>(38)</sup> using the 'Flight Simulator for Advanced Aircraft' (FSAA) at NASA Ames (Fig. 14). The simulation results gave the FAA great confidence in the use of simulation as a research and certification tool.

- In another joint effort, Boeing and NASA used the FSAA for a very complete simulation of the Boeing 747 transport<sup>(25)</sup> in a simulation program on civil transport airworthiness criteria. The modelling data, the application of these data in the model, and the results of real-time simulations performed in the FSAA are described in Ref. 26. This very detailed report also contains a comparison of FSAA responses with flight test data and the results obtained in a B-747 training simulator.
- The various phases in the design and development of a new powered-lift STOL research airplane<sup>(39)</sup> were also explored on the FSAA, presenting an example of the use of this R & D simulator for aircraft design studies. This new design concept emphasized the fidelity of the simulator, principally because of the limited amount of closely related experience on which the pilots could draw, for confirmation of the characteristics observed in the flight simulator.

The important outcome of the above programs is the reliability of the results obtained. The general reactions of the pilots, who have conducted the evaluations on the FSAA, were that it permitted them to assess the handling qualities of the simulated aircraft with a degree of confidence, approaching that of actual flight. In some of these programs, this opinion has been supported by concurrent or subsequent flight tests.

Two other large research and development simulator facilities are located at NASA Ames Research Center in the U.S. as well. These facilities consist of the Vertical Motion Simulator (VMS) and the Man-Vehicle Research Facility, the latter being operational since 1985. The 6 DOF VMS, with an excursion capability of 20 m in vertical direction (heave), and 15 m horizontally (sway or surge), can be assembled and integrated with four interchangeable cockpit cabs. The interchangeable cab concept is the key to efficient use of the VMS. To reduce the simulator down-time for cab teardown and the preparation of a new experiment, the interchangeable cabs are reconfigured and checked out in a separate laboratory, while the VMS remains operational with a fully checked cab on the motion platform. The four interchangeable cabs include:

- two single-seat helicopter cabs, used in the 'Rotorcraft System Integration Simulator' (RSIS) (Fig. 15);
- a side-by-side transport cockpit, used a.o. for Space Shuttle simulation;
- a fighter cab, used for the simulation of the Grumman X-29 forward-swept-wing fighter aircraft.

The RSIS is used for research into rotorcraft handling qualities, and to support all phases of the development of a family of light helicopters (LHX).

The Man-Vehicle Research Facility provides an opportunity for scientists to study human factor problems in the complex relationships between cockpit crew members, current advanced transports and Air Traffic Control (ATC). This facility includes:

- a Boeing 727 moving-base simulator, representing current-technology transport aircraft;
- an 'Advanced Flight Deck' simulator, representing 1990s-technology transports (Fig. 16);
- a simulated air traffic control environment, which includes three controller consoles and 40 'pseudo-pilot' terminals that appear to the simulator pilots as other aircraft, using the airspace.

At RAE Bedford in the U.K., a research and development simulator with a new 5 DOF motion system, with an excursion capability of 10 m heave and 8 m surge or sway, is used for the investigation of new forms of flight control and of the influence of atmospheric turbulence on aircraft, flight crew and passengers.<sup>(40)</sup>

At the National Aerospace Laboratory (NLR) in the Netherlands, a multi-purpose research flight simulator facility is used to investigate problems related to pilot-aircraft

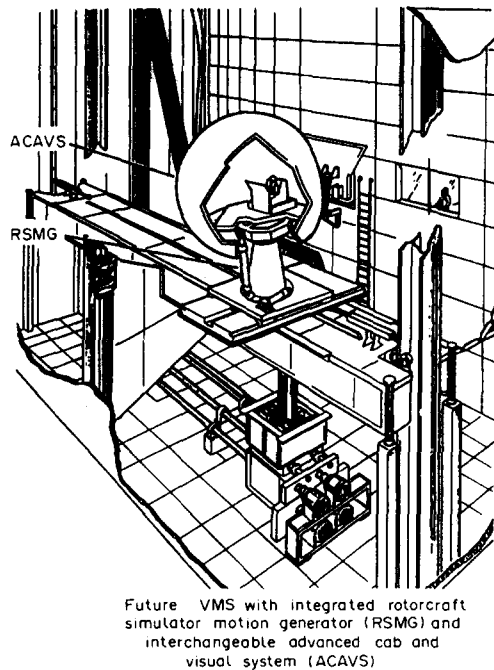


FIG. 15. Rotorcraft System Integration Simulator (RSIS).

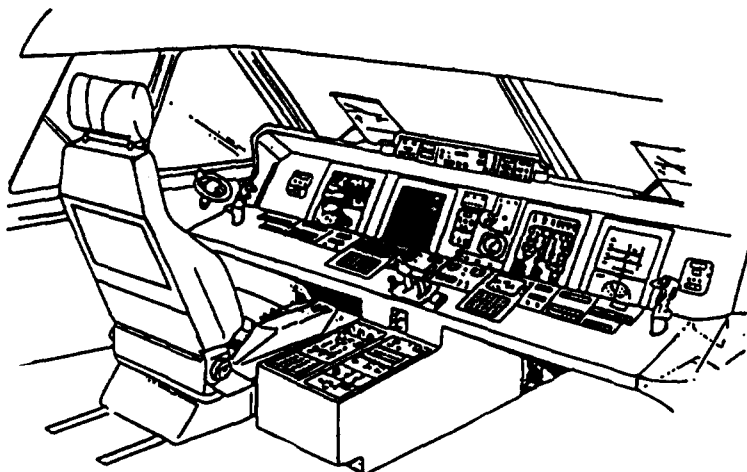


FIG. 16. Advanced concept flight station.

interactions.<sup>(29)</sup> A new, second generation 6 DOF hydrostatic motion system was developed for this facility, which possesses unique dynamic characteristics for demanding tasks like the simulation of high-performance helicopters and fighters, see Section 4.5.

In a University environment, the Faculty of Aerospace Engineering of DUT uses the moving-base visual flight simulator for:<sup>(20)</sup>

- aircraft stability and control research;
- research on flight simulation techniques.

Similar work is performed at the Institute for Aerospace Studies at the University of Toronto, Canada.<sup>(35)</sup>

### 3.3.2. In-Flight Simulators

An in-flight simulator is a specially equipped aircraft of which the stability, control and feel, i.e. the handling characteristics, can be varied, to match the characteristics of the aircraft to be investigated. In the 'simulation-mode', this so called 'variable stability aircraft' operates under 'fly-by-wire' control, where the functional connection between pilot control inputs and flight control actuator outputs is given by user defined functions. This results in in-flight simulator control laws, which allow the evaluation pilot to fly an aircraft model programmed in the on-board computer system. As the pilot moves the controls, the aircraft responds as the simulated aircraft would. The model following control laws in the variable stability system generate commands for all the flight control actuators, to force the in-flight simulator to follow the on-board computed equations of motion. As a consequence the pilot experiences the flight-motions and handling qualities of the aircraft simulated.

The advantages of in-flight simulation over ground-based simulation are the readily available visual and motion cues. The visual is the real world and the motion is complete and sustained. Besides the provision of real visual and motion cues, the in-flight simulator forces the pilot into the mental realization that he is flying a real aircraft. This elevates the 'pilot gain' to a realistic level, resulting in more precise control. In-flight simulation also provides all the concerns of actual flight, in particular the knowledge that a human error may result in possible aircraft damage and personal injury.

Just as in ground-based simulation, certain aspects may degrade in-flight simulation. A near perfect simulation is achievable only when the in-flight simulator has the same flight envelope, complete control of all six-degrees-of-freedom (6 DOF), and adequate control power to match the linear and angular accelerations of the simulated aircraft. For the in-flight simulation of large flexible aircraft (Fig. 17), this is a heavy demand on the 6 DOF independent controls of the in-flight simulator.

An in-flight simulator, especially designed for this purpose, is the Calspan 'Total In-flight Simulator' (TIFS) (Fig. 18). This is a highly modified Convair 131H having a.o. large vertical control surfaces on both wings to generate lateral acceleration, and an evaluation cockpit in the nose-section of the aircraft.

Other well-known in-flight simulators in the US are:<sup>(33)</sup>

- the NT-33A of the Flight Dynamics Laboratory, used a.o. for the simulation of the F-16 and F-18 fighter aircraft;<sup>(31)</sup>
- the NASA Gulfstream II Shuttle Training aircraft;<sup>(30)</sup>

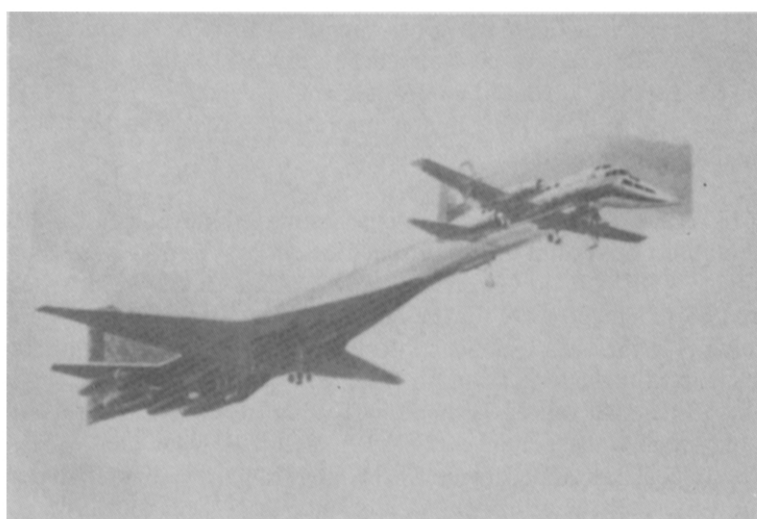


FIG. 17. In-flight simulation of large flexible aircraft. Reprinted with permission. © 1985 Society of Automotive Engineers, Inc.



FIG. 18. Total In-Flight Simulator (TIFS).

- the US Navy's X-22, a 4-engined research aircraft with 4 ducted propellers, used for V-STOL research;
- the USAF/USN/Calspan Learjet.

A unique application of in-flight simulation is the training of test pilots at the Air Force and Navy Test Pilot Schools, using the NT-33A and Learjet variable stability aircraft. Different sets of aircraft dynamic characteristics are programmed in the variable stability systems and subsequently flown by the student test pilots. In this way handling qualities evaluations are performed and new technologies, such as side-stick-controllers and head-up-displays with various characteristics, are introduced to the student pilots, greatly enhancing the level of academic instruction. Even dangerous (unstable) configurations can be demonstrated safely, because the safety pilot can take over control instantly.

In Europe, the following in-flight simulators are in use:<sup>(23)</sup>

- the Jaguar T2 digital fly-by-wire research fighter aircraft of British Aerospace, used for the investigation of flying qualities, active control technology, system architecture, etc.;
- the BAC 1-11 twin jet medium transport aircraft of the Royal Aircraft Establishment (RAE, Bedford, U.K.), used for civil avionics research like flight management systems (FMS), cockpit displays, advanced control techniques, etc.;
- the Harrier T2 two seat VSTOL fighter aircraft of RAE, used for VSTOL/STOVL research and the investigation of advanced controls and displays for this type of aircraft;<sup>(34)</sup>
- the FWF 614 ATTAS (Advanced Technology Testing Aircraft System), a short-haul twin jet variable stability aircraft of the "Deutsche Forschungs- und Versuchsanstalt für Luft- und Raumfahrt" (DFVLR) in Germany. The ATTAS is used as a flight test vehicle for research and development aimed at the demonstration and validation of new methods and technologies in the areas of flight control, flight guidance, navigation, man-machine interactions, and in-flight simulation,<sup>(27)</sup> (Fig. 19);
- the BO 105 ATTHES (Advanced Technology Testing Helicopter System), a digital fly-by-wire variable stability helicopter of DFVLR, used for helicopter handling qualities research, future cockpits, and advanced helicopter flight control system design;<sup>(28)</sup>
- the Falcon Mystere 20 twin-turbosfan variable stability executive transport of France.

Experience obtained in the application of both ground-based and in-flight simulation has shown that both simulation techniques have developed their own areas of excellence. They

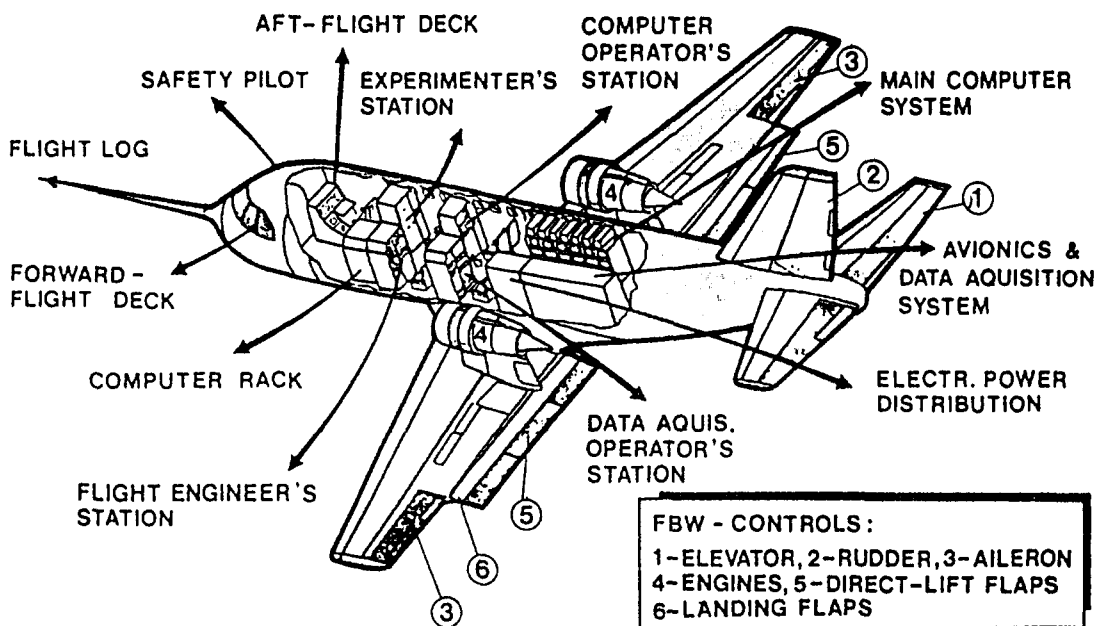


FIG. 19. Advanced Technology Testing Aircraft System (ATTAS).

generally complement each other when used in a combined test program. Many factors influence the choice between ground-based and in-flight simulators and the level of sophistication to be used. Serious consideration should be given to which items are critical by evaluating the desired final results of the simulation. The use of both types of simulators—if at all available—may often be justified in a combined ground-based and in-flight simulation program.

#### 4. MAIN COMPONENTS OF A PILOTED FLIGHT SIMULATOR

##### 4.1. GENERAL

The main components of a piloted flight simulator are (Fig. 20):

- The real-time digital computer, driving the simulator.
- The simulator cockpit, containing the flight controls, displays and the sound simulation system, providing various levels of equipment fidelity to the pilot, see Section 4.3.
- Visual systems, generating the visual scenery of the outside world.
- Motion systems, generating aircraft-like specific forces and angular accelerations, see Section 4.5.

The basis of any flight simulator is the mathematical model,<sup>(56)</sup> including the data package,<sup>(44)</sup> describing the characteristic features of the aircraft to be simulated. No matter how sophisticated the components of a flight simulator may be, an incorrect mathematical model and/or data package will cause the simulator to be unable to fulfill its intended mission satisfactorily, see Section 5.

The next sections discuss the main flight simulator components, starting with perhaps the most important part, i.e. the 'real-time' digital computer driving the flight simulator.

##### 4.2. REAL-TIME DIGITAL COMPUTER

Progress in computer technology, especially in processing speed and memory capacity, permits simulation of multiple, complex functions in real-time.

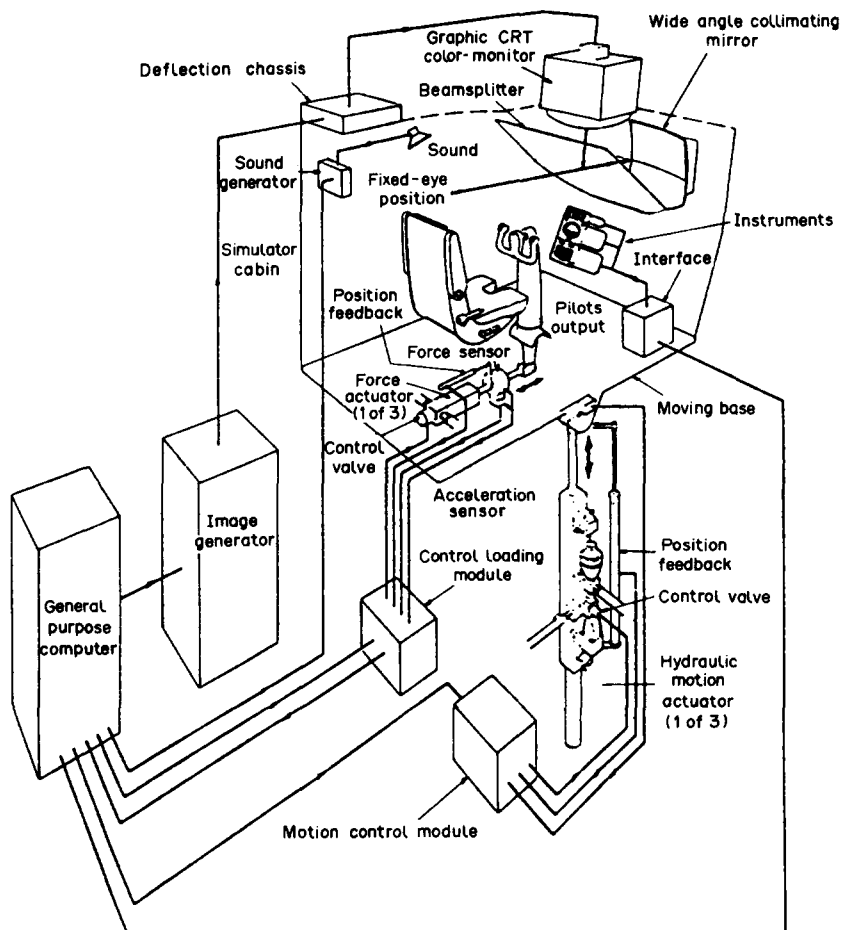


FIG. 20. Simplified lay-out of flight simulation components.

Piloted flight simulation, using computer speed and memory capacity to the limits, is realized by mathematical modelling of the aircraft's aerodynamic, aeroelastic, flight control, propulsion, landing gear, avionics and environmental characteristics, i.e. the response to atmospheric turbulence and wind shear (Fig. 21). In this figure, the 'lifeware' module 'HUMAN PILOT', is the only one which cannot be completely described in mathematical terms.

Mathematical models, used to simulate modern aircraft, consist of an extensive set of non-linear differential equations with large amounts of aerodynamic function data (tables), sometimes depending on 4 to 5 variables. In addition, these equations contain arbitrary discrete and continuous forcing functions, and a multiplicity of constraints imposed on the states of the different aircraft systems. From the resulting forces and moments, generated by these systems (Fig. 21), the equations of motion are composed and solved by the digital computer using an adequate integration algorithm. This process allows the simulation of the complete range of static and dynamic aircraft operating conditions, including landing and takeoff, ground-handling and emergency situations such as engine failure, stalls and component malfunction. For training simulators other significant parts of the computations involve fuel systems equations, weight, balance and inertia changes, autopilot/flight director functions, flight management system, navigation functions, radio aids and the instructor station, see Section 3.2.

Frequently the above avionics equipment consists of 'flight hardware'. Aeronautical Radio Inc. (ARINC) has prepared a working paper<sup>(42)</sup> for the Airlines Electronic Engineering Committee (AEEC) to enable direct use of applicable airborne equipment in

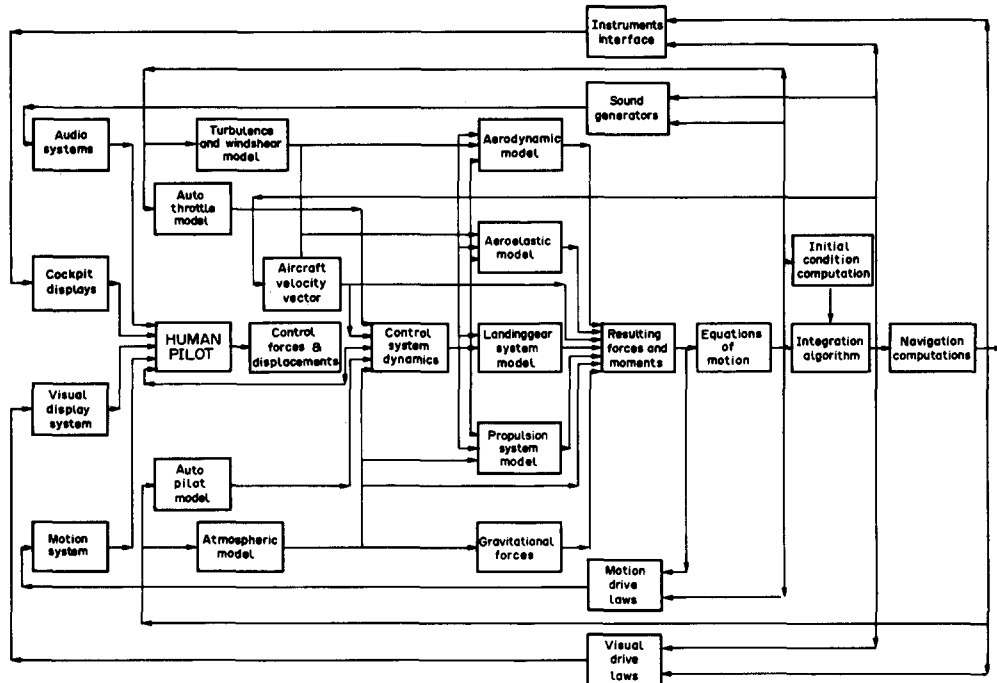


FIG. 21. Block diagram of software and hardware modules for piloted flight simulation.

flight simulators. This provides for readily available spares, the most recent version of operational software, and the assurance that equipment response will be the same in the aircraft and in the simulator. In particular the integration of 'the seventeen IATA Simulator Functions', e.g. freeze, reset, slew, recall, etc.<sup>(42)</sup> in new avionics designs, is proposed.

Because there is a 'pilot-in-the-loop', and/or hardware and avionics in the loop, the complete set of equations must be solved in real-time. This means that the simulated events must occur within the same time scale as they would occur in the real aircraft. Therefore in real-time flight simulation, the computer must carry out all calculations in the mathematical model, including input/output, a sufficient number of times per second to achieve dynamic fidelity of the highest natural frequency present in the simulation response.<sup>(43)</sup> Figure 22 shows the required computational duty cycle (sample period) as a function of airplane natural frequency.

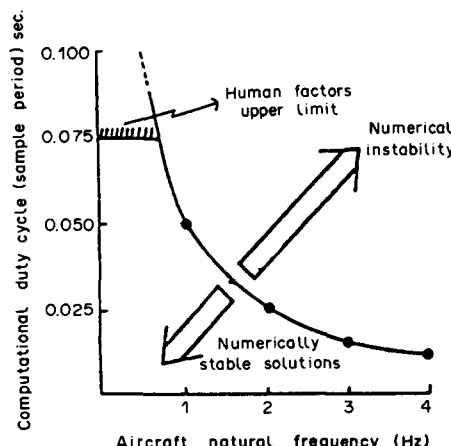


FIG. 22. Required sample period for real-time simulation of fixed wing non-aeroelastic aircraft.

The real-time constraint for a serial host computer, with analogue and digital input/output, can be expressed as:

$$[\text{Code Processing Time} + \text{Input/Output Time}] < [\text{Sample Period}] \quad (4.1)$$

This can place severe demands on required computer power.

The computations needed for flight simulation can be broken down into the following basic computational operations:

- addition and subtraction,
- multiplication and division,
- function generation (up to 5 independent variables),
- numerical integration (1 to 4 passes per sample of input data, e.g. 4 for a 4 pt Runge-Kutta routine),
- coordinate transformation,
- analogue and discrete input/output,
- bulk data access (navigation data base),
- decisions and branching (Boolean).

For a particular simulation application, the real-time constraint (4.1), the total number of computational operations, the applied integration algorithm, the number of samples per cycle of the highest frequency of interest and the airplane natural frequency, determine the required computer power. A measure of the required computer power, e.g. the simulation of the Boeing 747, can be expressed as:<sup>(43)</sup>

$$\text{FLOPS} = N_o \cdot P_s \cdot S_c \cdot F, \quad (4.2)$$

where FLOPS = the required number of Floating Point Operations per Second,  $N_o$  = normalized static operations to update dynamics per program pass (i.e. the first three items in the list of basic computational operations ( $= 4 \cdot 10^4$  for B-747)),  $P_s$  = number of program passes per sample of input data ( $= 4$  for 4 pt Runge-Kutta),  $S_c$  = number of samples per cycle of the highest natural frequency ( $= 20$  for the B-747),  $F$  = highest relevant airplane natural frequency in Hz (e.g. 1.5 for the B-747).

For the B-747 simulation this results roughly in a required computer power of 4.8 Million Floating Point Operations per Second (MFLOPS). Some estimated computer power requirements for other types of aircraft are:

- Fighter, including weapons simulation: 3–6 MFLOPS;
- Rotorcraft, including the simulation of a five blade main rotor at 200 RPM: 14–15 MFLOPS.

An alternative way to meet the high required computer power of today's modern flight simulators is the use of a functionally distributed computing system.<sup>(58)</sup> It consists of microprocessors, partitioned on a functional basis with the autonomous major functions connected as a network (Fig. 24). In this figure the microprocessors, providing for the major functions in the functionally distributed computer system, replace the single host computer in a traditional simulator configuration, as schematically depicted in Fig. 23.

As an example, a functionally distributed computer system for an Airbus A300-600 simulator<sup>(58)</sup> may contain seven major functions divided over a total of 27 CPUs for its real-time application software.

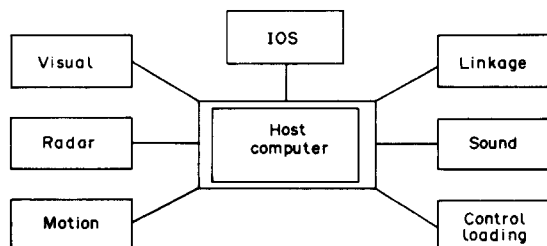


FIG. 23. Traditional simulator configuration.

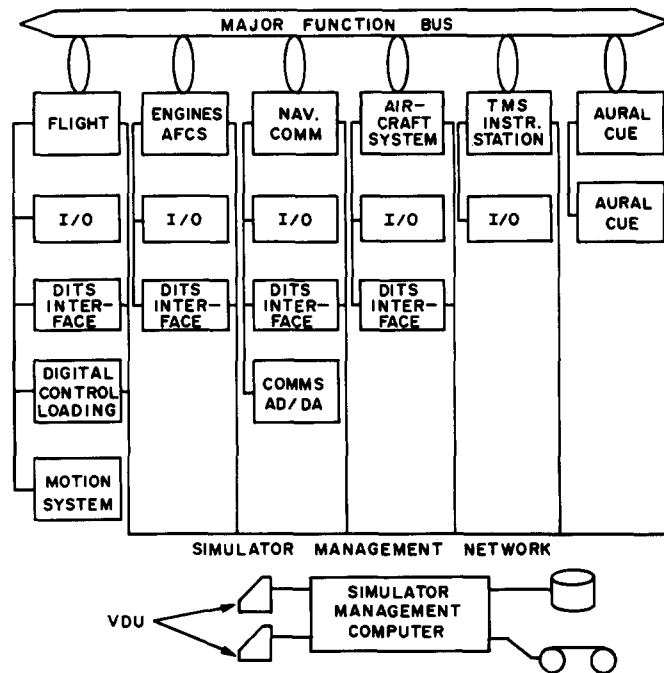


FIG. 24. Functionally distributed simulation.

By way of an example, at the Faculty of Aerospace Engineering of DUT, a Gould SEL 32/87 single host computer drives the moving-base visual flight simulator. The real-time simulation software running on this 'super-mini' computer, has a modular program structure in five levels,<sup>(52)</sup> as shown in Fig. 25. The acronyms used to identify the software modules in the modular program structure of Fig. 25 have the following meaning (top to bottom, left to right):

#### *First level*

- START: Main program unit of task 'MAIN.LM' ('LM' = Load Module), used for array-declaration and transfer of data to subroutine MAIN.
- MAIN: Control program for non-linear, real-time flight simulation.
- INCO: Main procedure of task 'INCO.LM', used to establish a memory area for communication between tasks 'MAIN.LM' and 'INCO.LM' and between 'INCO.LM' and 'AERO.LM'. In the initialization phase, the initial condition is computed (FINCO) and during simulation the integration procedure is executed (FAIRC).
- MODL: Motion Drive Laws to control the flight simulator motion system.
- VIDL: Visual Drive Laws generating inputs to a C.G.I. visual system.
- INSTR: Instruments software interface to drive the flight instruments inside the simulator.

#### *Second level*

- FSIDS: FSIDS provides a survey of the input data for subroutine MAIN and specifies the descriptors of the aircraft variables.
- FINER: Subroutine computing the inertia parameters in the equations of motion in a form where all time derivatives appear in the lefthand side of the equations, see Section 5.
- FSTAT: Subroutine computing the air density at a given flight altitude, using the model of the 'US Standard Atmosphere'.
- FINCO: Subroutine computing a steady initial condition using the non-linear equations of motion of the aircraft. FINCO is used prior to actual simulation.
- INPUT Z-CARD: The 'Z-CARD' is the I/O-interface between the Gould SEL 32/87 and the flight simulator systems. The routine INPUT Z-CARD converts 32-bit reals into the correct output format.

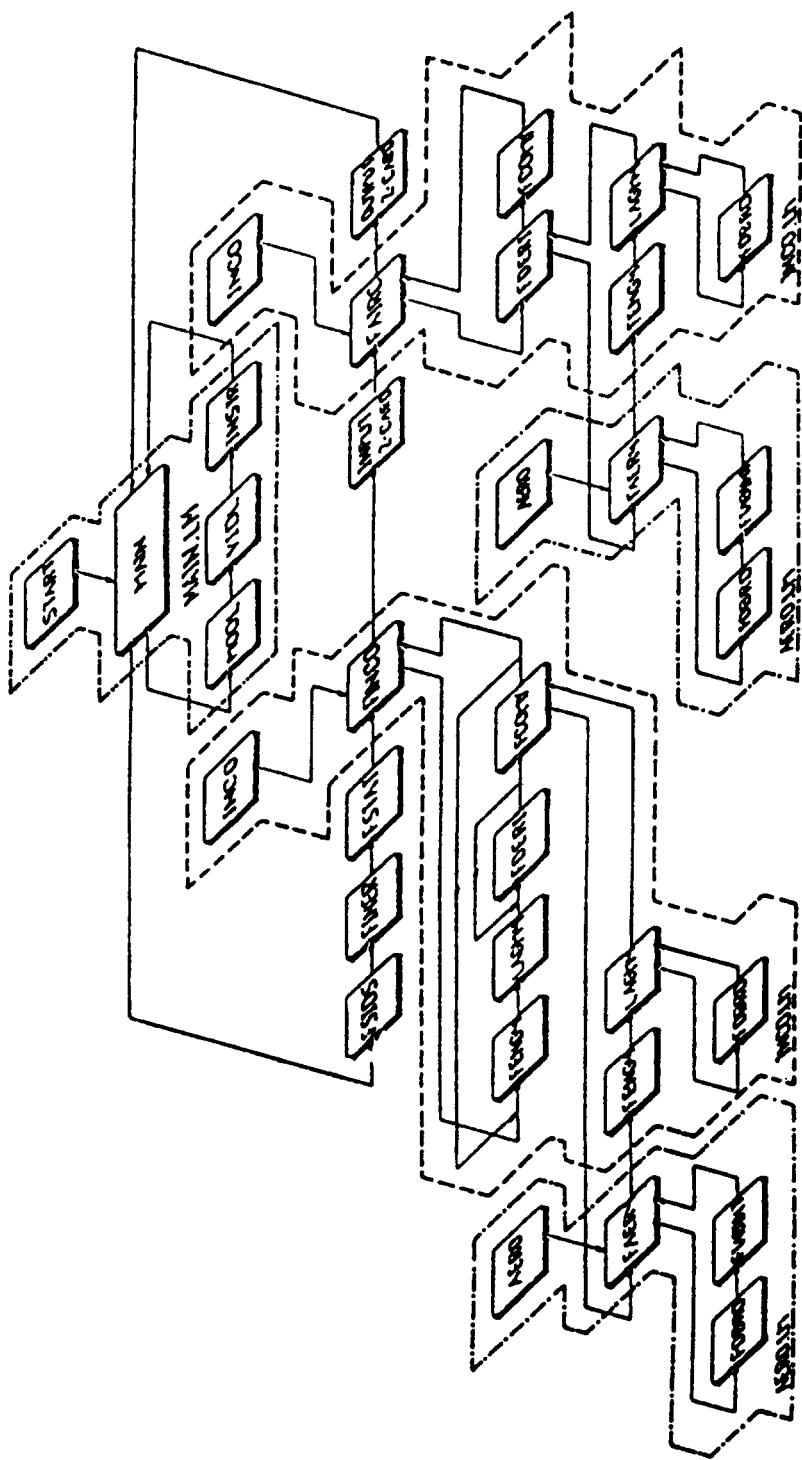


FIG. 25. Modular program structure of DUT real-time simulation software.

- FAIRC: Subroutine computing the aircraft state vector using one of three numerical integration methods: (1) Adams-Bashforth (AB2), (2) Heun (2-step), (3) Runge-Kutta (4-step), see Section 5.2.
- OUTPUT Z-CARD: This routine converts the input-signals from the flight control systems in the simulator cockpit (after analogue to digital conversion) into 32-bit reals for the Gould 32/87.

*Third, Fourth and Fifth Level*

- AERO: Main procedure of task ‘AERO.LM’ used to establish a memory area for communication between tasks ‘INCO.LM’ and ‘AERO.LM’.
- FENG4: This subroutine computes the dimensionless forces and moments resulting from the operation of the aircraft engine(s); the number indicates the aircraft-type, see Section 5.2.2.
- LAGM4: This subroutine calculates the forces and moments of the landing gear on the aircraft during taxi, take-off and touchdown, see Section 5.4.
- FDERI: In this subroutine the augmented state time derivatives of the airplane are computed, using the aerodynamic model (FAIR4), the engine model (FENG4) and the landing gear model (LAGM4), see Section 5.2.2.
- FCOMY: This subroutine computes the airspeed  $V$ , the angle of attack  $\alpha$ , the side-slip angle  $\beta$ , the flightpath angle  $\gamma$ , the rate of climb (descent)  $C$  and the altitude  $h$  from the state vector  $x(t)$  and presents them in the output vector  $y(t)$ .
- FAIR4: Subroutine calculating the aerodynamic forces and moments acting on the aircraft, see Section 5.2.2.
- FDBRD: This subroutine reads a matrix or vector from a database, containing for example the lift coefficient ( $C_L$ ) as a non-linear function of angle of attack ( $\alpha$ ), flap position ( $\delta_f$ ) and Mach-number ( $M$ ).
- FTABINT: This subroutine performs a linear table interpolation in tables with dimension of either  $M^*N$  or  $1^*N$ .

Section 5 describes the mathematical models in the subroutines mentioned above in detail. One of the applications of this modular program is the real-time simulation of a business jet,<sup>(45)</sup> see Section 5.5. Because of its modular structure, with airplane dependent and independent modules, the real-time simulation software can be readily adapted to simulate any airplane for which a mathematical model and data package is available.

There is generally a strong relationship between the level of model complexity, vehicle type, intended usage of the simulator and the required computer performance capabilities. Current in-place computational power, dedicated to real-time simulation ranges from 3 MFLOPS for a conventional transport to 15 MFLOPS for a high performance compound helicopter, using rotating blade-element models,<sup>(61)</sup> including rotor-fuselage interference.

#### 4.3. THE FLIGHT SIMULATOR COCKPIT

Before starting the discussion on the flight simulator components providing direct aircraft-state feedback to the pilot, it is appropriate to divide the cues, provided by these simulator components to the pilot, into two classes:<sup>(54)</sup>

- Equipment cues* providing a duplication of the appearance and feel of the flight displays and controller force and displacement characteristics inside the simulator cockpit.
- Environment cues* providing the (attempted) duplication of the environment, mainly using visual out-of-the-window cues and platform motion cues.

*Fidelity* is expressed by the degree to which these equipment and environmental cues match those of the real airplane. A subtle distinction between the real cues, measured objectively, and the cues the pilot subjectively experiences, provides the following definitions for two types of fidelity:<sup>(54)</sup>

- Objective fidelity* is the degree to which a simulator reproduces the behavior of the real airplane, in flight and on the ground, as sensed and recorded objectively by an instrumentation system on board the aircraft and the simulator, respectively. By including both equipment and environmental cues, this definition encompasses all pertinent dynamic cue timing and synchronization aspects of simulator fidelity.
- Perceptual fidelity* is the degree to which the pilot subjectively perceives the simulator to reproduce the real aircraft behavior in the operational task situation. The consideration of the operational equipment in the context of the task situation ensures that not only cue timing and synchronization, but also cue priority effects in the way the pilot performs his task, are taken into account.

The requirements for objective fidelity in the cockpit of the flight simulator vary with its objectives. However, the general assertion can be made that the character and the workload of the pilot's task in the simulator should be representative of those seen in flight. Hence the emphasis on perceptual fidelity.

The physical correspondence between simulator and airplane in terms of cockpit layout, flight instruments, controls, etc. for training simulators should result in high equipment cue fidelity. Environmental cue fidelity is of paramount importance for Phase II and III approved simulators, see Section 3.2.

Research and development simulators should have high environmental cue fidelity, while equipment cue fidelity may be less important here. Figure 26 shows the requirements for equipment and environmental cue fidelity.<sup>(54)</sup>

With the introduction of Electronic Flight Instrument Systems (EFIS), based on the ARINC 700-series specifications, actual flight hardware is applied in civil aviation training simulators. The necessary adaption of such airborne equipment<sup>(42)</sup> for flight simulators has already been mentioned in Section 4.2.

One of the most sensitive elements in terms of fidelity requirements are the primary flight controls in the simulator. The static force levels and dynamic feel perceived by the pilot in control of an aircraft must be totally reproduced in the simulator, to provide high equipment and environmental cue fidelity. The control forces and displacements felt by the pilot are due to a combination of break-out force and dead-band, spring force, control column inertia, forces due to aerodynamic hinge moments, static friction, coulomb and viscous friction. Today's control loading systems, based on hydraulic actuators with hydrostatic bearings,<sup>(20)</sup> have demonstrated impressive capabilities to provide the precise forces calculated in the mathematical model of the control system characteristics. Primary flight control system models may be identified from dynamic flight test maneuvers<sup>(57)</sup> in a

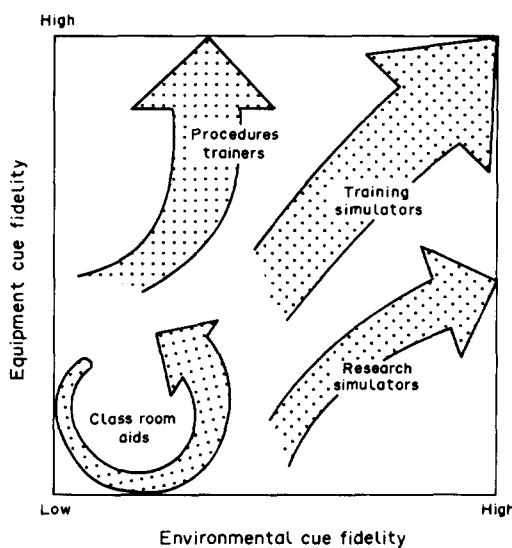


FIG. 26. Requirements for equipment and environmental cue fidelity.

similar way to the aircraft mathematical models,<sup>(45)</sup> see Section 5.5, using high-accuracy flight test instrumentation equipment.

The sound simulation system reproduces significant sounds audible in the simulated aircraft cockpit, by means of a multiple speaker arrangement. Simulated sounds like those from the turbine, compressor, taxi rumble, touchdown, crash, etc. are realistic to the degree that direction as well as amplitude and frequency content are correctly presented.

Future airplanes may be flying under control of the autopilot, autothrottles and Flight Management Systems 95% of the time. The maintenance of the pilot's manual flying skills and the training of unusual and emergency procedures, using advanced flight simulators, will require more and more attention.<sup>(41)</sup>

NASA Langley and NASA Ames Research Centers initiated, in cooperation with Lockheed Georgia, the development of Advanced Concepts Research Simulators (ACRS).<sup>(60)</sup> These flight simulators will be used to evaluate new flight deck concepts,<sup>(53)</sup> human engineering aspects and operational procedures. One of the envisaged cockpits has already been shown in Fig. 16.

The purpose of the research program carried out using the ACRS will be the evaluation of:

- future aircraft operation techniques;
- new display technology and criteria;
- flight station integration;
- flying qualities and control systems;
- crew performance and associated human factor aspects;
- flight hardware and system reliability.

More complex interfaces between the pilot and the aircraft systems, e.g. 'touch panels',<sup>(53)</sup> are introduced which may also affect training, as the controls can no longer be identified by location and shape.

#### 4.4. VISUAL SYSTEMS

In piloted flight, vision is the primary sense for the perception of real world data. Even today, with the availability of many sophisticated instruments, systems and automatics, out-of-the-window vision still plays a crucial role in the piloting task. In flight simulation visual systems are equally important. Out-of-the-window visual simulation presents a formidable challenge because of the terrific performance capabilities of the human eye.<sup>(48)</sup> The central foveal area of the retina, having a resolution better than 1 arc min, answers the question of 'what' of pattern vision. The peripheral retina, having a resolution of about 20 arc min and being highly sensitive to image movement, answers 'where' the observer or the environment are moving. The field of view limits of human vision are:

- Fixed head and eyes: foveal 5° diameter; peripheral 190° horizontally (H) and 113° vertically (V).
- Moveable head and eyes: foveal 144° H by 170° V; peripheral 474° H by 170° V. Besides these spatial properties, other perceptual capabilities of human vision, like luminance/brightness, contrast, acuity and color are very important in flight simulator visual systems, see Section 6.2.

Together with the other body senses, see Section 4.5, the pilot's visual sensory system provides a visual/vestibular/kinesthetic interaction, which plays a vital role in the perception and control of motion in a closed loop control task.

Over the past 35 years a wide variety of visual simulation systems have been conceived and developed and many of these systems are in use to day. The visual systems which are now available and most widely used, are:

- Modelboard systems, using closed circuit television (CCTV) or a laser camera and laser projector.

- The shadowgraph system, using point light sources shining through transparent models.
- Computer generated image (CGI) systems, using a beam penetration color CRT, a TV monitor, a TV projector or a laser projector for presentation.

Figure 27 shows some of the typical components of visual systems and the combination of these components that have been employed.<sup>(59)</sup>

Modelboards still offer the richest scene content but they have fundamental limitations on operating volume. So, several modelboards are required to cover a reasonable operating volume, occupying a lot of space and incurring high running costs. The introduction of the laser camera system improved resolution and it may ultimately provide adequate depth of field by dynamic focusing.

The shadowgraph system has an even more restricted operating volume than the modelboard. Therefore, shadowgraphs are of value only for special applications, such as the current sky/ground projectors, and possibly for the generation of a large field of view for helicopter operations in and around hover.<sup>(50)</sup>

At present Computer Generated Image (CGI)-databases still lack detail and texture content, but rapid advances are being made. Realistic texture helps the pilot in perceiving his own motion relative to the outside world. Texture enhances the sense of proximity to inclined and vertical surfaces. Texture, updated at an acceptable rate, also offers the prospect that all the picture content needed for training may be available in the near future. Figure 28 shows a functional block diagram of a current CGI system,<sup>(51)</sup> using pipeline processing; specifically an SPX Image Generator built by Evans & Sutherland in the U.S.A. The front end of the system is a Multi-Processor unit (MP) that monitors and manages overall system load and controls special effects and moving objects. During a training exercise, it performs input processing of Host Computer data, defining airplane position and attitude. It also does database management, data being stored on disk and accessed by the MP. The database contains the 3D polygons (surfaces) defining objects, texture maps defining 2D surface patterns and color maps containing the palette of visible colors and intensities available for lights and objects. The data are generated in non-real time before a training session starts. During a training exercise, the MP in conjunction with the Object Manager (OM) determine from the momentary range, which objects appear in a channel. A channel is defined as a specific field of view to the pilot. The selected objects are ranked according to range and passed to the Geometric Processor (GP). The GP is responsible for clipping polygons to channel boundaries and for back face elimination. It performs the

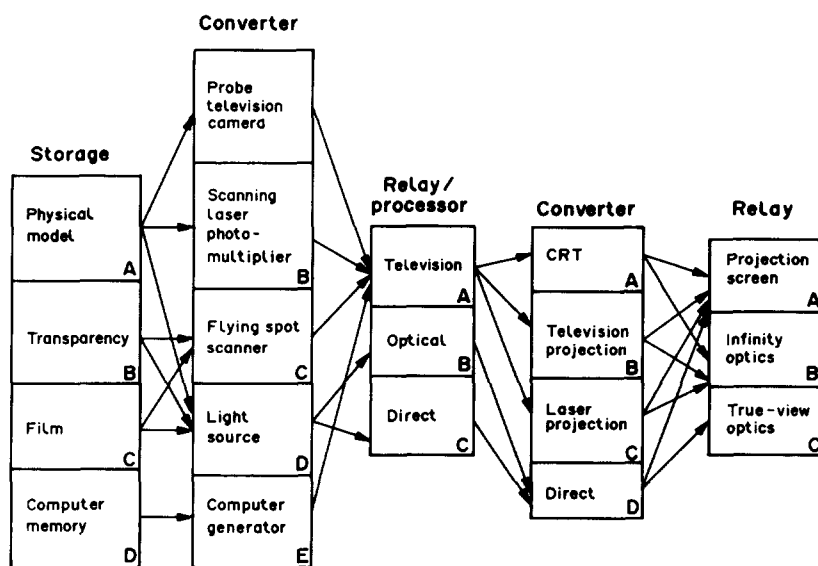


FIG. 27. Components of visual systems and some of the various combinations.

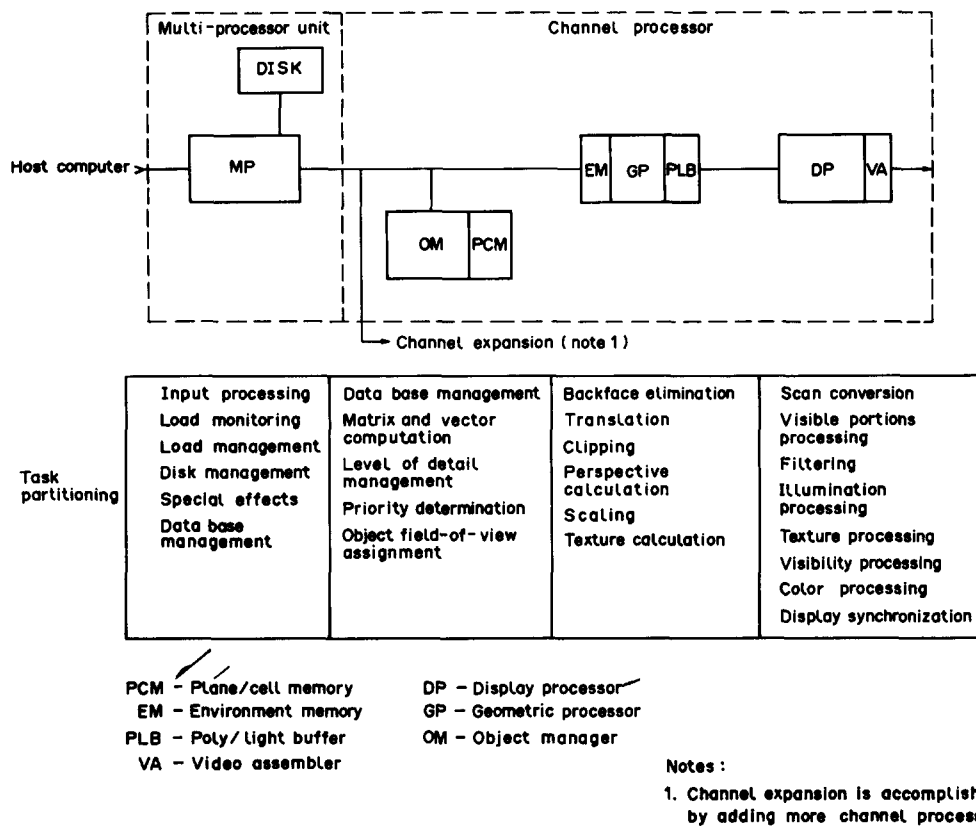


FIG. 28. Typical CGI functional block diagram.

critical transformations which ensure proper scene perspective. The final step in the pipeline is assembling a video image that forms a raster-scanned picture of lines and pixels. This is performed by the Display Processor (DP). The DP takes polygons and lights in perspective space and colors them as a function of: (1) assigned colour according to a specific colour map, (2) atmospheric visibility and (3) illumination effects such as sun angle, aircraft landing lights, etc. Coloration across the surface of a polygon need not be uniform, if it is assigned a shading function during database design. Finally the objects and lights are assembled in a video frame buffer (VA), anti-aliased to remove sampling artifacts, and scan-converted for display to the pilot.

For display devices, field of view and resolution are, for one channel and a given bandwidth, inversely related. The most common display device is the television monitor, in combination with an infinity display consisting of a beam-splitter and a spherical mirror (Fig. 29). It can achieve a resolution of about 3 arc min on a 60° diagonal field, using a 1000

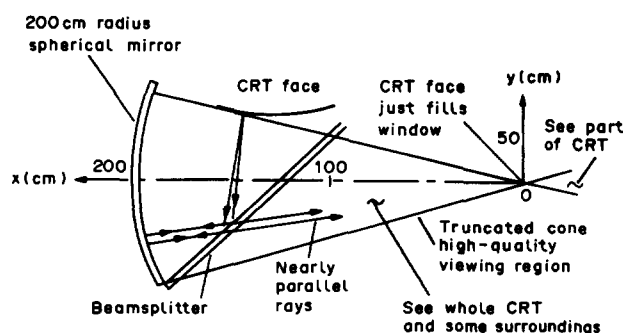


FIG. 29. Spherical mirror beam-splitter infinity display.

line TV display. The calligraphic display is an alternative to the conventional TV raster format. It is generally combined with raster insertions for specific features like runway markings and horizon glow as used in a night/dusk visual. The resolution of these displays is generally better than TV resolution, but a limited color spectrum is available using a beam penetration CRT.

A full color calligraphic projector is available, however, and several of them may be combined to give a wide angle, collimated field of view (WIDE) (Fig. 30). The laser projector offers significant improvements over current systems in both field of view and resolution,<sup>(46)</sup> primarily by virtue of its 100 MHz bandwidth. These projectors may be used with either modelboard or CGI-systems (Fig. 31).

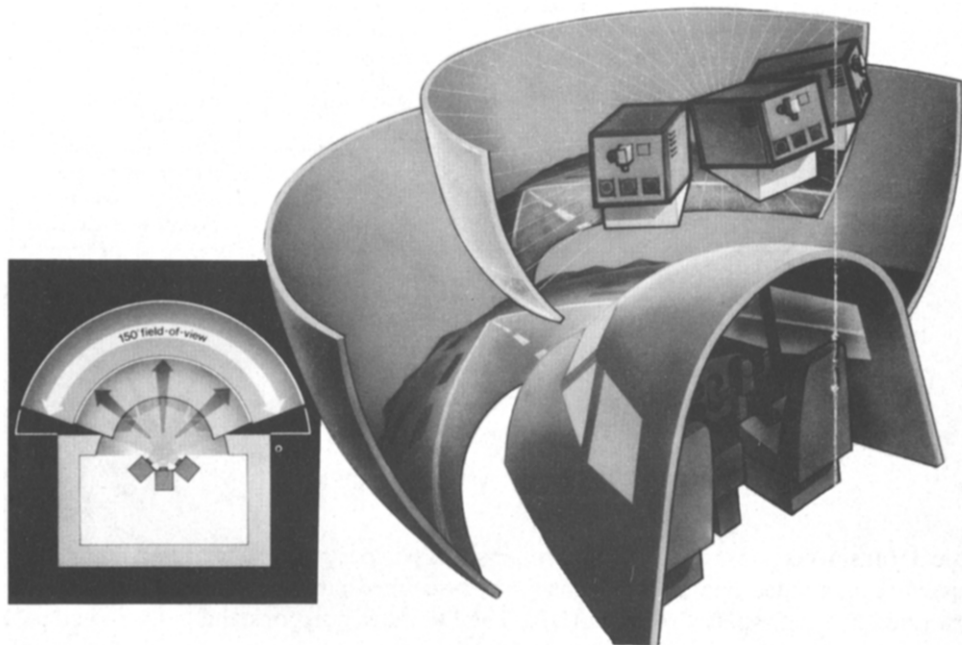


FIG. 30. Wide-angle Infinity Display Equipment (Rediffusion's WIDE).

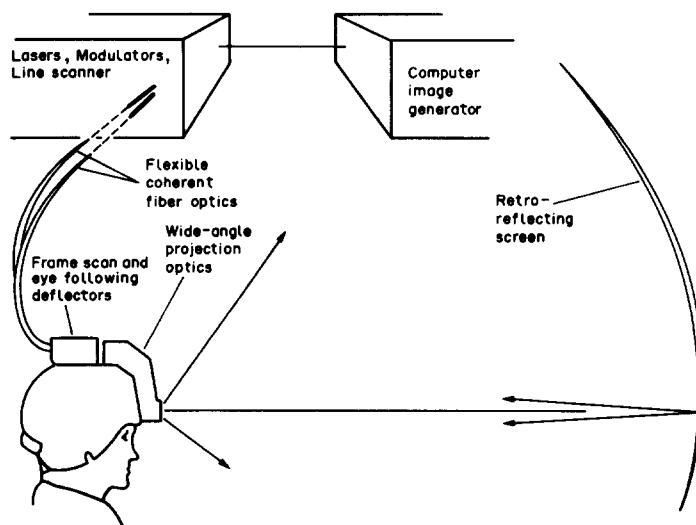


FIG. 31. Helmet-mounted laser projector concept.



FIG. 32. Fiber-optic helmet-mounted display. Reprinted with permission from the Royal Aeronautical Society.

One of the latest developments in display devices is the helmet-mounted visual display system,<sup>(49)</sup> developed by Canadian Aviation Electronics (CAE) for the Crew Station Research and Development Facility at NASA Ames Research Center. The purpose of this display device is to provide the pilot with an image, which dynamically tracks the head motions. The fiber-optic helmet-mounted display system (FOHMD) consists of a lightweight, custom-fitted helmet on which two 3-inch diameter pancake windows are mounted in front of the eyes (Fig. 32). These devices are compact, in-line, wide-field reflective infinity displays. They provide overlapping, full color images to each eye. The images are transferred to the helmet by two fiber-optic cables, from four high-brightness light valve projectors. An infrared head-tracker monitors head movements, using four cameras in the overhead structure, which scan a ring-array of Light Emitting Diodes (LED) on top of the helmet (Fig. 32). An angular rate sensor package, on the rear of the helmet, provides for lead predictions to compensate for CGI transport delays. The host computer calculates the head position and directs the CGI system to display the appropriate image, permitting an almost unlimited field of regard.

An urgent need exists for improved display devices to take advantage of improvements in CGI-systems. New techniques are being developed, e.g. matrices of LED or LCD and liquid crystal light valve projectors. The latter achieve 1 arc min resolution over a small and 4 arc min over a large field of view. Section 6.2 presents a more extensive treatment of visual system characteristics.

#### 4.5. MOTION SYSTEMS

Non-visual perception of motion relies on the following human sensors (Fig. 33):

- (1) The vestibular system, containing the semi-circular canals and the otoliths. Although the semi-circular canals are fundamentally overdamped angular accelerometers, their function is more analogous to that of rate gyros, sensing angular velocity of the head. However, at frequencies below 0.1 Hz, which are quite common in airplane motions, the semi-circular canal signals rather exhibit a phase lead making them closer to measures of

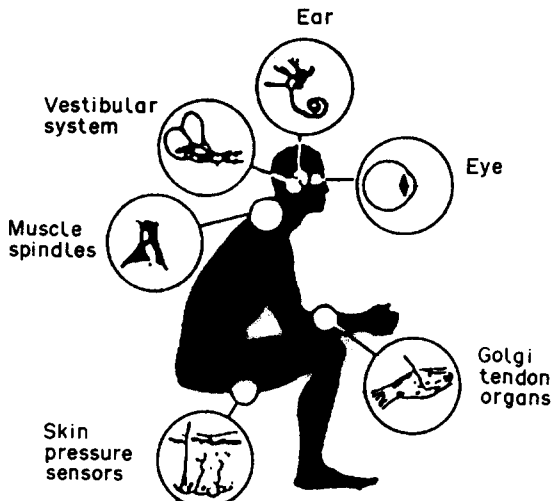


FIG. 33. The human sensors.

angular accelerations.<sup>(54)</sup> The otoliths play the role of linear accelerometers sensing specific forces, see Section 7.3. Like any accelerometer, they are incapable of distinguishing between gravitational acceleration and linear acceleration with respect to inertial space.

- (2) Pressure sensors consist of both surface tactile receptors in the outer layers of the skin, and deep pressure sensors, located well below the skin surface. They aid the otoliths in sensing specific forces and their output forms the basis of 'flying by the seat of the pants'.
- (3) Proprioceptive and kinesthetic sensors in the muscles signal to the central nervous system the relative positions of parts of the body, as well as their movements. Three basic types of sensory mechanisms are involved: the muscle spindles sensing muscle length, the Golgi tendon organs sensing muscle tension and the combination of the proprioceptive senses permitting subjects to perceive forces acting on the human body.

The non-visual sensors are less precise than the visual sensory system. However, they may respond more rapidly, providing *lead* information, and do not require direct attention of the subject. The above characteristics of the non-visual sensors permit the simulation of motion in a very limited space, using simulator cockpit motion systems, see Section 7.

Nevertheless, faithful reproduction of aircraft motion may need relatively large travel of the motion system. That is why research institutes like NASA Ames and RAE Bedford use large travel systems in their research and development simulators, see Section 3.3.1. The major users of 6 DOF motion systems, the airlines, apply to their training simulators so-called synergistic motion systems (Fig. 34). The six actuators with a travel of about 1.50 m each, commonly used in these motion systems, have been provided with hydrostatic bearings<sup>(20)</sup> since about 1977. This development resulted in large improvements in the dynamic characteristics of these motion systems.<sup>(55)</sup> The main criticism of synergistic motion systems, compared to systems having independent travel for each degree of freedom (e.g. the FSAA, Section 3.3.1), is that independent systems can achieve the full travel in all axes simultaneously. Synergistic systems, however, suffer severe restrictions if axes are used in combination.

British Aerospace at Warton acquired a small synergistic 6 DOF motion system with a jack travel of about 0.6 m for integration with their research and development fighter simulator, located in a dome.<sup>(47)</sup> The aim is a compact installation with good dynamic performance to simulate small responsive airplanes. The primary functions of the translational modes of this motion system are to simulate vibrations (buffet, runway-rumble, turbulence etc.). The rotational modes provide initial angular accelerations and the change in gravity vector with aircraft attitude.

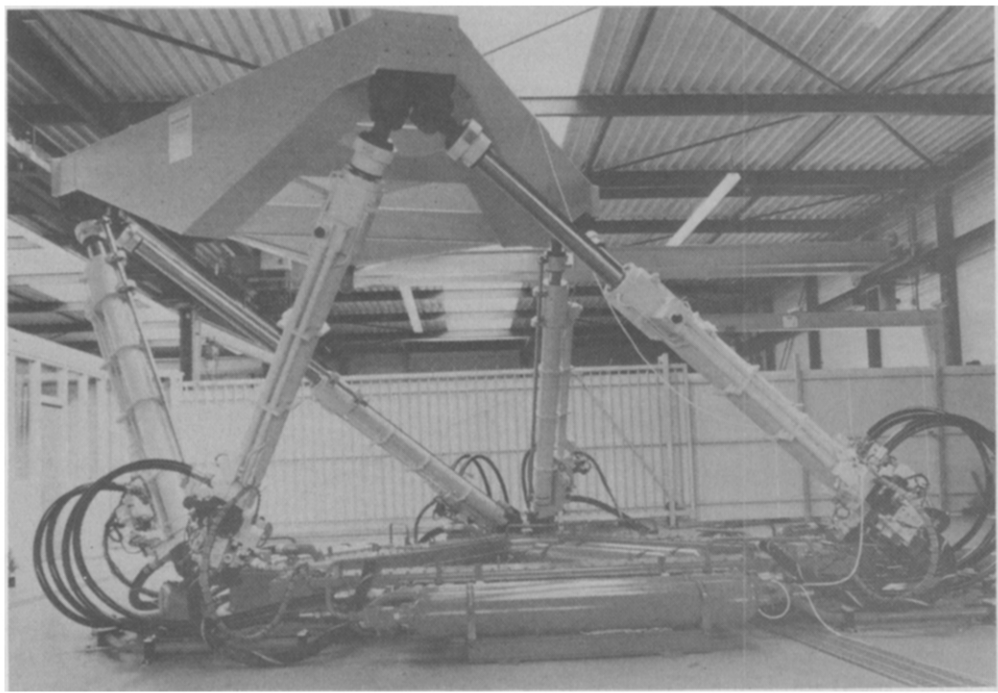


FIG. 34. Second generation synergistic hydrostatic motion system (Hydraudyne).

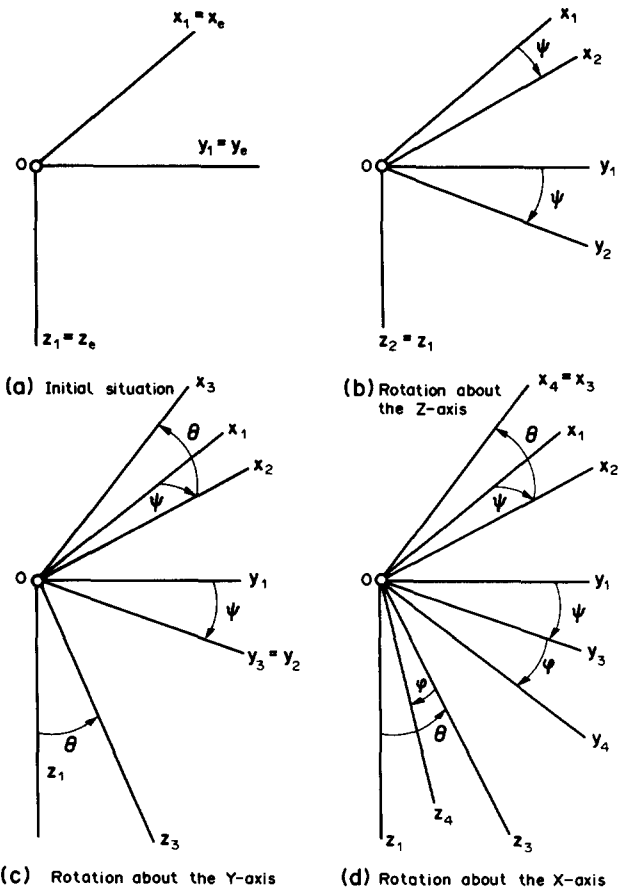


FIG. 35. The altitude of the airplane relative to the earth.

A modern, state-of-the-art motion system, built by Hydrauldyne Systems & Engineering, Boxtel, The Netherlands (Fig. 34) for the National Aerospace Laboratory, NLR, in Amsterdam,<sup>(29)</sup> uses advanced technology actuators having a travel of 1.85 m. These actuators have been designed in cooperation with Delft University of Technology,<sup>(20)</sup> Faculty of Mechanical Engineering. Inside the actuators, a spine is mounted. As a result, the upper and lower piston areas are equal, resulting in symmetrical flow for accurate control (no discontinuities at motion reverse), and higher lateral stiffness. Section 7 describes motion hardware dynamic characteristics and motion cue generation in detail.

## 5. MATHEMATICAL MODELS FOR FLIGHT SIMULATION

### 5.1. GENERAL

The basis of any flight simulator—as mentioned before—is the mathematical model, including the data package describing the characteristic features of the airplane to be simulated. Airplane mathematical models may be obtained from theoretical analysis, windtunnel measurements and flight tests.

This chapter presents the principles of mathematical modelling of the aerodynamic, flight control, propulsion, ground-handling and environmental characteristics of the airplane, starting from the most general equations of airplane motion. Linearization of these equations results in the small perturbation equations, valid only for small deviations from a certain airspeed and altitude. The simulation of a complete mission, however, from take-off to landing, needs the non-linear equations of motion, covering the full flight envelope.

Atmospheric turbulence, wind and wind-shear disturb the aircraft motions. Models describing these phenomena are therefore essential in flight simulation.

Ground-handling simulation became an important item, since the arrival of visual simulation systems. For the simulation of taxiing, take-off and landing, the mathematical model of the aircraft-undercarriage is indispensable.

In order to obtain an airplane mathematical model and data package for flight simulation, a possible option is dynamic model identification using a flight test instrumented aircraft.

### 5.2. EQUATIONS OF MOTION OF AN AIRPLANE

The motions of an airplane are affected by the external forces ( $F$ ) and moments ( $M$ ) resulting from flight through the atmosphere, engine thrust and landing gear forces during take-off and landing, acting on the airplane. The airplane motions are calculated using the equations of motion as derived from Newton's laws:<sup>(89)</sup>

$$dF = \frac{d}{dt}(dm \cdot V) \quad (5.1)$$

where point mass  $dm$  moves with time varying velocity  $V$  under the influence of a force  $dF$ , and:

$$dM = \frac{d}{dt}(dm r \times V), \quad (5.2)$$

where the moment of the force about a fixed point  $dM$  is equal to the time derivative of the angular momentum of the body relative to that same fixed point.

The equations of motion of an airplane can be derived on the basis of the above two expressions, by adding up the forces acting on all parts of the airplane as well as the moments due to these forces about the center of gravity of the airplane.

The resulting general equations of motion of an airplane in the body axes reference frame read:<sup>(75)</sup>

$$F_x = -W \sin \theta \quad + X = m \cdot (\dot{u} + qw - rv)$$

$$F_y = W \cos \theta \sin \varphi \quad + Y = m \cdot (\dot{v} + ru - pw)$$

$$\begin{aligned}
 F_z &= W \cos \theta \cos \varphi + Z = m \cdot (\dot{w} + p v - q u) \\
 M_x &= L = I_x \dot{p} + (I_z - I_y) q r - J_{xz} (\dot{r} + p q) \\
 M_y &= M = I_y \dot{q} + (I_x - I_z) r p + J_{xz} (p^2 - r^2) \\
 M_z &= N = I_z \dot{r} + (I_y - I_x) p q - J_{xz} (\dot{p} - r q). \quad (5.3)
 \end{aligned}$$

To the Eqs (5.3) the kinematic Eqs (5.4) should be added, expressing the relations between the rates of change of the airplane's attitude angles and the angular velocities about the airplane body axes:

$$\begin{aligned}
 \dot{\psi} &= q \frac{\sin \varphi}{\cos \theta} + r \frac{\cos \varphi}{\cos \theta} \\
 \dot{\theta} &= q \cos \varphi - r \sin \varphi \\
 \dot{\varphi} &= p + q \sin \varphi \tan \theta + r \cos \varphi \tan \theta. \quad (5.4)
 \end{aligned}$$

Figure 35 shows the successive rotations to obtain the Euler angles  $\psi$ ,  $\theta$ , and  $\varphi$ , respectively, determining the attitude of the airplane relative to the Earth. In order to avoid singularities when pitch attitude  $\theta$  reaches 90 degrees, the so-called 'quaternions' are used for defining the orientation of the airplane.<sup>(36)</sup> In particular, military airplane simulators use these quaternions.

The above equations describe the most general motions an airplane can perform and are based on the following restrictive assumptions:

- (1) The airplane's mass is constant in the time interval during which the motions of the airplane are studied.
- (2) The airplane is a rigid body in the motion under consideration.
- (3) The mass-distribution of the airplane is symmetric relative to the  $XOZ$ -plane.
- (4) The rotation of the earth in space, as well as the curvature of the earth's surface are negligible.

### 5.2.1. Small Perturbation Equations

The purpose of using the small perturbation equations of motion is that, because of their linearized form, they are suitable to treatment by a number of analytical techniques. Examples of these techniques are the use of Transfer Functions, Laplace and Fourier Transforms, and the computation of eigenvalues, eigenvectors and root locus plots.<sup>(71)</sup> In the design stage of a new aircraft these analytical techniques present the possibility to establish data on the stability and handling qualities of the aircraft, using simplified mathematical models.

The small perturbation equations of motion may be applied, if the motion of the airplane deviates only to a small extent from steady, trimmed, symmetrical flight. The permissible magnitudes of the small deviations are those for which linearization of the equations about the steady flight condition results in a sufficiently true replication of the actual airplane motions. Many comparisons of response calculations with flight test measurements have shown that linearization indeed results in a useful range of motions about the steady flight condition.

Another simplifying characteristic of the small perturbation equations of motion is that no aerodynamic coupling exists between the symmetric and asymmetric degrees of freedom, as long as the deviations remain sufficiently small. This results in the possibility to separate the small perturbation equations in the equations for the *symmetric* airplane motions and those for the *asymmetric* motions of the airplane. As the aerodynamic forces and moments in these equations are usually expressed in non-dimensional coefficients, it is common practice to use the equations in a non-dimensional form. To this end, the inertial characteristics and the time scale are also made non-dimensional.<sup>(75)</sup>

The resulting non-dimensional equations for the symmetric motions in the stability axes reference frame, as derived in Ref. 75, read:

$$\begin{aligned}
 & (C_{X_u} - 2\mu_c D_c) \dot{u} + C_{X_\alpha} \cdot \alpha + C_{Z_0} \cdot \theta + C_{X_q} \cdot \delta_e = 0 \\
 & C_{Z_u} \cdot \dot{u} + \{C_{Z_\alpha} + (C_{Z_\dot{\alpha}} - 2\mu_c) D_c\} \cdot \alpha - C_{X_0} \cdot \theta + (C_{Z_q} + 2\mu_c) \cdot \frac{q\bar{c}}{V} + C_{Z_\delta} \cdot \delta_e = 0 \\
 & \quad - D_c \theta \quad + \quad \frac{q\bar{c}}{V} \quad = 0 \\
 & C_{m_u} \cdot \dot{u} + (C_{m_\alpha} + C_{m_\dot{\alpha}} \cdot D_c) \cdot \alpha + (C_{m_q} - 2\mu_c K_Y^2 D_c) \cdot \frac{q\bar{c}}{V} + C_{m_\delta} \cdot \delta_e = 0
 \end{aligned} \tag{5.5}$$

or, using matrices:

$$\begin{vmatrix} C_{X_u} - 2\mu_c D_c & C_{X_\alpha} & C_{Z_0} & C_{X_q} \\ C_{Z_u} & C_{Z_\alpha} + (C_{Z_\dot{\alpha}} - 2\mu_c) D_c & -C_{X_0} & C_{Z_q} + 2\mu_c \\ 0 & 0 & -D_c & 1 \\ C_{m_u} & C_{m_\alpha} + C_{m_\dot{\alpha}} \cdot D_c & 0 & C_{m_q} - 2\mu_c K_Y^2 D_c \end{vmatrix} \cdot \begin{vmatrix} \dot{u} \\ \alpha \\ \theta \\ \frac{q\bar{c}}{V} \end{vmatrix} = \begin{vmatrix} -C_{X_\delta} \\ -C_{Z_\delta} \\ 0 \\ -C_{m_\delta} \end{vmatrix} \cdot \delta_e. \tag{5.6}$$

The non-dimensional equations for the asymmetric motions in stability axes, as derived in Ref. 75, read:

$$\begin{aligned}
 & \{C_{Y_\beta} + (C_{Y_\dot{\beta}} - 2\mu_b) D_b\} \beta + C_{Y_p} \cdot \frac{pb}{2V} + (C_{Y_r} - 4\mu_b) \cdot \frac{rb}{2V} + C_{Y_{\delta_a}} \cdot \delta_a + C_{Y_{\delta_r}} \cdot \delta_r = 0 \\
 & -\frac{1}{2} D_b \cdot \varphi + \frac{pb}{2V} = 0 \\
 & C_{l_p} \cdot \beta + (C_{l_p} - 4\mu_b K_X^2 D_b) \cdot \frac{pb}{2V} + (C_{l_r} + 4\mu_b K_{XZ} D_b) \cdot \frac{rb}{2V} + C_{l_{\delta_a}} \cdot \delta_a \\
 & + C_{l_{\delta_r}} \cdot \delta_r = 0 \\
 & (C_{n_p} + C_{n_\dot{\beta}} D_b) \cdot \beta + (C_{n_p} + 4\mu_b K_{XZ} D_b) \cdot \frac{pb}{2V} + (C_{n_r} - 4\mu_b K_Z^2 D_b) \cdot \frac{rb}{2V} + C_{n_{\delta_a}} \cdot \delta_a \\
 & + C_{n_{\delta_r}} \cdot \delta_r = 0
 \end{aligned} \tag{5.7}$$

Using matrix notation, the Eqs (5.7) are written as:

$$\begin{aligned}
 & \begin{vmatrix} C_{Y_\beta} + (C_{Y_\dot{\beta}} - 2\mu_b) D_b & C_L & C_{Y_p} & C_{Y_r} - 4\mu_b \\ 0 & -\frac{1}{2} D_b & 1 & 0 \\ C_{l_p} & 0 & C_{l_p} - 4\mu_b K_X^2 D_b & C_{l_r} + 4\mu_b K_{XZ} D_b \\ C_{n_p} + C_{n_\dot{\beta}} D_b & 0 & C_{n_p} + 4\mu_b K_{XZ} D_b & C_{n_r} - 4\mu_b K_Z^2 D_b \end{vmatrix} \cdot \begin{vmatrix} \beta \\ \varphi \\ \frac{pb}{2V} \\ \frac{rb}{2V} \end{vmatrix} \\
 & = \begin{vmatrix} -C_{Y_{\delta_a}} \\ 0 \\ -C_{l_{\delta_a}} \\ -C_{n_{\delta_a}} \end{vmatrix} \cdot \delta_a + \begin{vmatrix} C_{Y_{\delta_r}} \\ 0 \\ -C_{l_{\delta_r}} \\ -C_{n_{\delta_r}} \end{vmatrix} \cdot \delta_r
 \end{aligned} \tag{5.8}$$

TABLE 1. STABILITY AND CONTROL DERIVATIVES OF THE DHC-2 'BEAVER' AIRPLANE

| Airplane/flight condition                   | Stability derivatives symmetric motion | Stability derivatives asymmetric motion |
|---|--|---|
| $m = 2288.231 \text{ kg}$                   | $C_{X_0} = 0$                          | $C_{Y_p} = -0.76776$                    |
| $x_{cg} = 0.38 \bar{c}$                     | $C_{X_a} = -0.166576$                  | $C_{Y_r} = -0.07999$                    |
| $S = 23.23 \text{ m}^2$                     | $C_{X_s} = 0.51761$                    | $C_{Y_p} = -0.12399$                    |
| $C_L = 0.93177$                             | $C_{X_d} = 0$                          | $C_{Y_r} = 0.36757$                     |
| $\bar{c} = 1.5875 \text{ m}$                | $C_{X_x} = -1.09824$                   | $C_{Y_{a_s}} = -0.02956$                |
| $2\mu_c = 121.20$                           | $C_{X_e} = -0.05780$                   | $C_{Y_{a_s}} = 0.11628$                 |
| $K_f^2 = 1.2015$                            | $C_{Z_0} = -0.93177$                   | $C_{I_p} = -0.06047$                    |
| $h = 6000 \text{ ft SA}$                    | $C_{Z_u} = -1.61227$                   | $C_{I_r} = 0$                           |
| $\gamma_0 = 0^\circ$                        | $C_{Z_d} = -5.49424$                   | $C_{I_p} = -0.52201$                    |
| $V = 45 \text{ m/sec}$                      | $C_{Z_x} = 0$                          | $C_{I_r} = 0.14711$                     |
| $\Delta p_i / \frac{1}{2} \rho V^2 = 0.566$ | $C_{Z_a} = -2.82629$                   | $C_{I_{p_s}} = -0.11051$                |
| $b = 14.63 \text{ m}$                       | $C_{Z_s} = -0.40141$                   | $C_{I_{p_s}} = -0.00504$                |
| $2\mu_b = 13.16$                            | $C_{m_a} = 0.11179$                    | $C_{n_p} = 0.01462$                     |
| $K_f^2 = 0.01114$                           | $C_{m_e} = -1.18687$                   | $C_{n_p} = 0$                           |
| $K_Z^2 = 0.02261$                           | $C_{m_d} = 0$                          | $C_{n_p} = -0.08420$                    |
| $K_{xz} = -0.001450$                        | $C_{m_q} = -15.53530$                  | $C_{n_r} = -0.13398$                    |
|   | $C_{m_b} = -1.91846$                   | $C_{n_{A_s}} = 0.01217$                 |
|   |  | $C_{n_{A_s}} = -0.08279$                |

In both sets of Eqs (5.6) and (5.8) the stability and control derivatives as well as the inertia parameters are constants for a given aircraft configuration and weight, airspeed and altitude. Table 1 presents an example of the stability and control derivatives and the non-dimensional inertia characteristics of the DHC-2 'BEAVER' aircraft, see Section 5.2.2.

### 5.2.2. Non-Linear Equations Covering the Complete Flight Envelope

In real-time flight simulation the non-linear equations of motion, covering the complete flight envelope are used, starting from the total force and moment Eqs (5.3).

Rearranging the Eqs (5.3) and introducing the inertia parameters  $P_{pq}$ ,  $P_{qr}$ ,  $P_n$ ,  $P_l$ ,  $Q_{pp}$ ,  $Q_{pr}$ ,  $Q_m$ ,  $R_{pq}$ ,  $R_{qr}$ ,  $R_n$  and  $R_l$  results in the following equations, where all time derivatives appear in the lefthand side (see subroutine FINER in Section 4.2):

$$\begin{aligned}
 \dot{u} &= \frac{X}{m} & -g \cdot \sin \theta & -qw & +rv \\
 \dot{v} &= \frac{Y}{m} & +g \cdot \cos \theta \cdot \sin \varphi & +pw & -ru \\
 \dot{w} &= \frac{Z}{m} & +g \cdot \cos \theta \cdot \cos \varphi & -pv & +qu \\
 \dot{p} &= P_{pq} \cdot pq & +P_{qr} \cdot qr & +P_n \cdot N & +P_l \cdot L \\
 \dot{q} &= Q_{pp} \cdot p^2 & +Q_{pr} \cdot pr & +Q_{rr} \cdot r^2 & +Q_m \cdot M \\
 \dot{r} &= R_{pq} \cdot pq & +R_{qr} \cdot qr & +R_n \cdot N & +R_l \cdot L
 \end{aligned} \quad (5.9)$$

where:

$$\begin{aligned}
 P_{pq} &= \frac{(I_x - I_y + I_z) \cdot J_{xz}}{I_{rr}}, \quad P_{qr} = \frac{[(I_y - I_z) \cdot I_z - J_{xz}^2]}{I_{rr}}, \quad P_n = \frac{J_{xz}}{I_{rr}}, \quad P_l = \frac{I_z}{I_{rr}}, \quad Q_{pp} = \frac{-J_{xz}}{I_y}, \\
 Q_{pr} &= \frac{(I_z - I_x)}{I_y}, \quad Q_{rr} = \frac{J_{xz}}{I_y}, \quad Q_m = \frac{1}{I_y}, \quad R_{pq} = \frac{[(I_x - I_y) \cdot I_x + J_{xz}^2]}{I_{rr}}, \quad R_{qr} = \frac{(I_y - I_z - I_x) \cdot J_{xz}}{I_{rr}}, \\
 R_n &= \frac{I_x}{I_{rr}}, \quad R_l = \frac{J_{xz}}{I_{rr}} \text{ and } I_{rr} = (I_x I_z - J_{xz}^2).
 \end{aligned}$$

From the components  $u$ ,  $v$  and  $w$  of the airspeed  $V$  of the airplane c.g. relative to the ambient air, the components of  $V$  along the axes of the earth reference frame are

computed:<sup>(75)</sup>

$$\begin{aligned}\dot{X}_e &= V_{\text{north}} = \{u \cos \theta + (v \sin \varphi + w \cos \varphi) \sin \theta\} \cos \psi \\ &\quad - (v \cos \varphi - w \sin \varphi) \sin \psi \\ \dot{Y}_e &= V_{\text{east}} = \{u \cos \theta + (v \sin \varphi + w \cos \varphi) \sin \theta\} \sin \psi \\ &\quad + (v \cos \varphi - w \sin \varphi) \cos \psi \\ \dot{Z}_e &= V_{\text{vert}} = -u \sin \theta + (v \sin \varphi + w \cos \varphi) \cos \theta.\end{aligned}\quad (5.10)$$

The Eqs (5.4), (5.9) and (5.10) are the complete set of the equations of motion of an airplane; however, they are independent of a *particular* airplane. These equations are solved in subroutine FDERI, see Section 4.2 and Fig. 25. As an example, Fig. 36 shows the structured-flowchart of FDERI and the Fortran 77 source-listing is available to interested readers on request.

The external forces  $X$ ,  $Y$  and  $Z$ , and moments  $L$ ,  $M$  and  $N$  in Eqs (5.9) are those generated by the aerodynamics, engine and landing gear. In aeronautical engineering it is customary

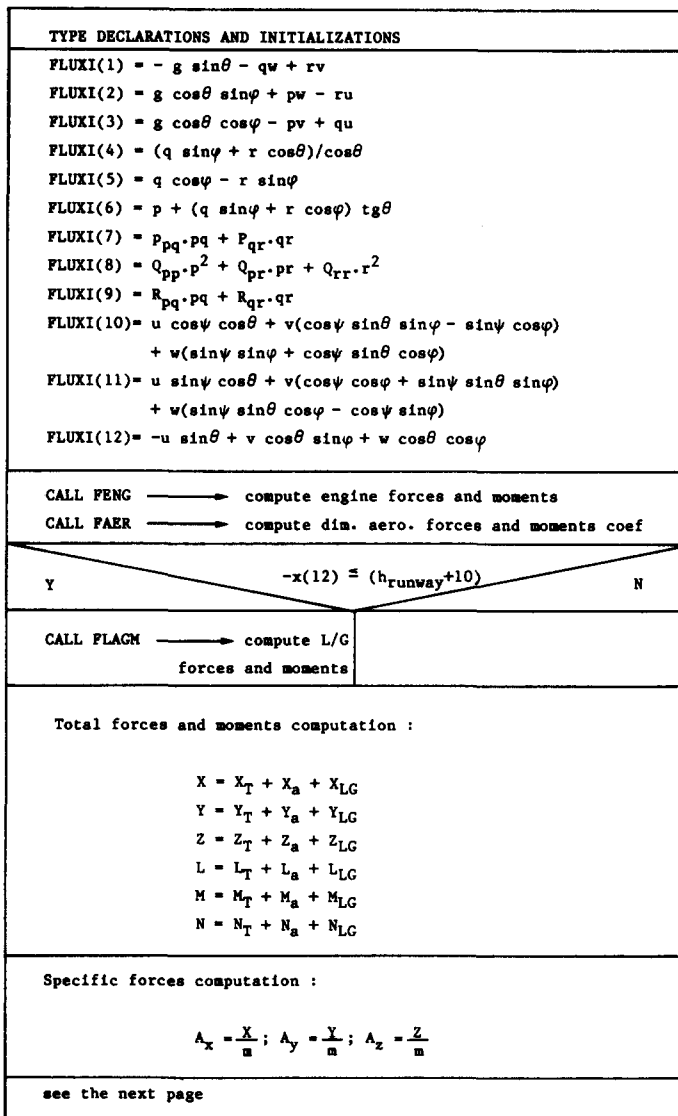


FIG. 36. Structured-flowchart of the subroutine FDERI.

```

State derivative computation :
XDOT(1) = FLUXI(1) + AX
XDOT(2) = FLUXI(2) + Ay
XDOT(3) = FLUXI(3) + Ax
XDOT(4) = FLUXI(4)
XDOT(5) = FLUXI(5)
XDOT(6) = FLUXI(6)
XDOT(7) = FLUXI(7) + L.INERT(1,4) + N.INERT(1,3)
XDOT(8) = FLUXI(8) + M.INERT(2,4)
XDOT(9) = FLUXI(9) + L.INERT(3,4) + N.INERT(3,3)
XDOT(10)= FLUXI(10)
XDOT(11)= FLUXI(11)
XDOT(12)= FLUXI(12)

n,  $\dot{\alpha}$  and  $\dot{\beta}$  computation :

NLF = -  $\frac{A_z}{g_0}$  ; UW = u2 + v2
ALPHADOT =  $\frac{(\dot{w} \cdot u - \dot{u} \cdot w)}{UW}$ 
BETADOT =  $\frac{(\dot{v} \cdot UW - v(u \cdot \dot{u} + w \cdot \dot{w}))}{(u^2 + v^2 + w^2) \cdot \sqrt{UW}}$ 

RETURN

```

FIG. 36. (Contd.)

practice to relate the aerodynamic forces  $X_a$ ,  $Y_a$  and  $Z_a$ , and moments  $L_a$ ,  $M_a$  and  $N_a$  to the corresponding dimensionless force and moment coefficients:  $C_{X_a}$ ,  $C_{Y_a}$ ,  $C_{Z_a}$ ,  $C_{l_a}$ ,  $C_{m_a}$  and  $C_{n_a}$ , writing:

$$\begin{aligned}
X_a &= C_{X_a} \frac{1}{2} \rho V^2 S \\
Y_a &= C_{Y_a} \frac{1}{2} \rho V^2 S \\
Z_a &= C_{Z_a} \frac{1}{2} \rho V^2 S \\
L_a &= C_{l_a} \frac{1}{2} \rho V^2 S b \\
M_a &= C_{m_a} \frac{1}{2} \rho V^2 S \bar{c} \\
N_a &= C_{n_a} \frac{1}{2} \rho V^2 S b.
\end{aligned} \tag{5.11}$$

The aerodynamic forces and moments (5.11) result from flight through a volume of ambient air *at rest*, relative to earth. Adding the contributions of the forces and moments due to atmospheric turbulence ( $g$ ), engine operation ( $T$ ) and landing gear ground contact (LG), results in the following general equations for the external forces and moments in body axes:

$$\begin{aligned}
X &= \frac{1}{2} \rho V^2 S (C_{X_a} + C_{X_g} + C_{X_T}) + X_{LG} \\
Y &= \frac{1}{2} \rho V^2 S (C_{Y_a} + C_{Y_g} + C_{Y_T}) + Y_{LG} \\
Z &= \frac{1}{2} \rho V^2 S (C_{Z_a} + C_{Z_g} + C_{Z_T}) + Z_{LG}
\end{aligned}$$



FIG. 37. The De Havilland DHC-2 BEAVER experimental aircraft of Delft University of Technology.

$$\begin{aligned} L &= \frac{1}{2} \rho V^2 S b (C_{l_a} + C_{l_g} + C_{l_T}) + L_{LG} \\ M &= \frac{1}{2} \rho V^2 S c (C_{m_a} + C_{m_g} + C_{m_T}) + M_{LG} \\ N &= \frac{1}{2} \rho V^2 S b (C_{n_a} + C_{n_g} + C_{n_T}) + N_{LG}. \end{aligned} \quad (5.12)$$

Equations (5.12) are solved in subroutine FDERI as well, see Fig. 36.

As an example the aerodynamic model and engine model of the De Havilland DHC-2 BEAVER laboratory aircraft of DUT (Fig. 37) are described below. The data package used in these models is based on flight tests throughout the normal flight envelope of the airplane.<sup>(90)</sup> Sections 5.3 and 5.4 describe the contributions to the external forces and moments of atmospheric turbulence and windshear, and of the landing gear model respectively.

#### 5.2.2.1. The aerodynamic model

The DHC-2 BEAVER is a seven-seat, single combustion engine, high-wing all-metal aircraft, having a maximum take-off weight of 22.800 N. Some general data of this airplane are presented in Table 2, and Table 3 presents the inertia data on which the aerodynamic model is based. In the aerodynamic model, presented below, the effect of compressibility is neglected, as airspeed is assumed to be low. Also scale effects are not taken into account since, at a relatively high Reynolds number, the effect of Reynolds number variations, as occurring in flight, is considered negligible.

To present non-linear aerodynamic data, two possible methods are available, i.e. the table look-up method and the polynomial fit to data.

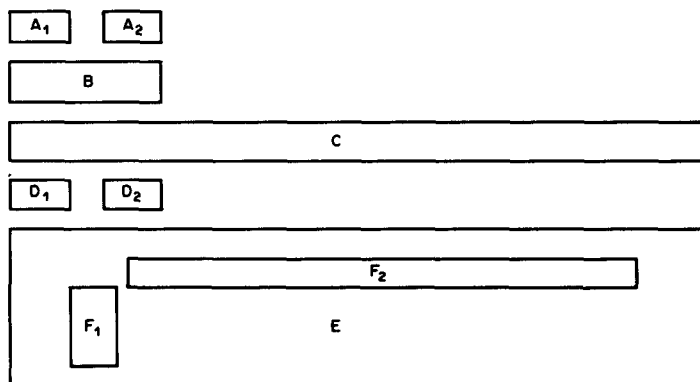
Using the table look-up method, a table of values of a dependent variable as a function of one or more independent variables is given. Figure 38 shows how the data may be arranged. In this figure the break point sets  $F_1$  and  $F_2$  present the tables of values of the independent variables and  $E$  contains the values of the dependent variable. As an example, the lift coefficient  $C_L$  as a function of the angle of attack  $\alpha$  and flap deflection  $\delta_f$  of the DHC-2 BEAVER is shown in Table 4 and Fig. 39. The value of  $C_L$  for any value of  $\alpha$  and  $\delta_f$  is obtained by linear interpolation, see subroutines FDABRD and FTABINT in Section 4.2.

TABLE 2. GENERAL AIRCRAFT DATA OF THE DHC-2 'BEAVER' PH-VTH

|  |  |
|--|--|
| Manufacturer                           | The De Havilland Aircraft of Canada Ltd                                    |
| Serial no.                             | 1244   |
| Type                                   | Seven-seat, single engine, high-wing all-metal aircraft.                   |
| Wing span ( $b$ )                      | 14.63 m  |
| Wing area ( $S$ )                      | 23.23 m <sup>2</sup>   |
| Mean aerodynamic chord ( $c$ )         | 1.5875 m   |
| Wing sweep                             | 0°   |
| Wing dihedral                          | 1°   |
| Wing profile                           | NACA 64 A 416  |
| Fuselage length                        | 9.22 m   |
| Max. take-off weight                   | 2315 kgf = 22800 N   |
| Empty weight                           | 1520 kgf = 14970 N   |
| Engine                                 | Pratt and Whitney Wasp Jr  |
| Type                                   | R-985  |
| Max. power                             | 450 hp at $n = 2300$ RPM, $p_z = 26$ inch Hg, $h = 750$ m                  |
| Airscrew                               | Hamilton Standard  |
| Type                                   | Two-bladed metal regulator propeller                                       |
| Diameter                               | 2.59 m   |
| Total contents of fuel tanks           | 115 imp. gallon = 521 l  |
| Fuselage front tank                    | 131 l = 0.1318 m <sup>3</sup>  |
| Fuselage center tank                   | 131 l = 0.1318 m <sup>3</sup>  |
| Fuselage rear tank                     | 95 l = 0.1318 m <sup>3</sup>   |
| Wing tiptanks                          | 2 × 82 l = 2 × 0.0818 m <sup>3</sup>                                       |
| Most forward admissible c.g.-position  | 17.36% m.a.c. at 1725 kgf = 16989 N<br>29.92% m.a.c. at 2315 kgf = 22800 N |
| Most backward admissible c.g.-position | 40.24% m.a.c.  |

TABLE 3. BEAVER DATA ON WHICH THE AERODYNAMIC MODEL IS BASED

$$\begin{aligned}
 x_{c.g.} &= 0.5996 \text{ m} \\
 y_{c.g.} &= 0.0 \text{ m} \\
 z_{c.g.} &= -0.8851 \text{ m} \\
 I_x &= 5368.39 \text{ kgm}^2 \\
 I_y &= 6928.93 \text{ kgm}^2 \\
 I_z &= 11158.75 \text{ kgm}^2 \\
 J_{xz} &= 117.64 \text{ kgm}^2 \\
 m &= 2288.231 \text{ kg} \\
 h &= 1828.8 \text{ m} \\
 \rho &= 1.024 \text{ kg/m}^3
 \end{aligned}$$

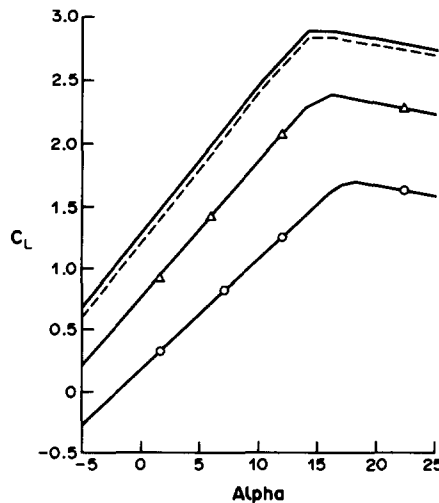


- A : Breakpoint set number
- B : Address of the data
- C : Description of the data
- D : Dimension of the data
- E : The data
- F : Breakpoint set
- 1 : Row      2 : Column

FIG. 38. Data arrangement.

TABLE 4.  $C_L$  AS A FUNCTION OF  $\alpha$  AND  $\delta_f$ 

| $\alpha$<br>(degrees) | $\delta_f$ |       |       |       |
|-----------------------|------------|-------|-------|-------|
|                       | 0          | 1     | 2     | 3     |
| -5.0                  | -0.270     | 0.220 | 0.60  | 0.680 |
| 10.0                  | 1.082      | 1.88  | 2.42  | 2.47  |
| 14.0                  | 1.440      | 2.28  | 2.826 | 2.88  |
| 16.0                  | 1.62       | 2.38  | 2.826 | 2.88  |
| 17.4                  | 1.712      | 2.364 | 2.800 | 2.860 |
| 25.0                  | 1.58       | 2.22  | 2.68  | 2.73  |

FIG. 39.  $C_L$  as a function of  $\alpha$  and  $\delta_f$ . ○ Flaps up; ▷ flap setting for climb; --- flap setting for take-off; — flap setting for landing.

If it is possible to fit the curve, describing the dependent variable, with a first, second or third degree polynomial, a simple continuous expression is available for computation.

Using the polynomial fit to data, the non-linear aerodynamic model of the DHC-2 BEAVER, in terms of the dimensionless force and moment coefficients in Eqs(5.12) becomes:

$$\begin{aligned}
 C_{X_a} &= C_{X_0} + C_{X_\alpha} \cdot \alpha + C_{X_{\alpha^2}} \cdot \alpha^2 + C_{X_{\alpha^3}} \cdot \alpha^3 + \\
 &\quad C_{X_q} \cdot \frac{q\bar{c}}{V} + C_{X_{\delta_r}} \cdot \delta_r + C_{X_{\delta_f}} \cdot \delta_f + C_{X_{\delta_a}} \cdot \alpha \cdot \delta_f \\
 C_{Y_a} &= C_{Y_0} + C_{Y_\beta} \cdot \beta + C_{Y_p} \cdot \frac{pb}{2V} + C_{Y_r} \cdot \frac{rb}{2V} + \\
 &\quad C_{Y_{\delta_a}} \cdot \delta_a + C_{Y_{\delta_r}} \cdot \delta_r + C_{Y_{\delta_{\alpha}}} \cdot \delta_r \alpha + C_{Y_\beta} \cdot \frac{\dot{\beta}b}{2V} \\
 C_{Z_a} &= C_{Z_0} + C_{Z_\alpha} \cdot \alpha + C_{Z_{\alpha^3}} \cdot \alpha^3 + C_{Z_q} \cdot \frac{q\bar{c}}{V} + C_{Z_{\delta_e}} \cdot \delta_e + \\
 &\quad C_{Z_{\delta_{\alpha\beta^2}}} \cdot \delta_e \cdot \beta^2 + C_{Z_{\delta_f}} \cdot \delta_f + C_{Z_{\delta_{\alpha\delta_f}}} \cdot \alpha \cdot \delta_f \\
 C_{l_a} &= C_{l_0} + C_{l_\beta} \cdot \beta + C_{l_p} \cdot \frac{pb}{2V} + C_{l_r} \cdot \frac{rb}{2V} + C_{l_{\delta_a}} \cdot \delta_a + \\
 &\quad C_{l_{\delta_r}} \cdot \delta_r + C_{l_{\delta_{\alpha}}} \cdot \delta_a \cdot \alpha
 \end{aligned}$$

$$\begin{aligned}
C_{m_a} &= C_{m_0} + C_{m_e} \cdot \alpha + C_{m_{e^2}} \cdot \alpha^2 + C_{m_q} \cdot \frac{q\bar{c}}{V} + C_{m_{\delta_e}} \cdot \delta_e + \\
&\quad C_{m_{\beta^2}} \cdot \beta^2 + C_{m_r} \cdot \frac{rb}{2V} + C_{m_{\delta_r}} \cdot \delta_r \\
C_{n_a} &= C_{n_0} + C_{n_p} \cdot \beta + C_{n_p} \cdot \frac{pb}{2V} + C_{n_r} \cdot \frac{rb}{2V} + C_{n_{\delta_a}} \cdot \delta_a + \\
&\quad C_{n_{\delta_r}} \cdot \delta_r + C_{n_q} \cdot \frac{q\bar{c}}{V} + C_{n_{\beta^3}} \cdot \beta^3. \tag{5.13}
\end{aligned}$$

The values of the coefficients of the variables in the Eqs (5.13) are summarized in Table 5. From this table it follows that this aerodynamic model includes effects like longitudinal-lateral crosscoupling and unsteady aerodynamics. For instance the gyroscopic effect of the propeller, for one nominal constant engine speed of 1800 r.p.m., is expressed in terms of the coefficients  $C_{m_p}$  ( $= -0.3118$ ) and  $C_{n_q}$  ( $= 0.1595$ ).

Figure 40 shows the dimensionless aerodynamic forces and moments for the symmetric and the asymmetric motions as a function of angle of attack  $\alpha$  and side-slip angle  $\beta$ , respectively. This figure also shows the effect of engine operation on these forces and moments. The Eqs (5.13) are solved in subroutine FAER 4, see Section 4.2 and Fig. 25.

### 5.2.2.2. The engine model

The contributions of the propeller/engine combination to the external forces and moments (5.12), in terms of dimensionless force and moment coefficients, become:

$$\begin{aligned}
C_{X_T} &= C_{X_{\Delta p_t}} \cdot \frac{\Delta p_t}{\frac{1}{2}\rho V^2} + C_{X_{\alpha \Delta p_t}} \cdot \alpha \left| \frac{\Delta p_t}{\frac{1}{2}\rho V^2} \right|^2 \\
C_{Y_T} &= 0 \\
C_{Z_T} &= C_{Z_{\Delta p_t}} \cdot \frac{\Delta p_t}{\frac{1}{2}\rho V^2} \\
C_{l_T} &= C_{l_{\alpha^2 \Delta p_t}} \cdot \alpha^2 \cdot \frac{\Delta p_t}{\frac{1}{2}\rho V^2} \\
C_{m_T} &= C_{m_{\Delta p_t}} \cdot \frac{\Delta p_t}{\frac{1}{2}\rho V^2} \\
C_{n_T} &= C_{n_{\Delta p_t}} \cdot \left| \frac{\Delta p_t}{\frac{1}{2}\rho V^2} \right|^3. \tag{5.14}
\end{aligned}$$

In the Eqs (5.14),  $\Delta p_t$  denotes the increase of total air pressure measured in the propeller slipstream. If the propeller is represented as an ideal pulling disc, the following relation between  $\Delta p_t / (\frac{1}{2}\rho V^2)$ , the airspeed  $V$  and the engine power  $P$  holds for the DHC-2 BEAVER:

$$\begin{aligned}
\frac{\Delta p_t}{\frac{1}{2}\rho V^2} &= a + b \frac{P}{\frac{1}{2}\rho V^3} \\
\text{with } \frac{P}{\frac{1}{2}\rho V^3} \text{ in } \left| \frac{\text{kW}}{\text{kg/sec}^3} \right|, \quad a = 0.08696 \quad \text{and} \quad b = 191.18. \tag{5.15}
\end{aligned}$$

In the case of piston engined airplanes, variations in airspeed  $V$  and engine power settings (engine speed  $n$  and manifold pressure  $p_z$ ) can be replaced by the variable  $\Delta p_t / \frac{1}{2}\rho V^2$ .<sup>(56)</sup> Engine power  $P$  as a function of the engine speed  $n$  in r.p.m., manifold pressure  $p_z$  in inch Hg and air density  $\rho$  ( $\text{kg/m}^3$ ) are obtained from the 'engine power chart', as given by the engine

TABLE 5. COEFFICIENTS IN THE NON-LINEAR AERODYNAMIC MODEL OF THE DHC-2 BEAVER, VALID WITHIN THE 35-55 m/sec TAS-RANGE (EQ. (5.13))

| $C_x$                   |          | $C_y$                   |           | $C_z$                    |           |
|-------------------------|----------|-------------------------|-----------|--------------------------|-----------|
| 0                       | -0.03554 | 0                       | -0.002226 | 0                        | -0.05504  |
| $\alpha$                | 0.00292  | $\beta$                 | -0.7678   | $\alpha$                 | -5.578    |
| $\alpha^2$              | 5.459    | $p$                     | -0.1240   | $\alpha^3$               | 3.442     |
| $\alpha^3$              | -5.162   | $r$                     | 0.3666    | $q$                      | -2.988    |
| $q$                     | -0.6748  | $\delta_a$              | -0.02956  | $\delta_e$               | -0.3980   |
| $\delta_r$              | 0.003412 | $\delta_t$              | 0.1158    | $\delta_e \cdot \beta^2$ | -15.93    |
| $\delta_f$              | -0.09447 | $\delta_r \cdot \alpha$ | 0.5238    | $\delta_t$               | -1.377    |
| $\alpha \cdot \delta_t$ | 1.106    | $\beta$                 | -0.1600   | $\alpha \cdot \delta_t$  | -1.261    |
| $C_l$                   |          | $C_m$                   |           | $C_n$                    |           |
| 0                       | 0.000591 | 0                       | 0.09448   | 0                        | -0.003117 |
| $\beta$                 | -0.06180 | $\alpha$                | -0.6029   | $\beta$                  | 0.006719  |
| $p$                     | -0.5045  | $\alpha^2$              | -2.140    | $p$                      | -0.1585   |
| $r$                     | 0.1695   | $q$                     | -15.56    | $r$                      | -0.1112   |
| $\delta_a$              | -0.09917 | $\delta_e$              | -1.921    | $\delta_a$               | -0.003872 |
| $\delta_r$              | 0.006934 | $\beta^2$               | 0.6921    | $\delta_r$               | -0.08256  |
| $\delta_f$              | -0.08269 | $r$                     | -0.3118   | $q$                      | 0.1595    |
| $\alpha \cdot \delta_a$ |          | $\delta_t$              | 0.4072    | $\beta^3$                | 0.1373    |

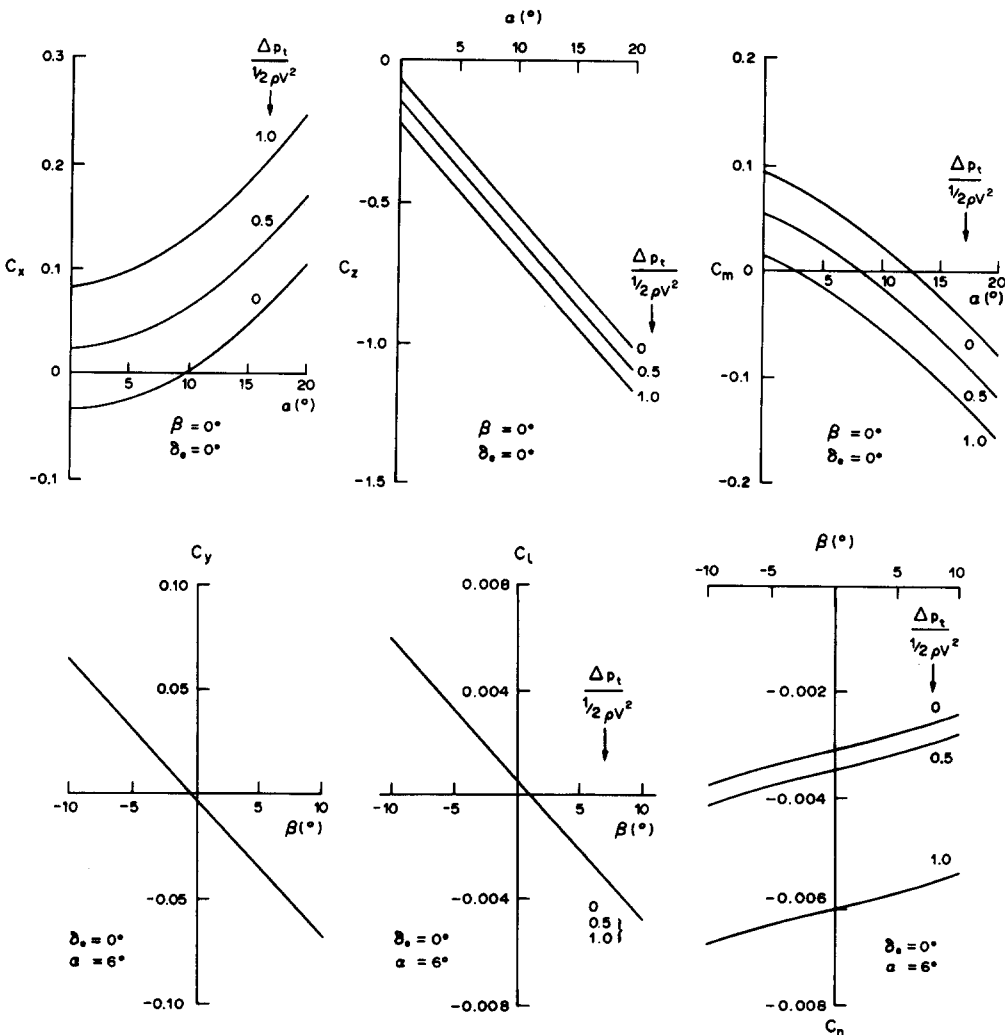


FIG. 40. The dimensionless aerodynamic forces and moments of the non-linear BEAVER-aircraft model as a function of angle of attack  $\alpha$  and side slip angle  $\beta$ .

TABLE 6. COEFFICIENTS IN THE NON-LINEAR ENGINE MODEL OF THE DHC-2 BEAVER, VALID WITHIN THE 35–55 m/sec TAS-RANGE (Eqs (5.14) AND (5.15))

| $C_x$                       | $C_z$    | $C_l$                                |
|-----------------------------|----------|--------------------------------------|
| $\Delta p_t$                | 0.1161   | $\Delta p_t$ -0.1563                 |
| $\alpha \cdot \Delta p_t^2$ | 0.1453   | $\alpha^2 \cdot \Delta p_t$ -0.01406 |
| $C_m$                       | $C_n$    |                                      |
| $\Delta p_t$                | -0.07895 | $\Delta p_t^3$ -0.003026             |
|                             |          | $a$ 0.08696                          |
|                             |          | $b$ 191.18                           |

manufacturer. In the present example, the equation for the engine power reads:

$$P = -326.5 + \left[ 0.00412(p_z + 7.4) \cdot (n + 2010) + (408 - 0.0965n) \cdot \left( 1 - \frac{\rho}{\rho_0} \right) \right] \quad (5.16)$$

(dimension of  $P$  in brake horse power)

(Multiplication of  $P$  by 0.7355 results in  $P$  in Nm/sec.)

The values of the coefficients in the engine equations (5.14) are summarized in Table 6. Figure 40 shows the effect of engine operation on the external force and moment coefficients for three values of  $\Delta p_t / \frac{1}{2} \rho V^2$ . Subroutine FENG4 solves the Eqs (5.14), see Section 4.2.

Figures 41, 42 and 43 show the response of this non-linear DHC-2 BEAVER Model on a blockshaped elevator ( $\delta_e$ ), aileron ( $\delta_a$ ) and rudder deflection ( $\delta_r$ ), respectively.

In Fig. 41 the responses of the angle of attack (ALFA) and pitch rate ( $Q$ ) clearly show the 'Short Period' motion of the BEAVER. The 'Phugoide' is visible in the responses of the true airspeed (TAS), the pitch angle (THETA), the flight path angle (GAMMA) and the rate of climb (C). The responses of the angle of roll (PHI) and the side-slip angle (BETA) clearly show the longitudinal-lateral crosscoupling included in the model.

In Fig. 42 the responses of the roll rate ( $P$ ) and roll angle (PHI) show the roll response of the BEAVER. The 'adverse Yaw', due to aileron deflection (DAIL), which is typical for the BEAVER, is clearly visible in the responses of the side-slip angle (BETA) and yaw angle (PSI).

The well-damped "Dutch Roll" oscillation of the BEAVER is clearly shown in the responses of the yaw rate ( $R$ ), the roll rate ( $P$ ) and the side-slip angle  $\beta$ , in Fig. 43.

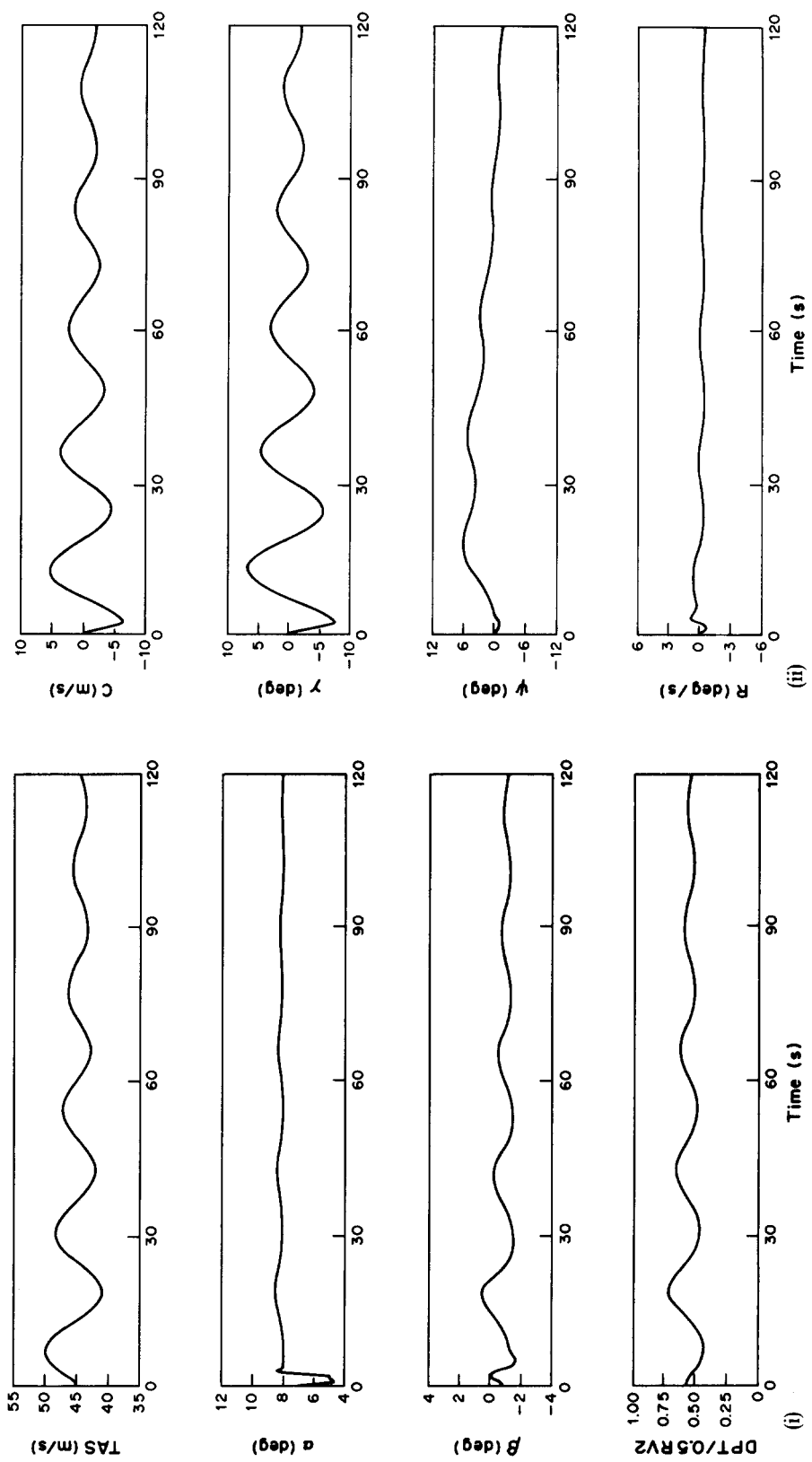
### 5.3. MATHEMATICAL MODELLING OF FLIGHT IN TURBULENCE AND WINDSHEAR

The application of turbulence and windshear in piloted flight simulation may be used for several purposes, e.g.:

- to serve as a general distracting element to increase the pilot's overall workload,
- to represent the actual disturbances acting on the aircraft in real flight, in order to investigate pilot-aircraft performance.

In the first application, simple filtering of Gaussian white noise is a possible solution, as the accuracy requirements on the simulated turbulence are rather low. However, as greater reliance is placed on the flight simulator, the accurate reproduction of turbulence and windshear becomes more important. Atmospheric turbulence is, in contrast with other elements of flight simulation like aircraft motion due to control inputs, not deterministic but stochastic by nature. So, the mathematical model, describing the turbulence velocity components, is based on statistical methods like power spectra and probability distributions.

Measurements of actual turbulence velocities have shown that atmospheric turbulence is a non-Gaussian process which poses a serious problem on its simulation. The so-called 'patchy' characteristics of atmospheric turbulence exhibit local regions of higher energy concentrations separated by relatively calm periods, which cause deviations from the



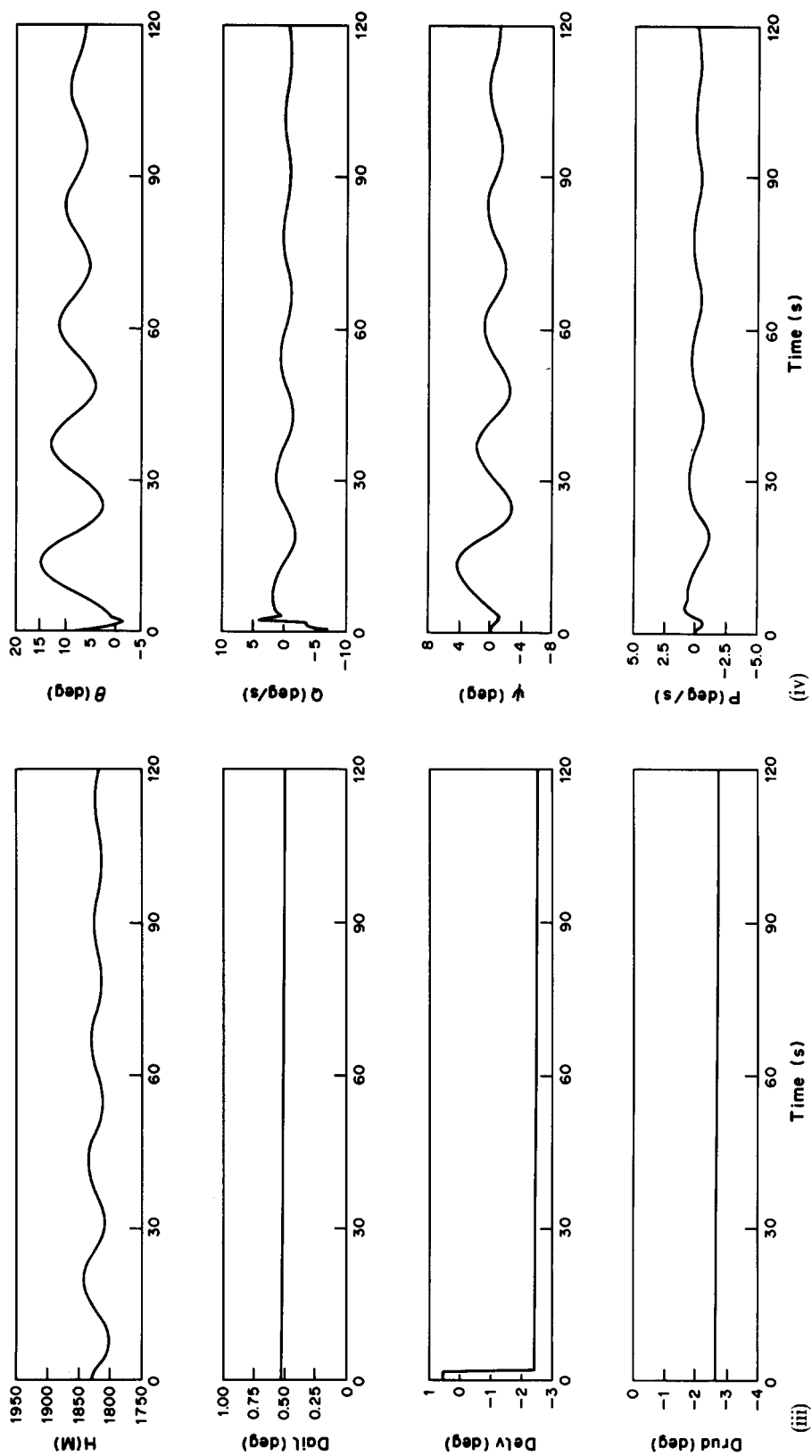
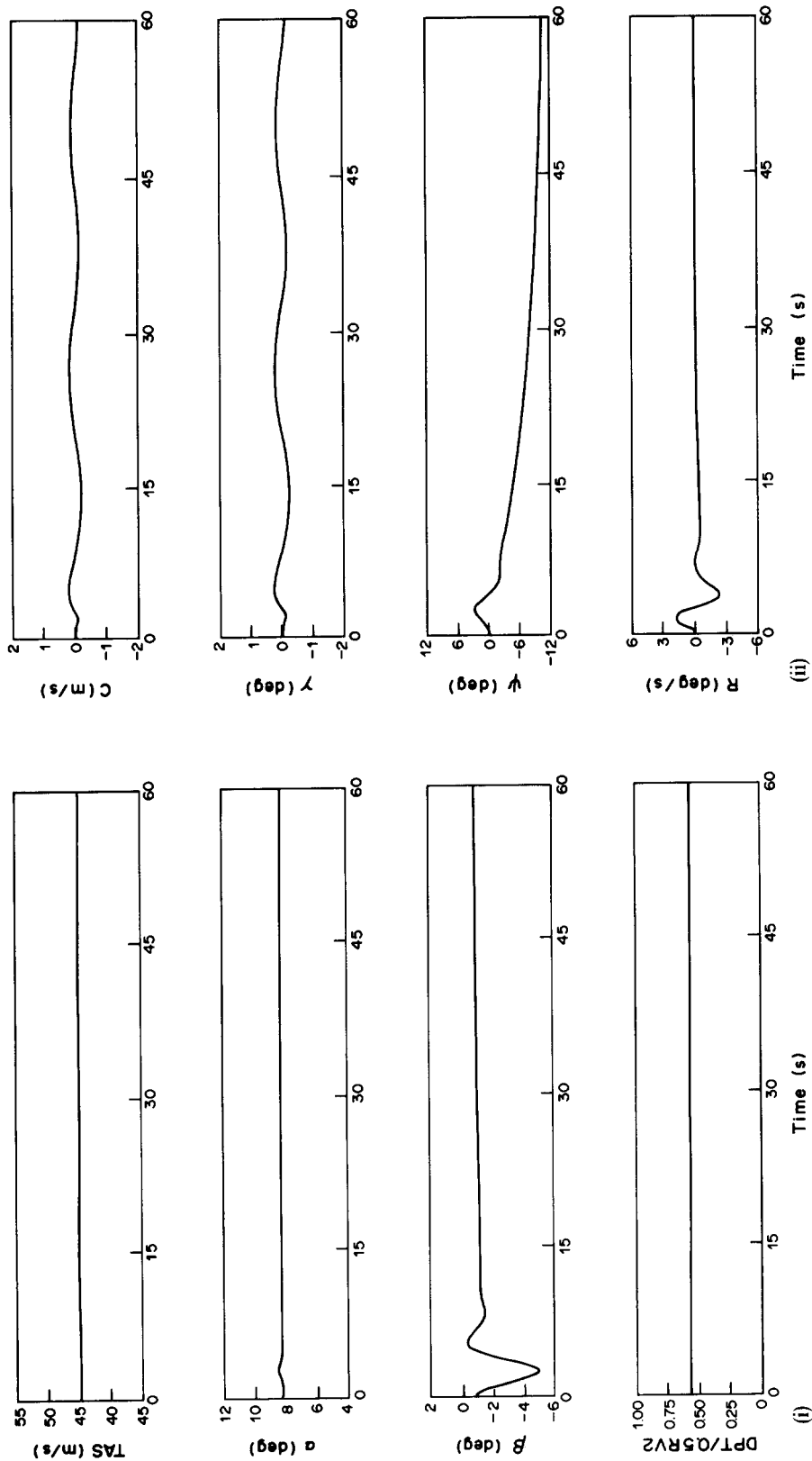


Fig. 41. The non-linear response of the DHC-2 BEAVER on a blockshaped elevator deflection ( $\delta_e = 3^\circ$ ), during 2 sec.



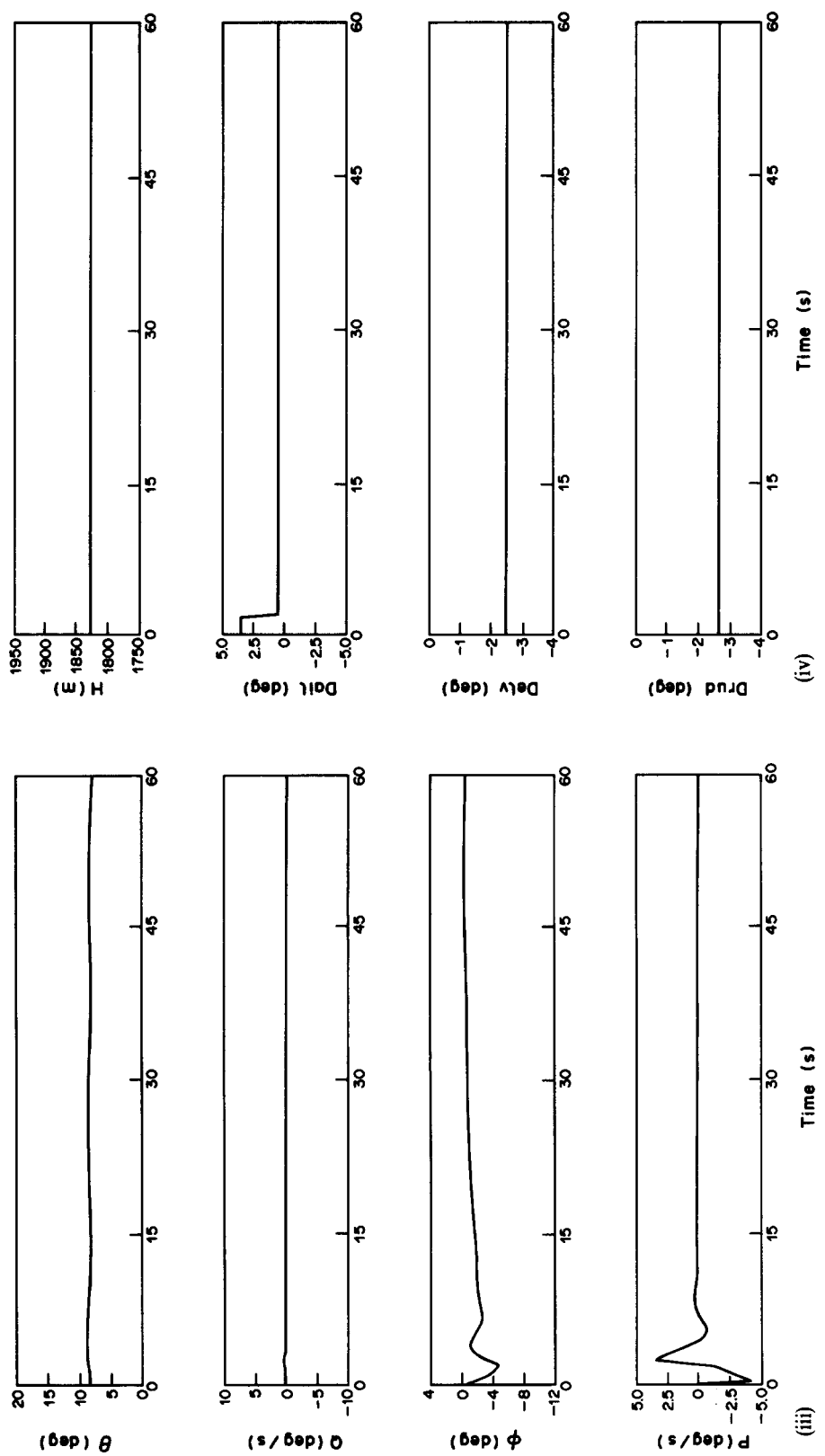
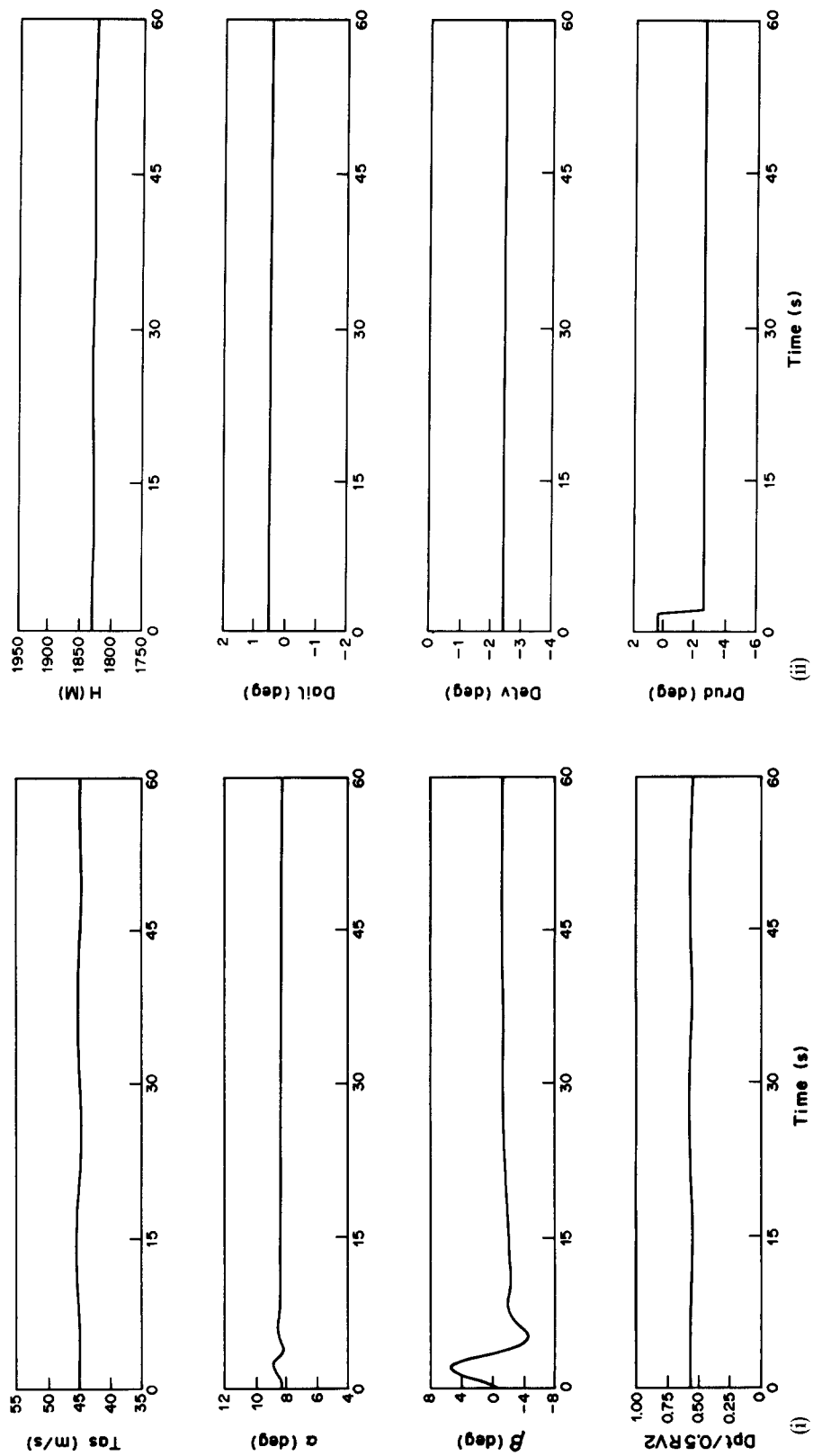


FIG. 42. The non-linear response of the DHC-2 BEAVER on a blockshaped aileron deflection ( $\delta_a = 3^\circ$ ), during 2 sec.



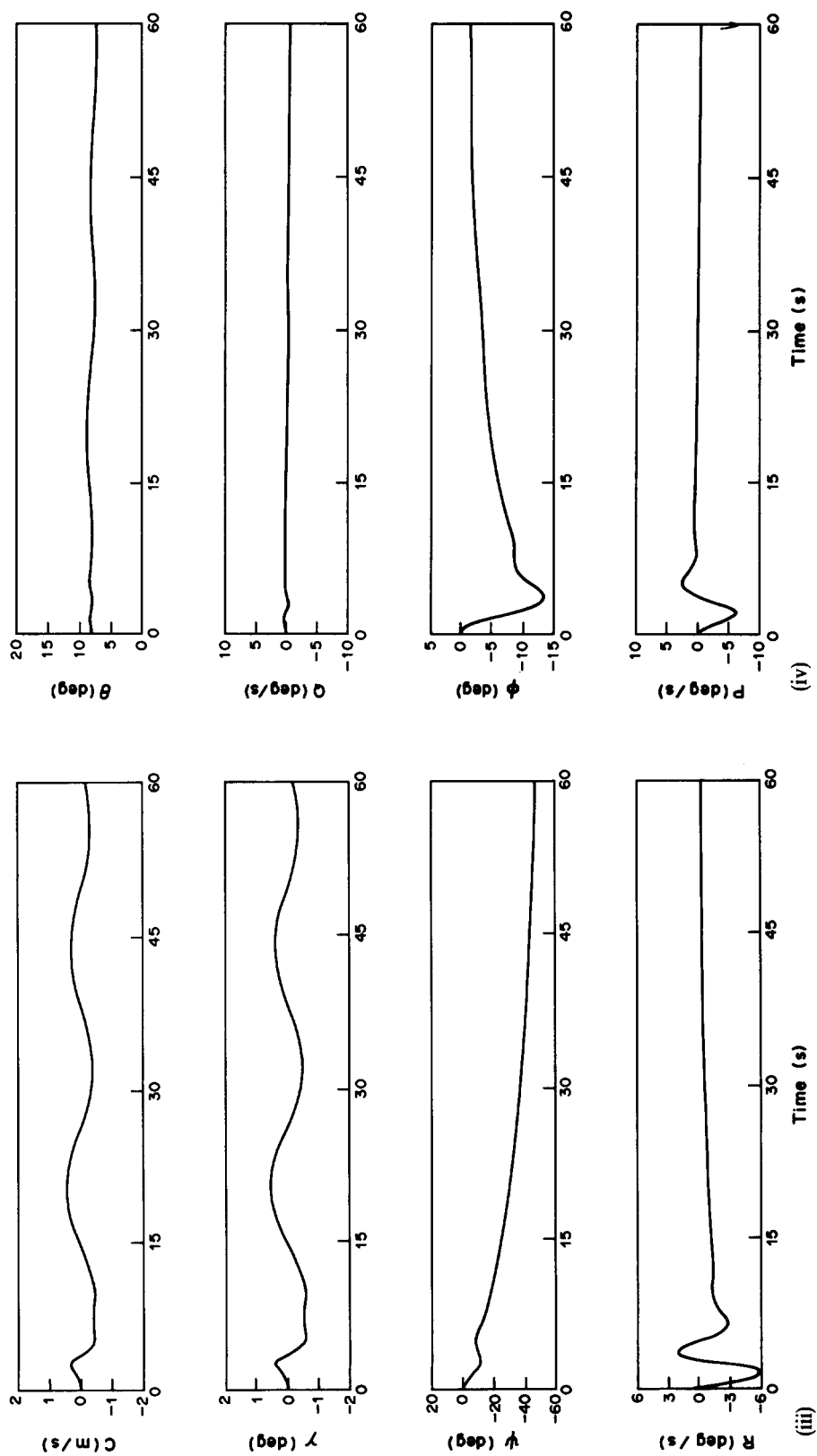


FIG. 43. The non-linear response of the DHC-2 BEAVER on a blockshaped rudder deflection ( $\delta_r = 3^\circ$ ), during 2 sec.

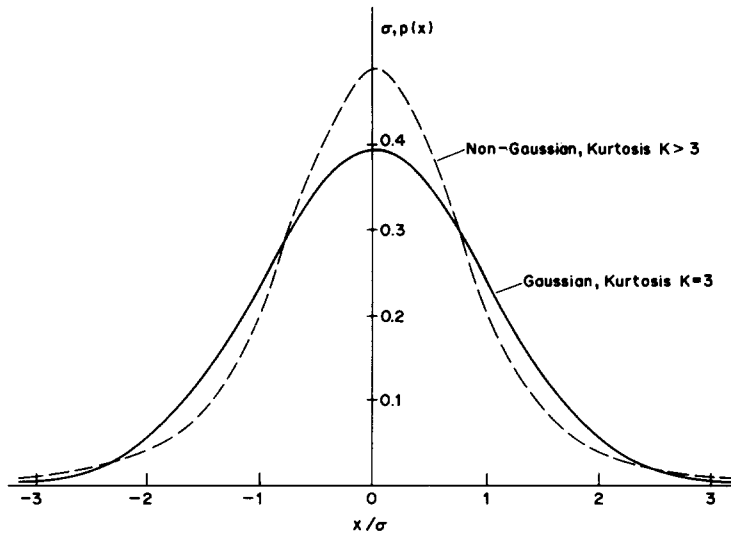


FIG. 44. The Gaussian—and a possible non-Gaussian—distribution function.

Gaussian distribution function. The non-Gaussian characteristics will be described in the following by two parameters: 'Kurtosis',  $K$ , and a 'patchiness parameter',  $R$ .

Figure 44 shows the Gaussian and a possible non-Gaussian distribution function which are distinguished by the value of the Kurtosis,  $K$ , defined as:<sup>(82)</sup>

$$K = \frac{m_4}{(m_2)^2}$$

where  $m_2$  is the second order central moment, known as the variance,  $\sigma^2$ , and  $m_4$  is the fourth order central moment, which takes the value of  $3\sigma^4$  (resulting in  $K = 3$ , see below) in a Gaussian process.

The second parameter, which describes the 'patchiness' in atmospheric turbulence, is the parameter ' $R$ ', to be defined below. The patchy characteristics may cause sudden large deviations in aircraft attitude, which demand pilot corrective actions. In particular in training and research simulation with the pilot-in-the-loop, patchy atmospheric turbulence is essential for pilot acceptance.

The complete patchy turbulence simulation is obtained, using five turbulence velocities as inputs to the mathematical model of the airplane (Fig. 45). The generation of each of these turbulence velocities consists of three independent white noise sources, feeding three linear filters, as shown in Fig. 46. The filter outputs  $a(t)$ ,  $b(t)$  and  $c(t)$  are mixed such as to obtain the desired patchy characteristic of the turbulence velocity. The longitudinal turbulence velocity  $u_{g_{sym}}$  and vertical velocity  $w_{g_{sym}}$  in Fig. 46 determine the symmetric airplane motions due to atmospheric turbulence.<sup>(76)</sup> The lateral turbulence velocity  $v_g$  and the turbulence velocities  $u_{g_{asym}}$  and  $w_{g_{asym}}$  in Fig. 46 determine the asymmetric airplane motions due to atmospheric turbulence.<sup>(77)</sup>

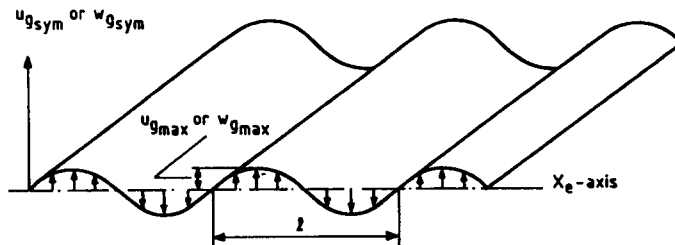


FIG. 45a. Sinusoidal elementary field of flow.  $u_{g_{sym}}$  and  $w_{g_{sym}}$  vary only along the  $X_e$ -axis, the wavelength in spanwise direction is assumed to be infinite.

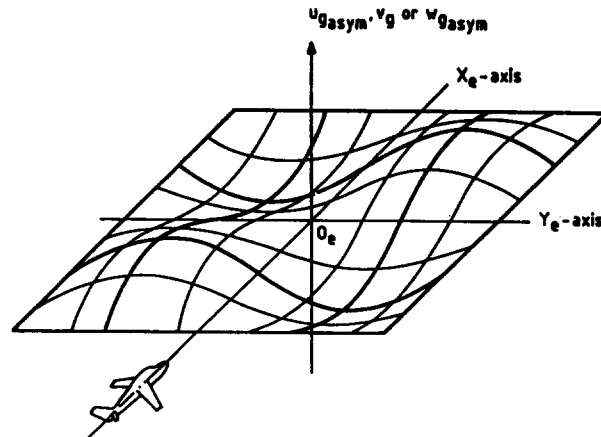


FIG. 45b. Two-dimensional elementary flowfield (Fig. 45a is a simplified case of this flowfield). The turbulence velocities  $u_{gasym}$ , and  $v_g$  and  $w_{gasym}$  change sinusoidally in the  $X_e$ —as well as in the  $Y_e$ —direction.

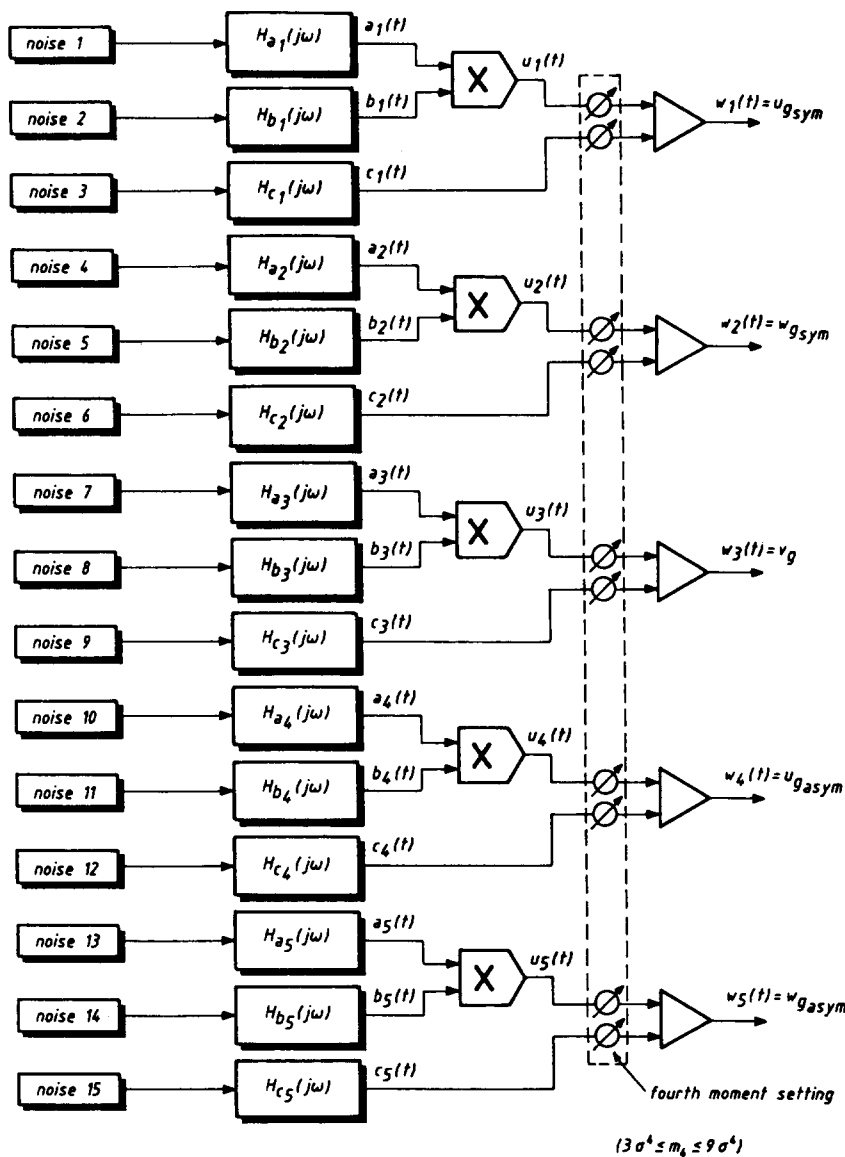


FIG. 46. The generation of 'Patchy' atmospheric turbulence for real-time flight simulation.

The actual generation of each of these five stochastic turbulence velocities employs the product of two independent Gaussian processes, shaped by linear filters to acquire the power spectra of the turbulence velocities, according to Dryden.<sup>(70)</sup> Turbulence velocities as a result of the multiplication, however, are more severely non-Gaussian than indicated by experimental data.<sup>(86, 87)</sup> Therefore, a third independent Gaussian process, linearly filtered also to obtain the Dryden power spectrum, is added to create a wide variety of possible patchy characteristics.<sup>(82)</sup>

The following describes the mathematical formulation for the generation of each of the five turbulence velocities.

(1) *The longitudinal turbulence velocity  $u_{g_{sym}}$*

The spectral equation for the longitudinal turbulence velocity, according to Dryden, reads:<sup>(76)</sup>

$$\Phi_{u_g u_g}(\omega) = \frac{2}{\pi} \sigma_{u_g}^2 \frac{L_{u_g}}{V} \frac{1}{1 + \omega^2 \left( \frac{L_{u_g}}{V} \right)^2}, \quad (5.17)$$

where  $\sigma_{u_g}^2$  is the variance of the longitudinal turbulence velocity and  $L_{u_g}$  is the scale length of this velocity. Figure 47 shows the standard deviation of the longitudinal turbulence velocity for different atmospheric conditions as a function of altitude. Figure 48 shows the scale length as a function of altitude for the same atmospheric conditions.<sup>(62)</sup> The auto-power spectral densities of the filter outputs  $a_1(t)$ ,  $b_1(t)$  and  $c_1(t)$  (Fig. 46) as derived in Ref. 82, read:

$$\Phi_{a_1 a_1}(\omega) = \frac{2}{\pi} \sigma_{a_1} \frac{L_{u_g}}{V} (R + 1) \frac{1}{1 + \left( \frac{L_{u_g}}{V} \right)^2 (R + 1)^2 \omega^2} \quad (5.18)$$

$$\Phi_{b_1 b_1}(\omega) = \frac{2}{\pi} \sigma_{b_1} \frac{L_{u_g}}{V} \frac{(R + 1)}{R} \frac{1}{1 + \left( \frac{L_{u_g}}{V} \right)^2 \left( \frac{R + 1}{R} \right)^2 \omega^2} \quad (5.19)$$

$$\Phi_{c_1 c_1}(\omega) = \frac{2}{\pi} \sigma_{c_1}^2 \frac{L_{u_g}}{V} \frac{1}{1 + \left( \frac{L_{u_g}}{V} \right)^2 \omega^2}. \quad (5.20)$$

The patchiness parameter  $R$  in Eqs (5.18) and (5.19) is defined as the ratio between the cutoff frequencies of the filters with transfer functions  $H_{a_1}(j\omega)$  and  $H_{b_1}(j\omega)$ ,<sup>(82)</sup> see below. Values applied for  $R$  in the simulation of patchy turbulence range from zero to one. With decreasing  $R$ , the average patch length increases. Figures 49 and 50 show the effect of the parameter  $R$  on the longitudinal turbulence velocity  $u_{g_{sym}}$ .

The filter transfer functions  $H_{a_1}(j\omega)$ ,  $H_{b_1}(j\omega)$  and  $H_{c_1}(j\omega)$  (Fig. 46) completely determine the shapes of the power spectral densities  $\Phi_{aa}(\omega)$ ,  $\Phi_{bb}(\omega)$  and  $\Phi_{cc}(\omega)$ , according to the following equations:<sup>(82)</sup>

$$\begin{aligned} \Phi_{aa}(\omega) &= |H_{a_1}(j\omega)|^2 \cdot \Phi_{00}(\omega)_1 \\ \Phi_{bb}(\omega) &= |H_{b_1}(j\omega)|^2 \cdot \Phi_{00}(\omega)_2 \\ \Phi_{cc}(\omega) &= |H_{c_1}(j\omega)|^2 \cdot \Phi_{00}(\omega)_3 \end{aligned} \quad (5.21)$$

where  $\Phi_{00}(\omega)_1$ ,  $\Phi_{00}(\omega)_2$  and  $\Phi_{00}(\omega)_3$  are the input auto-power spectra of independent Gaussian white noise signals, having the constant values of  $K_a^2$ ,  $K_b^2$  and  $K_c^2$  respectively.

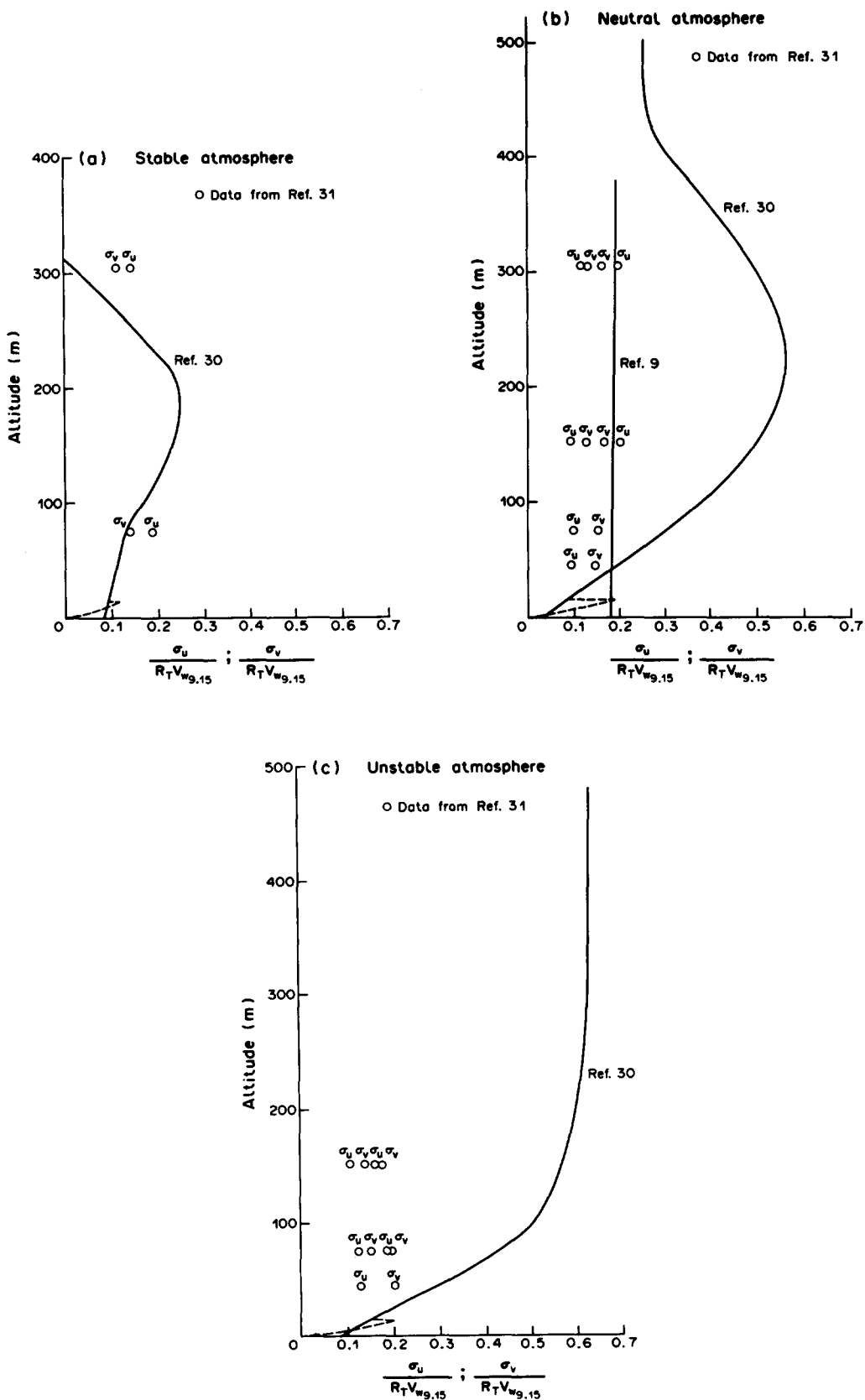


FIG. 47. Standard deviation of longitudinal and lateral turbulence velocities.<sup>(62)</sup>

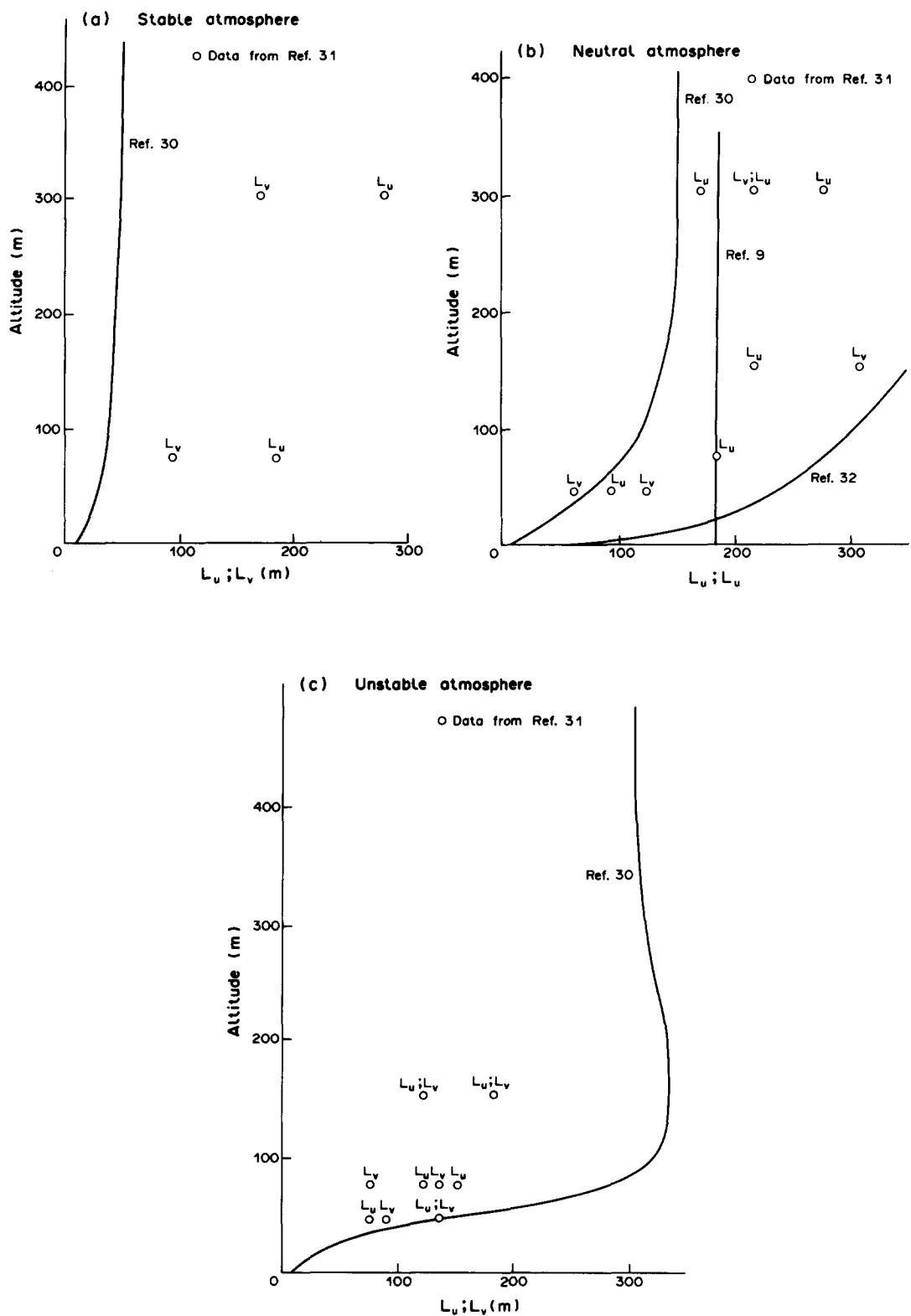
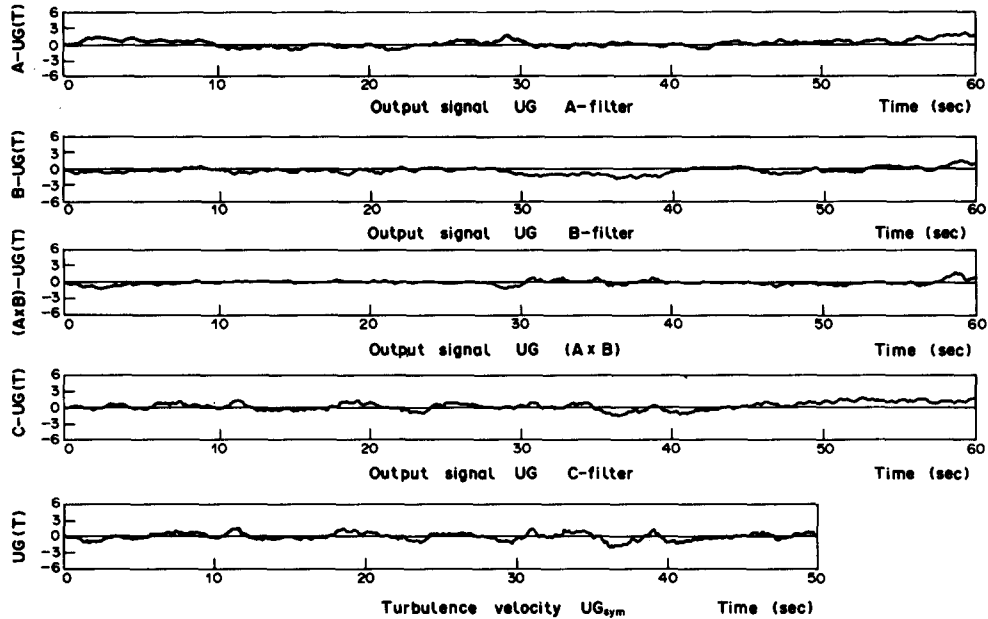


FIG. 48. Scale lengths of longitudinal and lateral turbulence velocities.<sup>[62]</sup>

FIG. 49. Composition of the longitudinal turbulence velocity  $u_{g_{sym}}$  for  $R = 1.0$  and  $Q = 1.0$ .

Substituting the expressions (5.18), (5.19) and (5.20) in (5.21) gives the expressions for the filter transfer functions:<sup>(82)</sup>

$$H_{a_1}(j\omega) = \frac{1}{K_a} \sqrt{\left[ \frac{2}{\pi} \sigma_{u_1} \frac{L_{u_g}}{V} (R + 1) \right]} \frac{1}{1 + \frac{L_{u_g}}{V} (R + 1) j\omega} \quad (5.22)$$

$$H_{b_1}(j\omega) = \frac{1}{K_b} \sqrt{\left[ \frac{2}{\pi} \sigma_{u_1} \frac{L_{u_g}}{V} \frac{(R + 1)}{R} \right]} \frac{1}{1 + \frac{L_{u_g}}{V} \frac{(R + 1)}{R} j\omega} \quad (5.23)$$

$$H_{c_1}(j\omega) = \frac{1}{K_c} \sigma_{c_1} \sqrt{\left[ \frac{2}{\pi} \frac{L_{u_g}}{V} \right]} \frac{1}{1 + \frac{L_{u_g}}{V} j\omega}. \quad (5.24)$$

In Eqs (5.22), (5.23) and (5.24) the following relations yield:

$$\begin{aligned} \sigma_{u_1} &= \sigma_{a_1} \sigma_{b_1}, \quad \text{where } \sigma_{a_1} = \sigma_{b_1} \\ \sigma_{u_g}^2 &= \sigma_{u_1}^2 + \sigma_{c_1}^2 = \sigma_{a_1}^2 \cdot \sigma_{b_1}^2 + \sigma_{c_1}^2. \end{aligned} \quad (5.25)$$

The parameter  $Q$  is defined as the ratio of the standard deviations of the processes  $u_1(t)$  and  $c_1(t)$  (Fig. 46):

$$Q = \frac{\sigma_{a_1} \sigma_{b_1}}{\sigma_{c_1}} = \frac{\sigma_{u_1}}{\sigma_{c_1}} \quad (5.26)$$

From Eqs (5.25), it follows for  $\sigma_{u_1}$  and  $\sigma_{c_1}$ :

$$\sigma_{u_1} = \frac{Q \cdot \sigma_{u_g}}{\sqrt{1 + Q^2}} \quad \text{and} \quad \sigma_{c_1} = \frac{\sigma_{u_g}}{\sqrt{1 + Q^2}}. \quad (5.27)$$

The Kurtosis  $K$  of the probability distribution of the turbulence velocity  $u_{g_{sym}}$  is completely determined by the parameter  $Q$ :

$$K = \frac{9Q^4 + 6Q^2 + 3}{(1 + Q^2)^2}, \quad (5.28)$$

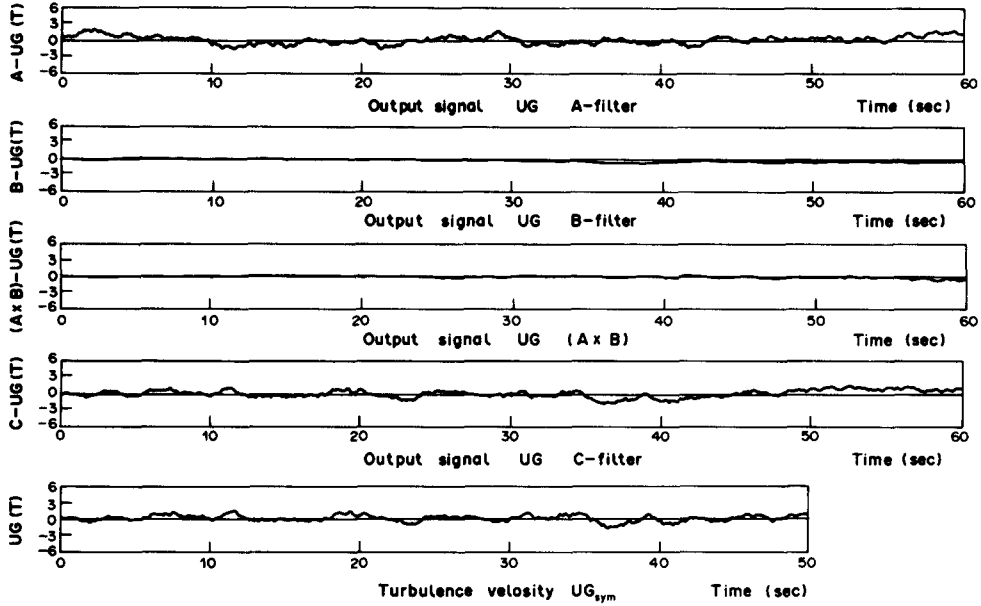


FIG. 50. Composition of the longitudinal turbulence velocity  $u_{g_{\text{sym}}}$  for  $R = 0.01$  and  $Q = 1.0$ .

where  $Q$  ranges from zero to infinity. The Gaussian probability distribution ( $K = 3$ ) is obtained for  $Q = 0$ . The modified Bessel distribution ( $K = 9$ ) results for  $Q = \infty$ .

## (2) The vertical turbulence velocity $w_{g_{\text{sym}}}$

The spectral equation for the vertical turbulence velocity, according to Dryden, reads:<sup>(76)</sup>

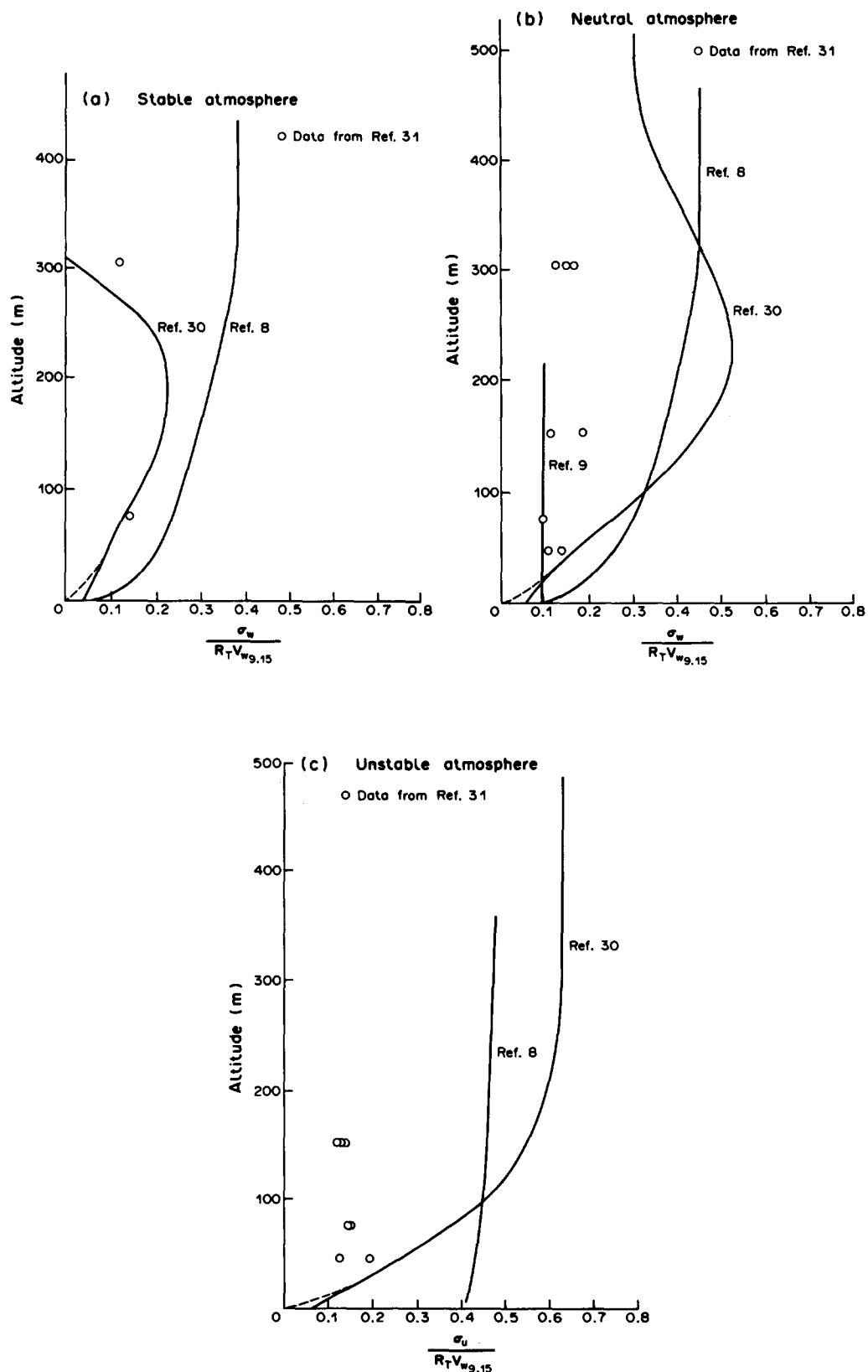
$$\Phi_{w_g w_g}(\omega) = \frac{1}{\pi} \sigma_{w_g}^2 \frac{L_{w_g}}{V} \frac{1 + 3\omega^2 \left( \frac{L_{w_g}}{V} \right)^2}{\left( 1 + \omega^2 \left[ \frac{L_{w_g}}{V} \right]^2 \right)^2}, \quad (5.29)$$

where  $\sigma_{w_g}^2$  and  $L_{w_g}$  are the variance and the scale length of the vertical turbulence velocity, respectively (Figs 51 and 52), which present the standard deviation and the scale length of the vertical turbulence velocity as a function altitude for different atmospheric conditions. The auto-power spectral densities of the filter outputs  $a_2(t)$ ,  $b_2(t)$  and  $c_2(t)$  (Fig. 46) as derived in Ref. 82, read:

$$\Phi_{a_2 a_2}(\omega) = \frac{2}{\pi} \sigma_{u_2} \frac{L_{w_g}}{V} \frac{(R+1)}{R} \frac{1}{1 + \left( \frac{L_{w_g}}{V} \right)^2 \left( \frac{R+1}{R} \right)^2 \omega^2} \quad (5.30)$$

$$\Phi_{b_2 b_2}(\omega) = \frac{1}{\pi} \sigma_{u_2} \frac{L_{w_g}}{V} (R+1) \frac{(1-R) + (3+R)(R+1)^2 \left( \frac{L_{w_g}}{V} \right)^2 \omega^2}{\left[ 1 + \left( \frac{L_{w_g}}{V} \right)^2 (R+1)^2 \omega^2 \right]^2} \quad (5.31)$$

$$\Phi_{c_2 c_2}(\omega) = \frac{1}{\pi} \sigma_{c_2}^2 \frac{L_{w_g}}{V} \frac{1 + 3 \left( \frac{L_{w_g}}{V} \right)^2 \omega^2}{\left[ 1 + \left( \frac{L_{w_g}}{V} \right)^2 \omega^2 \right]^2}. \quad (5.32)$$

FIG. 51. Standard deviation of vertical turbulence velocity.<sup>(62)</sup>

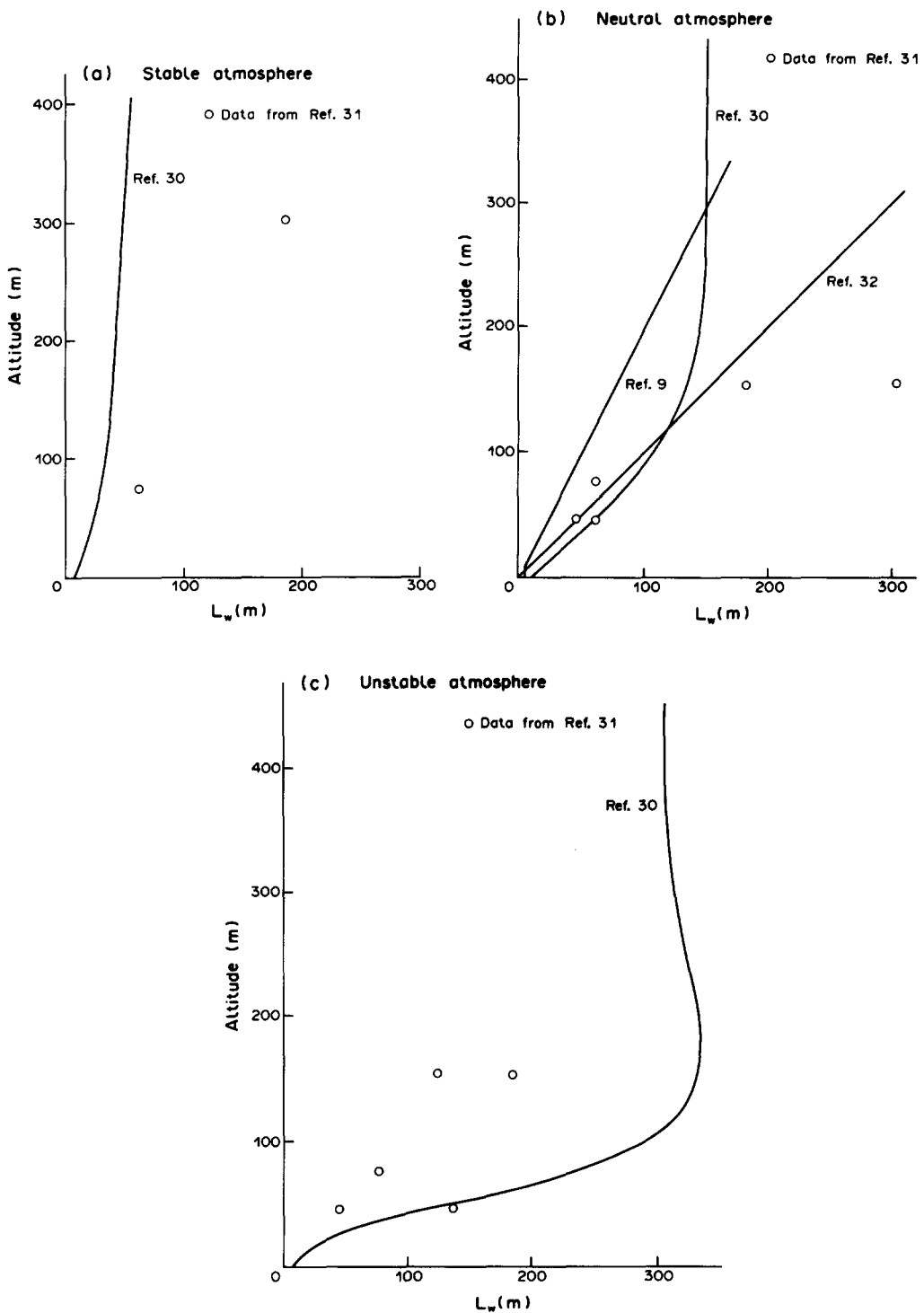


FIG. 52. Scale length of vertical turbulence velocity.<sup>(62)</sup>

Substituting the expressions (5.30), (5.31) and (5.32) in the equations (5.21) results in the expressions for the filter transfer functions:

$$H_{a_2}(j\omega) = \frac{1}{K_a} \sqrt{\left[ \frac{2}{\pi} \sigma_{u_2} \frac{L_{w_2}(R+1)}{V} \frac{1}{R} \right]} \frac{1}{1 + \frac{(R+1)L_{w_2}}{V} j\omega} \quad (5.33)$$

$$H_{b_2}(j\omega) = \frac{1}{K_b} \sqrt{\left[ \frac{1}{\pi} \sigma_{u_2} \frac{L_{w_g}}{V} (R+1) \right]} \frac{\sqrt{(1-R)+(R+1)\sqrt{(3+R)}} \frac{L_{w_g} j\omega}{V}}{\left[ 1 + (R+1) \frac{L_{w_g} j\omega}{V} \right]^2} \quad (5.34)$$

$$H_{c_2}(j\omega) = \frac{1}{K_c} \sigma_{c_2} \sqrt{\left[ \frac{1}{\pi} \frac{L_{w_g}}{V} \right]} \frac{1 + \sqrt{3} \frac{L_{w_g} j\omega}{V}}{\left( 1 + \frac{L_{w_g} j\omega}{V} \right)^2}. \quad (5.35)$$

The values of  $\sigma_{u_2}$  and  $\sigma_{c_2}$  follow from Eq. (5.27). However, in this equation  $\sigma_{u_g}$  should now be replaced by  $\sigma_{v_g}$ .

### (3) The lateral turbulence velocity $v_g$

The spectral equation for the lateral turbulence velocity, according to Dryden, is identical to the spectral equation for the vertical turbulence velocity  $w_{g_{sym}}$ .<sup>(77)</sup> So, the derivation of the auto-power spectral densities of the filter outputs  $a_3(t)$ ,  $b_3(t)$  and  $c_3(t)$  (Fig. 46) are identical to the expressions (5.30), (5.31) and (5.32), provided that the index  $w_g$  is replaced by  $v_g$  and the subscript 2 by 3. Summarizing the expressions for the filter transfer functions for the generation of the lateral turbulence velocity:

$$H_{a_3}(j\omega) = \frac{1}{K_a} \sqrt{\left[ \frac{2}{\pi} \sigma_{u_3} \frac{L_{v_g}}{V} \frac{(R+1)}{R} \right]} \frac{1}{1 + \frac{(R+1)}{R} \frac{L_{v_g}}{V} j\omega} \quad (5.36)$$

$$H_{b_3}(j\omega) = \frac{1}{K_b} \sqrt{\left[ \frac{1}{\pi} \sigma_{u_3} \frac{L_{v_g}}{V} (R+1) \right]} \frac{\sqrt{(1-R)+(R+1)\sqrt{(3+R)}} \frac{L_{v_g} j\omega}{V}}{\left[ 1 + (R+1) \frac{L_{v_g} j\omega}{V} \right]^2} \quad (5.37)$$

$$H_{c_3}(j\omega) = \frac{1}{K_c} \sigma_{c_3} \sqrt{\left[ \frac{1}{\pi} \frac{L_{w_g}}{V} \right]} \frac{1 + \sqrt{3} \frac{L_{v_g} j\omega}{V}}{\left( 1 + \frac{L_{v_g} j\omega}{V} \right)^2}. \quad (5.38)$$

The values of  $\sigma_{u_3}$  and  $\sigma_{c_3}$  again follow from Eq. (5.27). However, in this case  $\sigma_{u_g}$  is replaced by  $\sigma_{v_g}$ .

### (4) The longitudinal turbulence velocity $\hat{u}_{g_{asym}}$ , where $\hat{u}_g = \frac{u_g}{V}$

The expression for the effective one-dimensional power spectral density function of the longitudinal turbulence velocity  $\hat{u}_{g_{asym}}$ , as derived in Ref. 77 reads:

$$I_{\hat{u}_g}(\Omega_x L_g, B) = \frac{\hat{u}_g^2}{\pi} \int_0^\infty h^2\left(\Omega_y \frac{b}{2}\right) \frac{1 + \Omega_x^2 L_g^2 + 4\Omega_y^2 L_g^2}{\left(1 + \Omega_x^2 L_g^2 + \Omega_y^2 L_g^2\right)^{5/2}} d(\Omega_y L_g). \quad (5.39)$$

This function is approximated by the following general expression:<sup>(77)</sup>

$$I_{\hat{u}_g}(\Omega_x L_g, B) = I_{\hat{u}_g}(O, B) \frac{1 + \tau_3^2 \Omega_x^2 L_g^2}{(1 + \tau_1^2 \Omega_x^2 L_g^2)(1 + \tau_2^2 \Omega_x^2 L_g^2)}, \quad (5.40)$$

where  $B = b/2L_g$  and  $L_g = L_{u_g}$ .

$I_{\hat{u}_g}(O, B)$  is presented as a function of  $B$  in Fig. 53, and Fig. 54 presents  $\tau_1$ ,  $\tau_2$  and  $\tau_3$  as functions of  $B$ . Table 7 presents the numerical values of these variables.

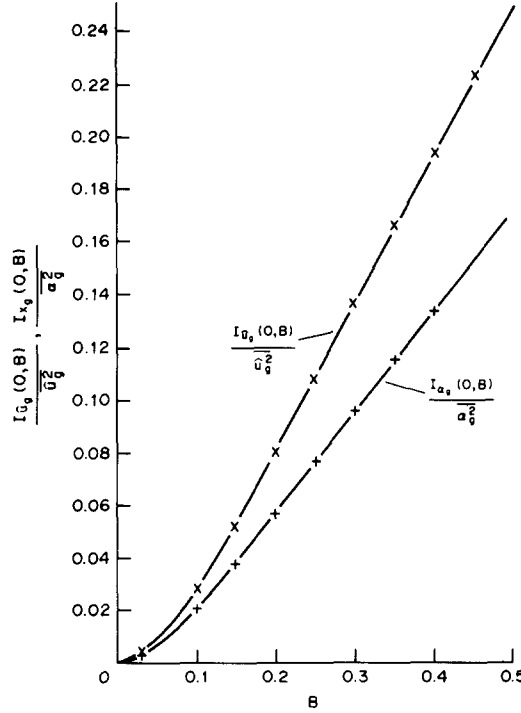


FIG. 53.  $\frac{I_{\bar{u}_g}(O, B)}{\bar{u}_g^2}$  and  $\frac{I_{a_4}(O, B)}{\bar{\alpha}_g^2}$  as functions of  $B$ .

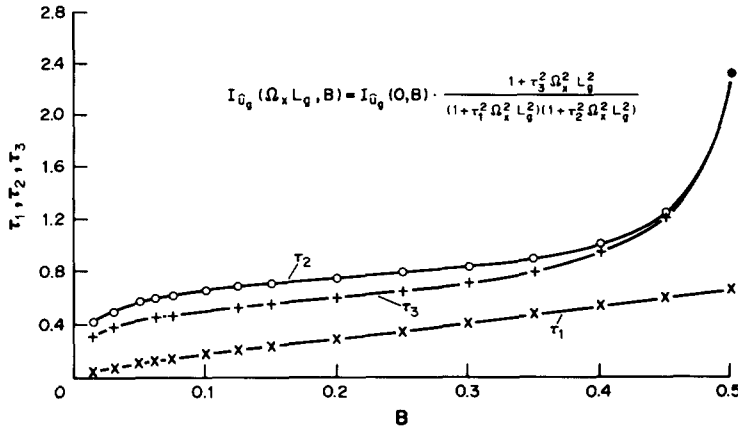


FIG. 54.  $\tau_1$ ,  $\tau_2$  and  $\tau_3$  in the approximated power spectral density function of the horizontal gust velocity, as functions of  $B$ .

Using the same method as for the derivation of the filter transfer functions for  $u_{g_{\text{sym}}}$  and  $w_{g_{\text{sym}}}$ , the filter transfer functions for the generation of  $\dot{u}_{g_{\text{asym}}}$  read<sup>(83)</sup> (Fig. 46):

$$H_{a_4}(j\omega) = \frac{1}{K_a} \sqrt{C} \frac{1}{1 + A \cdot j\omega} \quad (5.41)$$

$$H_{b_4}(j\omega) = \frac{1}{K_b} \sqrt{F} \frac{B + E \cdot j\omega}{(1 + D \cdot j\omega)(1 + G \cdot j\omega)} \quad (5.42)$$

$$H_{c_4}(j\omega) = \frac{1}{K_c} \sqrt{H} \frac{1 + L \cdot j\omega}{(1 + M \cdot j\omega)(1 + N \cdot j\omega)}. \quad (5.43)$$



This function is, like  $I_{\hat{u}_g}(\Omega_x L_g, B)$ , approximated by the following expression:<sup>(77)</sup>

$$I_{\alpha_g}(\Omega_x L_g, B) = I_{\alpha_g}(O, B) \frac{1 + \tau_6^2 \Omega_x^2 L_g^2}{(1 + \tau_4^2 \Omega_x^2 L_g^2)(1 + \tau_5^2 \Omega_x^2 L_g^2)}, \quad (5.45)$$

where  $L_g = L_{w_g}$ . The expression  $I_{\alpha_g}(O, B)$  is presented as a function of  $B$  in Fig. 53, and Fig. 55 presents  $\tau_4$ ,  $\tau_5$  and  $\tau_6$  as functions of  $B$ . Table 8 presents the numerical values of these variables.

The expressions (5.41), (5.42) and (5.43) also apply to the filter transfer functions  $H_{a_5}(j\omega)$ ,  $H_{b_5}(j\omega)$  and  $H_{c_5}(j\omega)$  of the vertical turbulence velocity  $\alpha_{g_{asy}}$  (Fig. 46), except that in the constants  $A$  up to and including  $N$  in these transfer functions:

$I_{\hat{u}_g}(O, B)$  should be replaced by  $I_{\alpha_g}(O, B)$ ;

$L_{w_g}$  should be replaced by  $L_{w_g}$ ;

$\tau_1$  should be replaced by  $\tau_4$ ;

$\tau_2$  should be replaced by  $\tau_5$ ;

$\tau_3$  should be replaced by  $\tau_6$ .

The patchy turbulence simulation described above, runs in real-time on the Gould SEL 32/87 in combination with the modular flight simulation software, described in Section 5.2.2.

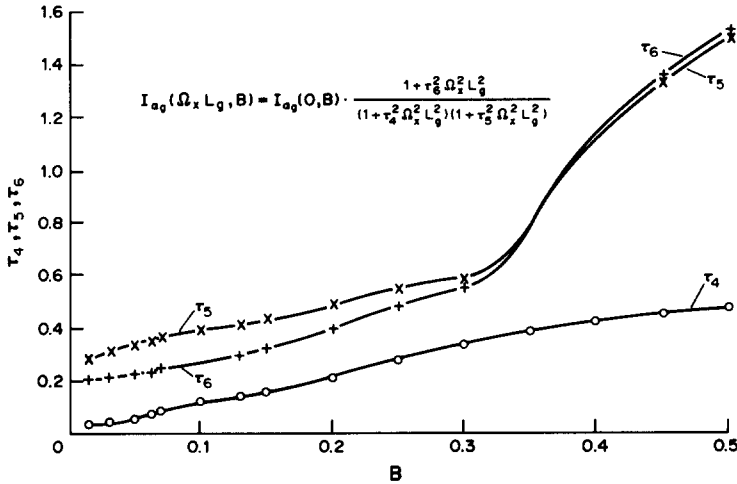


FIG. 55.  $\tau_4$ ,  $\tau_5$  and  $\tau_6$  in the approximated power spectral density function of the vertical gust velocity as functions of  $B$ .

TABLE 8.  $\frac{I_{x_g}(O, B)}{\alpha_g^2}$ ,  $\tau_4$ ,  $\tau_5$  AND  $\tau_6$  AS FUNCTIONS OF  $B$

| $B$      | $\frac{I_{x_g}(O, B)}{\alpha_g^2}$ | $\tau_4$ | $\tau_5$ | $\tau_6$ |
|----------|------------------------------------|----------|----------|----------|
| 0.50     | 0.171258                           | 0.480764 | 1.492572 | 1.527124 |
| 0.45     | 0.154164                           | 0.458294 | 1.332911 | 1.358464 |
| 0.40     | 0.136015                           | 0.426746 | 1.120000 | 1.140000 |
| 0.35     | 0.116959                           | 0.386097 | 0.787000 | 0.773000 |
| 0.30     | 0.097219                           | 0.337007 | 0.589747 | 0.552325 |
| 0.25     | 0.077119                           | 0.279943 | 0.551119 | 0.482539 |
| 0.20     | 0.057131                           | 0.218703 | 0.488882 | 0.390730 |
| 0.15     | 0.037945                           | 0.162684 | 0.440944 | 0.324153 |
| 0.125    | 0.028958                           | 0.136627 | 0.417279 | 0.296144 |
| 0.10     | 0.020599                           | 0.111941 | 0.392720 | 0.271229 |
| 0.075    | 0.013101                           | 0.087681 | 0.365723 | 0.247885 |
| 0.0625   | 0.009769                           | 0.076006 | 0.351389 | 0.237504 |
| 0.05     | 0.006779                           | 0.064521 | 0.336211 | 0.227862 |
| 0.03125  | 0.003084                           | 0.047613 | 0.310788 | 0.214478 |
| 0.015625 | 0.000932                           | 0.033226 | 0.283501 | 0.202983 |

### 5.3.1. Coupling of the Patchy Turbulence Simulation and the Mathematical Model of the Airplane

The coupling of the patchy turbulence simulation with the aircraft mathematical model, to compute the dimensionless force and moment coefficients due to atmospheric turbulence, has been derived in Ref. 76 for the symmetric and in Ref. 77 for the asymmetric airplane motions. As a result, the expressions for the force and moment coefficients in the Eqs (5.12), due to atmospheric turbulence, in case of a linear aircraft model as described in Section 5.2.1, read:

$$\begin{aligned}
 C_{X_g} &= C_{X_u} \cdot \hat{u}_{g\text{sym}} & + C_{X_a} \cdot \alpha_{g\text{sym}} \\
 C_{Y_g} &= & C_{Y_p} \cdot \beta_g \\
 C_{Z_g} &= C_{Z_u} \cdot \hat{u}_{g\text{sym}} & + C_{Z_a} \cdot \alpha_{g\text{sym}} \\
 C_{l_g} &= -C_{l_w} \cdot \hat{u}_{g\text{asym}} + C_{l_p} \cdot \beta_g & + C_{l_a} \cdot \alpha_{g\text{asym}} \\
 C_{m_g} &= C_{m_u} \cdot \hat{u}_{g\text{sym}} + C_{m_{u_p}} \cdot \frac{\dot{\hat{u}}_g \bar{c}}{V} & + C_{m_a} \cdot \alpha_{g\text{sym}} + C_{m_{a_p}} \cdot \frac{\dot{\alpha}_g \bar{c}}{V} \\
 C_{n_g} &= -C_{n_w} \cdot \hat{u}_{g\text{asym}} + C_{n_p} \cdot \beta_g & + C_{n_a} \cdot \alpha_{g\text{asym}}.
 \end{aligned} \tag{5.46}$$

In the Eqs (5.46),  $C_{m_{u_p}}$  and  $C_{m_{a_p}}$  are:<sup>(76)</sup>

$$\begin{aligned}
 C_{m_{u_p}} &= -2C_{m_h} \cdot \frac{l_h}{\bar{c}} \quad (\text{where } C_{m_h} \text{ is the contribution to } C_m \text{ due to the horizontal tail}) \\
 C_{m_{a_p}} &= C_{m_a} - C_{m_q}.
 \end{aligned}$$

In the case of a non-linear mathematical model of the airplane, covering the complete flight envelope, the coupling of the patchy turbulence model is more complex, as the stability derivatives in the Eqs (5.46) are no longer constants.

### 5.3.2. Wind Shear and Wind Profiles

During an actual approach to landing of an airplane there is usually some wind in the lower atmosphere. Of major importance to the pilot is the variation with altitude of the wind velocity and direction, known as the wind shear, as experienced by the airplane.

The combined effect of two atmospheric disturbance components represents the total wind shear (Fig. 56):

- (1) The variation of the mean or steady-state wind velocity with altitude, as determined from the wind profile and the change in wind direction with altitude.
- (2) A stochastic component, which is the result of the prevailing patchy atmospheric turbulence as described above.

Experimental data indicate that the atmospheric stability influences wind profiles, and large wind shears are known to occur, especially if the atmosphere is very stable. Since the mathematical model of the steady-state wind variation with altitude presented below is a function of the atmospheric stability, this parameter is discussed first.

The rate of change of air temperature with altitude,  $dT/dh$ , is one of the major factors affecting atmospheric stability. Excluding temperature inversions, the air temperature decreases with increasing altitude. So, the so-called lapse rate,  $dT/dh$ , is normally negative. Atmospheric stability characteristics are usually given for three atmospheric conditions:

- (1) Stable:  $-dT/dh < 0.005^\circ\text{C}/\text{m}$
- (2) Neutral:  $0.005 \leq -dT/dh \leq 0.01^\circ\text{C}/\text{m}$
- (3) Unstable:  $-dT/dh > 0.01^\circ\text{C}/\text{m}$ .

Both the wind profile model and values of some parameters defining the turbulence model, presented earlier in this section, depend on the atmospheric stability (see Figs 47, 48, 51 and 52).

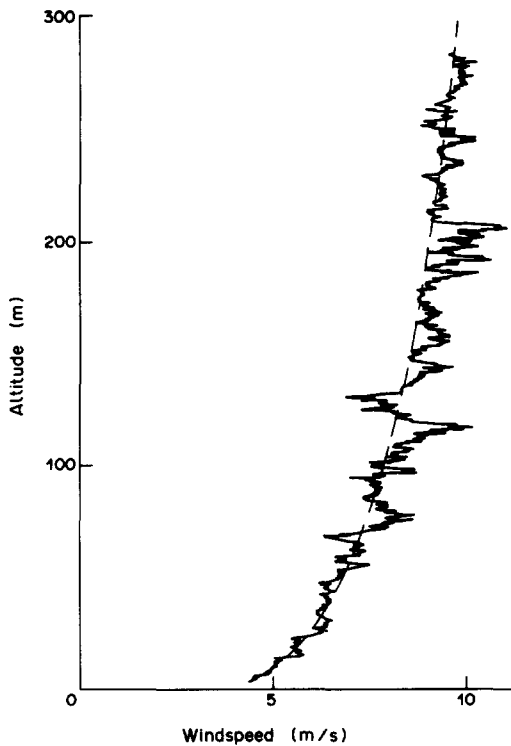


FIG. 56. Superposition of the wind profile and turbulence.

Assuming that the mean or steady-state wind velocity has no vertical component at low altitude, the horizontal wind velocity vector  $V_w$  is defined by its magnitude  $V_w$  and its direction  $\psi_w$ , both of which can vary with altitude. The change of wind direction with increasing altitude over coastal planes in the northern hemisphere is normally clockwise. On the average it amounts to  $0.04^\circ/\text{m}$  up to an altitude of 900 m.<sup>(63)</sup> Actual variations in wind direction may be much larger than  $0.04^\circ/\text{m}$  in the so-called shear conditions, due to factors such as a locally irregular temperature profile, occurring in particular in very stable air.<sup>(81)</sup>

The wind velocity vector magnitude, or wind speed, is modelled by expressions matched to experimental data. In unstable atmospheric conditions a logarithmic law seems to fit the experimental data quite well. Employing the notation as given in Refs 79 and 80, for standard atmospheric stability conditions and flat terrain:

$$u(z) = \frac{u^*}{k} \cdot \ln\left(\frac{z}{z_0}\right) \quad (5.47)$$

where

$u(z)$  = wind speed at height  $z$ ,

$u^*$  = friction velocity = 0.47 m/sec, being constant up to a height,  $z$ , of at least 100 m,

$k$  = Von Karman constant = 0.4,

$z_0$  = aerodynamic roughness height = 0.1 m.

In order to bring the wind shear and turbulence models to a common basis, the wind speed is expressed as a function of the wind velocity at a reference height of 9.15 m (30 ft). The following expression for the wind speed  $V_w$  can be found from Eq. (5.47), using a different notation:<sup>(64)</sup>

$$V_w = V_{w_{9.15}} (0.43 \log_{10} h + 0.572) \quad 0 < h < 300 \text{ m}$$

$$V_w = 1.637 \cdot V_{w_{9.15}} \quad h \geq 300 \text{ m}$$

where

$V_w$  = wind speed at height  $h$  (m/sec),

$V_{w_{9.15}}$  = wind speed at 9.15 m altitude (m/sec),

$h$  = altitude above the terrain (m).

The shape of the wind profile depends more critically on the lapse rate in neutral and stable atmospheric conditions. In these cases the wind profile can be represented by a power law:<sup>(80)</sup>

$$V_w = V_{w_{9.15}} \cdot \frac{h^p - h_0^p}{9.15^p - h_0^p} \quad 0 < h < 300 \text{ m}$$

$$V_w = V_{w_{300}} \quad h \geq 300 \text{ m}$$

where

$h_0 = 0.03 \text{ m}$ ,

$p = 0.43 + 27 \text{ d}T/\text{dh}$ ,

$V_{w_{300}}$  = wind speed at 300 m altitude (m/sec).

Figure 57 shows the wind profiles, according to the above expressions, for  $-\text{d}T/\text{dh} > 0.01$ ,  $-\text{d}T/\text{dh} = 0.0065$  and  $-\text{d}T/\text{dh} = 0.003$ , representing unstable, neutral and stable atmospheric conditions, respectively.

A cumulative probability of reported mean wind and cross wind at the reference height of 9.15 m is shown in Fig. 58.<sup>(64)</sup> The data presented in this figure may provide an estimate of the mean wind speed at 9.15 m altitude required to utilize the curves in Figs 47, 51 and 57 in order to generate patchy atmospheric turbulence and windshear.

Other meteorological phenomena causing dangerous windshears to aircraft are the thunderstorm and the microburst. Windshear profiles occurring during a thunderstorm are measured and modelled<sup>(73)</sup> for use in flight training simulation. Examples are the windshear profiles, which occurred during the Logan/Iberian, 1973, accident and the Kennedy/Eastern, 1975, accident.

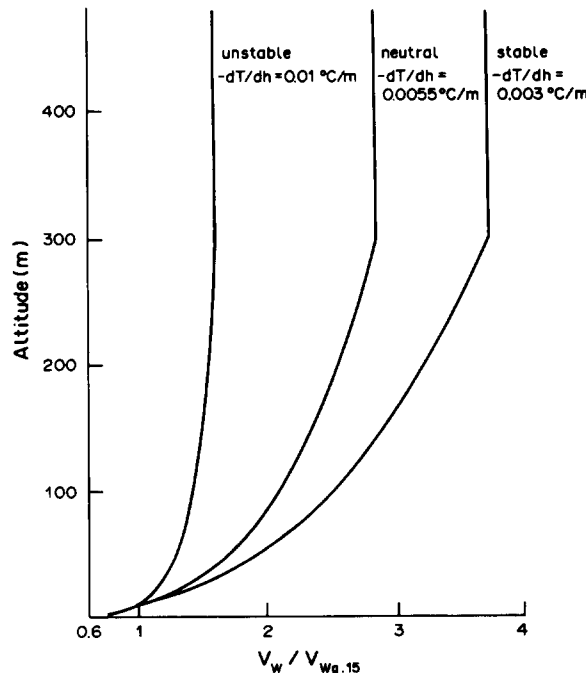


FIG. 57. Wind profiles for three atmospheric stability conditions.

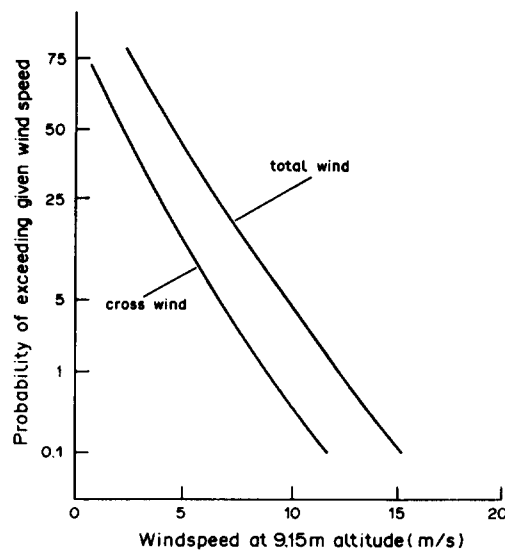


FIG. 58. Cumulative probability of reported mean wind and cross wind.

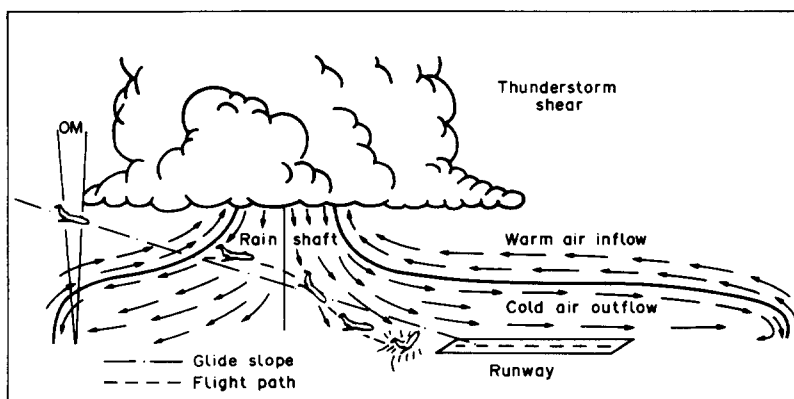
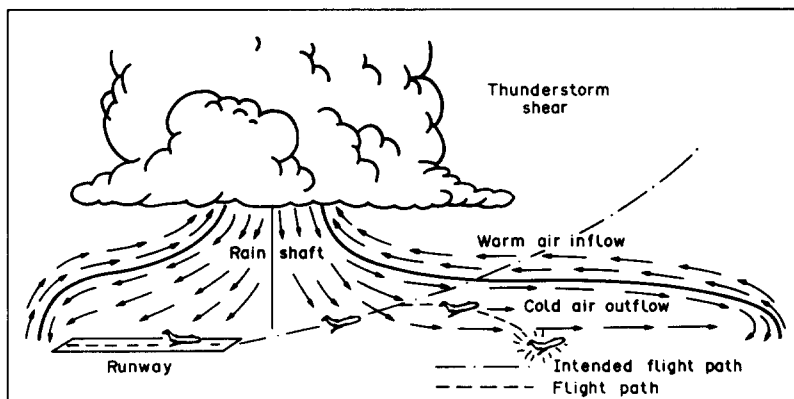


FIG. 59. Thunderstorm shear.

What might happen to an aircraft that tries to take-off or approach to land, respectively, in thunderstorm shears, is shown in Fig. 59.

Microbursts are small but intense downdrafts that last only a short period of time. Close to the ground they cause severe head and tail winds and are of great concern to the pilot, when encountered during final approach or just after lift off at altitudes below 2000 ft. The

Joint Weather Studies (JAWS) field experiment,<sup>(74)</sup> conducted at Stapleton Airport near Denver in 1982, provided radar measured data of some 190 microbursts less than 2 nautical miles in diameter. Approach and take-off windshear profiles as a result of the JAWS-data, are programmed and used in flight training simulators. The so-called 'ring-vortex downburst model' provides a mathematical model for the simulation of microbursts.<sup>(78)</sup>

#### 5.4. GROUND HANDLING

Some of the most important factors affecting airplane performance on runways and taxi tracks are the characteristics of the landing gear. The methods used to model an airplane in flight apply equally well to its modelling, while moving on the ground. The landing gear model should allow the tyres, wheels, suspension, and steering of the airplane to be simulated. The special properties of the ground surface, as well as the aerodynamic effects as speed increases must also be reproduced.

The ability to simulate take-off and landing emerges when the non-linear airborne model, as described in Section 5.2.2, and the representative ground-roll model are combined. Furthermore the aerodynamic changes associated with flight close to the ground<sup>(67)</sup> should be added to the aerodynamic model, as non-linear incremental lift, drag and pitching moments due to ground-effect.<sup>(68,69)</sup>

As an example, the landing gear model of the De Havilland DHC-2 BEAVER laboratory aircraft of DUT (Fig. 37) is described below. The landing gear of the DHC-2 BEAVER consists of two non-retractable main gears and a tail-wheel, connected to the rudder.

##### *The landing gear model*

The DHC-2 BEAVER landing gear model consists of three separate models:<sup>(92)</sup>

- (1) the longitudinal force model,
- (2) the lateral force model,
- (3) the vertical force model.

As the longitudinal and lateral forces generated by the landing gear model depend on the vertical or normal force  $F_V$  on each gear, the vertical force model is described first. Table 9 presents the DHC-2 landing gear data, to be used in the three models described below.

##### *The vertical force model*

The vertical force model generates vertical forces on the airplane as a function of:

- the tyre deflection ( $\delta_t$ )
- the strut deflection ( $\delta_s$ ), where total gear deflection  $\delta_g = \delta_t + \delta_s$
- the gear rate of deflection ( $\dot{\delta}_g$ ).

The total deflection of each landing gear strut  $\delta_g$  and deflection rate  $\dot{\delta}_g$  follows from (Fig. 60):

$$\delta_g = z_1 - h_{c.g.} - x_1 \sin \theta + y_1 \sin \varphi \quad (5.48)$$

$$\dot{\delta}_g = -\dot{h}_{c.g.} - x_1 \dot{\theta} \cos \theta + y_1 \dot{\varphi} \cos \varphi, \quad (5.49)$$

where the coordinates of the landing gear struts in the measurement reference frame,  $F_M$  (see Fig. 61), are determined from the airplane c.g. position and from the gear geometry ( $x_0$ ,  $y_0$  and  $z_0$ , measured in  $F_M$ ):

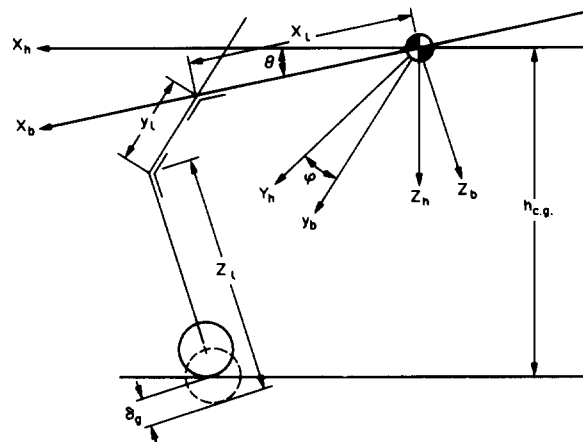
$$x_1 = x_{c.g.} + x_0 \quad (x_{c.g.} \text{ positive in } F_M)$$

$$y_1 = y_{c.g.} + y_0$$

$$z_1 = z_{c.g.} + z_0 \quad (z_{c.g.} \text{ negative in } F_M).$$

TABLE 9. BEAVER LANDING GEAR DATA

|                    |   |                         |
|--------------------|---|-------------------------|
| $a$                | constant depending on runway condition          | 1.0                     |
| $b_M$              | tyre-width main-gears                           | 0.216 m                 |
| $b_T$              | tyre-width tailwheel                            | 0.140 m                 |
| $c_{v_M}$          | strut damping constant main-gears               | 10.000 N S/m            |
| $c_{v_T}$          | strut damping constant tail-gear                | 40.000 N S/m            |
| $D_M$              | tyre diameter main-gears                        | 0.625 m                 |
| $D_T$              | tyre diameter tailwheel                         | 0.340 m                 |
| $g$                | gravity acceleration                            | 9.81 m/sec <sup>2</sup> |
| $P_M$              | preload main-gear struts                        | 2500 N                  |
| $P_T$              | preload tail-gear strut                         | 540 N                   |
| $P_{O_M}$          | operating tyre pressure ratio main              | 172400 N/m <sup>2</sup> |
| $P_{O_T}$          | operating tyre pressure ratio tail              | 210200 N/m <sup>2</sup> |
| $P_{r_M}$          | actual tyre pressure ratio main                 | 282700 N/m <sup>2</sup> |
| $P_{r_T}$          | actual tyre pressure ratio tail                 | 344700 N/m <sup>2</sup> |
| $x_{o_L}$          | $x$ -coordinate strut left (measured in $F_M$ ) | - 0.1875 m              |
| $x_{o_R}$          | $x$ -coordinate strut right                     | - 0.1875 m              |
| $x_{o_T}$          | $x$ -coordinate strut tail (measured in $F_M$ ) | + 7.1 m                 |
| $y_{o_L}$          | $y$ -coordinate strut left                      | + 1.55 m                |
| $y_{o_R}$          | $y$ -coordinate strut right                     | - 1.55 m                |
| $y_{o_T}$          | $y$ -coordinate strut tail                      | 0 m                     |
| $z_{o_L}$          | $z$ -coordinate strut left (measured in $F_M$ ) | - 2.875 m               |
| $z_{o_R}$          | $z$ -coordinate strut right                     | - 2.875 m               |
| $z_{o_T}$          | $z$ -coordinate strut tail (measured in $F_M$ ) | - 1.775 m               |
| $\delta_{s\max_M}$ | maximum strut deflection main-gears             | 0.15 m                  |
| $\delta_{s\max_T}$ | maximum strut deflection tail-gear              | 0.1 m                   |
| $\epsilon_{\max}$  | maximum tail wheel steering angle               | 0.26 rad                |
| $\rho_d$           | runway dependent friction coefficient           | 0.8                     |
| $\rho_M$           | side force friction coefficient                 | 0.6                     |
| $\mu_{B\max}$      | maximum braking friction coefficient            | 0.65                    |
| $\mu_{roi}$        | rolling friction coefficient                    | 0.02                    |



$$h_{c,g} = (z_l - \delta_g) \cos \theta \cos \varphi + y_l \sin \varphi - x_l \sin \theta$$

$$\delta_g = z_l - \frac{1}{\cos \theta \cos \varphi} (h_{c,g} + x_l \sin \theta - y_l \sin \varphi)$$

assume that:  $\cos \theta \cos \varphi = 1$

$$\delta_g = z_l - h_{c,g} - x_l \sin \theta + y_l \sin \varphi$$

FIG. 60. Computation of the total gear deflection  $\delta_g$ .

Three conditions are possible, depending on the value of  $\delta_g$ :

(1)  $\delta_g \leq 0$

This landing gear strut makes no ground contact and so:

$F_v = 0$  and  $\delta_g = 0$ .

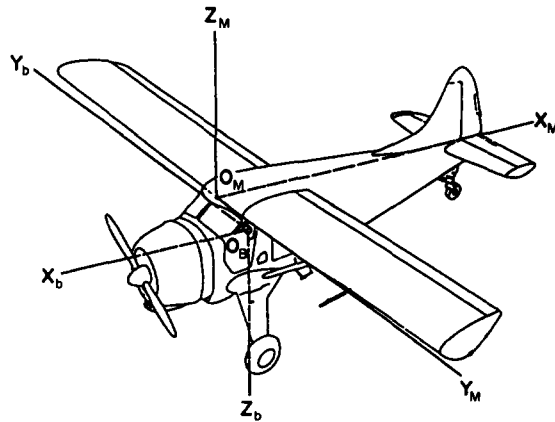


FIG. 61. The measurement reference frame  $F_M$  and the body-fixed reference frame  $F_b$ .

(2)  $\delta_g > 0$  and  $\delta_s = 0$

The strut makes ground contact, but the vertical force  $F_v$  does not exceed the preload of the strut  $P$  ( $F_v \leq P$ ), so:

$$\delta_g = \delta_t \quad \text{and} \quad F_v = P \frac{\delta_g}{\delta_{t_p}}$$

where

$P$  = preload of the landing gear strut,  
 $\delta_{t_p}$  = deflection of the tyre for  $F_v = P$ .

(3)  $\delta_g > 0$  and  $\delta_s > 0$

In this case the vertical force exceeds the preload of the strut ( $F_v > P$ ). The strut damping force ( $F_D$ ) is considered to be linear with the gear deflection rate  $\dot{\delta}_g$ . So, in this case the vertical force yields:

$$F_v = P \frac{\delta_{g_{max}}}{(\delta_{g_{max}} + \delta_{t_p} - \delta_g)} + F_D$$

where

$\delta_{g_{max}}$  = maximum deflection of the strut,  
 $F_D = c_v \cdot \dot{\delta}_g$  ( $c_v$  = damping constant).

Figure 62 shows the vertical force as a function of static gear deflection of the BEAVER-main gears.

#### *The lateral force model*

The lateral or side forces, which are forces along the Earth's surface and orthogonal to the  $X_h$ -axis (see Fig. 60 and below) are determined by the tyre ground-slip angles.<sup>(92)</sup> A tyre ground-slip angle (tyre yaw angle) is the angle between the aircraft velocity vector and a tyre symmetrical axis. The equation for a tyre ground-slip angle reads:

$$\gamma = \tan^{-1} \left( \frac{V_y + x_1 \cdot r}{|V_x - y_1 \cdot r|} \right)$$

where  $V_x$  and  $V_y$  are the airplane velocity components along the  $X_h$ - and  $Y_h$ -axes, respectively:

$$V_x = V_N \cos \psi + V_E \sin \psi,$$

$$V_y = V_E \cos \psi - V_N \sin \psi,$$

$r$  = airplane yaw rate.

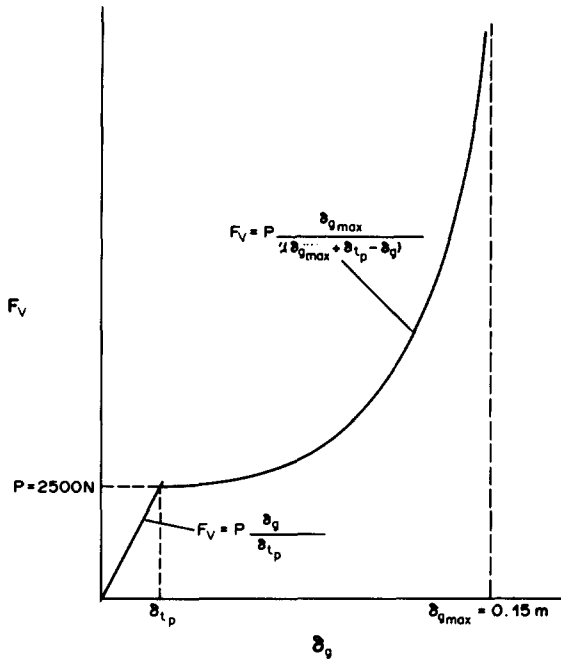


FIG. 62. The vertical force  $F_v$  as a function of static gear deflection of the BEAVER-maingears.

The tailwheel steering angle ( $\varepsilon$ ) compensates the ground-slip angle of the tailwheel:

$$\gamma_T = \gamma - \varepsilon, \quad \text{where} \quad \varepsilon = \frac{\delta_r}{\delta_{r_{\max}}} \varepsilon_{\max}.$$

The 'tyre deflection diameter ratio'  $\kappa$  is represented by:

$$\kappa = (\delta_g - \delta_s)/D.$$

The 'cornering gain'  $CO$  represents the side force, which is generated on a dry surface per unit ground-slip angle (at small ground-slip angles):

$$CO = (p_o + 0.44 p_r) \cdot b^2 \cdot n,$$

where  $p_o$  = operating tyre pressure ratio,  $p_r$  = actual tyre pressure ratio,  $b$  = tyre width,  $n$  = tyre cornering gain parameter.

The 'tyre cornering gain parameter'  $n$  depends on the value of  $\kappa$ :

$$\kappa < 0.0875: n = 1.2 \kappa - 8.8 \kappa^2$$

$$\kappa \geq 0.0875: n = 0.0674 - 0.34 \kappa.$$

Now a dummy 'working parameter'  $w_p$  is introduced:

$$w_p = \frac{CO \cdot \gamma}{F_v \cdot \rho_d}$$

where  $\rho_d$  represents the ground-slip angle, for which the maximum side force will occur;  $\rho_d$  is a runway condition dependent friction coefficient, which will be larger on a dry surface than on a wet surface.

The 'force ratio'  $FO$  depends on the absolute value of  $w_p$ :

$$|w_p| < 1.5: FO = w_p \cdot \left( 1 - \frac{4}{27} \cdot w_p^2 \right)$$

$$|w_p| \geq 1.5: FO = \frac{w_p}{|w_p|} \cdot \sin \left( \frac{\pi}{1 + \frac{2}{3} |w_p|^a} \right),$$

where the 'force ratio' determines the ratio between the actual side force and the maximum side force. The parameter  $a$  is a constant depending on runway condition. On a dry surface  $a$  will be larger than on a wet surface. Using the 'force ratio', the side force  $F_s$  on each tyre becomes:

$$F_s = F_v \cdot FO \cdot \rho_M$$

where  $\rho_M$  is the side force friction coefficient, depending on the forward velocity of the airplane and on the runway surface condition.

### *The longitudinal force model*

The longitudinal force model generates longitudinal forces along the  $X_h$ -axis as a function of:

- the brake pedal deflection ( $\delta_{bp}$ ),
- the vertical force ( $F_v$ ) on each gear,
- the braking friction coefficient ( $\mu_B$ ),
- the rolling friction coefficient ( $\mu_{rol}$ ).

The braking friction coefficient depends on the brake pedal deflection,  $\delta_{bp}$ :

$$\mu_B = \mu_{B_{max}} \cdot \delta_{bp} / \delta_{bp_{max}}$$

where  $\mu_{B_{max}}$  = maximum braking friction coefficient,  $\delta_{bp_{max}}$  = maximum brake pedal deflection.

The rolling friction on each landing gear is taken into account, by adding the rolling friction coefficient to the braking friction coefficient:

$$\mu = \mu_B + \mu_{rol}$$

where  $\mu$  = the effective friction coefficient.

Using the effective friction coefficient, the longitudinal force  $F_\mu$  on each main gear becomes:

$$F_{\mu_{L,R}} = F_{V_{L,R}} \cdot \mu.$$

The longitudinal force and side force on the tailwheel become:

$$F_{\mu_T} = F_{V_T} \cdot \mu_{rol} + |F_{S_T} \cdot \sin \varepsilon|$$

$$F_{S_T} = F_{S_T} \cdot \cos \varepsilon.$$

#### *5.4.1. Transformation of the Landing Gear Forces to Body Axes*

The vertical, lateral and longitudinal landing gear forces are calculated in the heading attached vertical axis reference frame,  $F_h$ . In the case of a flat Earth, the  $X_h$ -axis is the projection of the airplane's  $X_b$ -axis on the horizontal plane (Fig. 60). Therefore the landing gear forces have to be transformed to body axes, in order to be added to the external forces and moments acting on the airplane (Eqs (5.12)). For each landing gear, the forces in body axes result from:

$$\begin{array}{l|llll|l} |F_x| & -\cos \theta & 0 & \sin \theta & |F_\mu| \\ |F_y| & -\sin \theta \sin \varphi & -\cos \varphi & -\cos \theta \sin \varphi & \cdot |F_s| \\ |F_z| & -\sin \theta \cos \varphi & \sin \varphi & -\cos \theta \cos \varphi & |F_v| \end{array}$$

The external forces due to landing gear ground contact in Eqs (5.12) now become:

$$X_{LG} = (F_x)_L + (F_x)_R + (F_x)_T,$$

$$Y_{LG} = (F_y)_L + (F_y)_R + (F_y)_T,$$

$$Z_{LG} = (F_z)_L + (F_z)_R + (F_z)_T.$$

The external moments due to landing gear ground contact in Eqs (5.12) become:

$$\begin{aligned}|L_{LG}| &= |0 \quad -z_{l_c} \quad y_l| \cdot |F_X| \\|M_{LG}| = \Sigma_i &|z_{l_c} \quad 0 \quad -x_l| \cdot |F_Y| \\|N_{LG}| &= |-y_l \quad x_l \quad 0| \cdot |F_Z|\end{aligned}$$

where  $z_{l_c}$  is the actual length of each landing gear strut, corrected for the gear deflection, according to:  $z_{l_c} = z_l - \delta_g$ ,  $i$  is the contribution of the left main gear (L), the right main gear (R) and the tailwheel (T) to the external moments.

### 5.5. MATHEMATICAL MODEL IDENTIFICATION, BASED ON FLIGHT AND TAXI TESTS

This section describes a case history.

In the spring of 1986 the National Aerospace Laboratory (NLR) in Amsterdam and the Faculty of Aerospace Engineering of DUT were selected to develop the mathematical model and data package of a Cessna Citation 500 jet aircraft (Fig. 63). These aircraft are

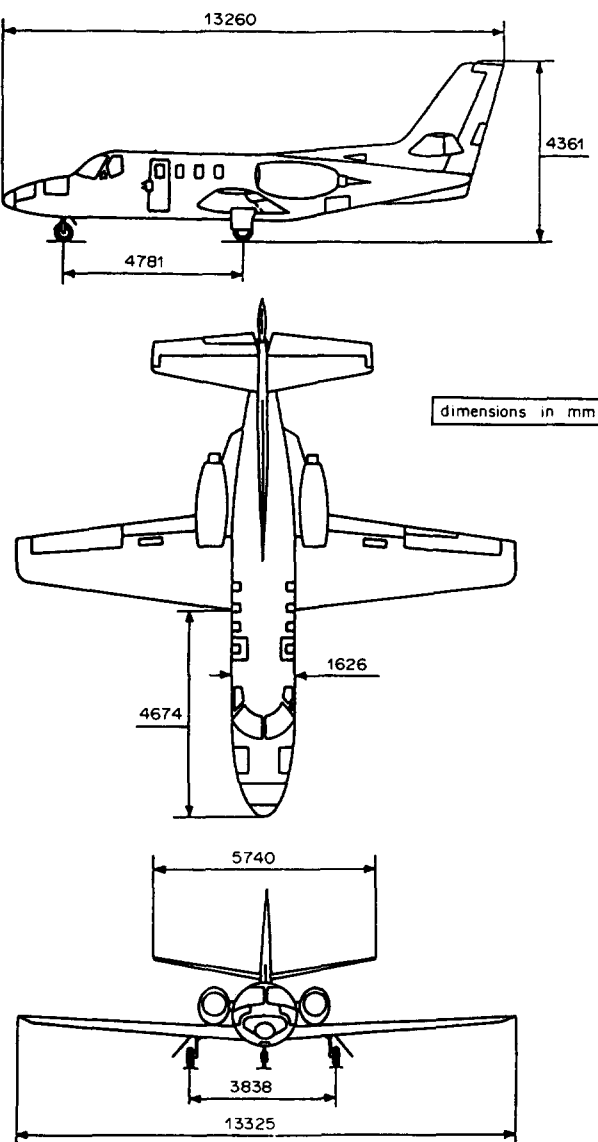


FIG. 63. Citation 500 overall dimensions.

used by the Dutch Government Civil Aviation School, RLS, in the final part of civil aviation pilot training. By purchasing a FAA Phase II flight simulator for the Citation, the objective was to transfer part of the type training from the aircraft to the simulator, enabling the RLS to reduce its fleet from six to three Citations. It was expected that using the simulator would improve the cost effectiveness and the quality of the advanced flight training course.

The Citation 500 was developed in the late sixties. At that time there was much less emphasis on flight simulation. Therefore it was no surprise that an adequate simulation model of the aircraft did not yet exist. The problem is not unique and applies to many existing aircraft types for which advanced simulation facilities are wanted. A possible option is to execute a flight test program with one of the available aircraft in order to form a database from which an accurate mathematical model can be developed.

At first sight, this may look like a very expensive solution, but in the case at hand a flight test program was necessary anyway, since Phase II certification of a flight simulator requires a successful 'Proof of Match'. This means that simulated responses are to be directly compared to aircraft flight traces, permitting an objective examination of the fidelity of the mathematical model and data package.

### 5.5.1. *A Priori Models*

To gain insight at an early stage in the structure of the mathematical models of the aerodynamic forces and moments, the static and dynamic engine performance, the mass properties, the flight control system and the landing gear, it was decided to build a priori models of these aircraft systems to be simulated. The a priori models are based on available flight test and wind tunnel data, complemented with data of comparable aircraft and engineering judgement. They are formulated in accordance with the requirements prescribed by IATA.<sup>(44)</sup> In this way rather comprehensive models were developed, including all kinds of non-linearities and dependencies on the aircraft state. Coefficients or functions, which were not available for the a priori models from the preliminary database, were initially set to zero. Also from a software managing point of view, it was supposed to be a good philosophy to develop these comprehensive models in advance, where time was less restricted, than during the rather short period available for the analysis of the flight test data and the development of the final models. If later on particular parts of the models appeared to be insignificant or could not be identified from the flight test data, it would be much simpler to set the corresponding coefficients to zero, rather than having to expand the model.

Below, the a priori aerodynamic lift coefficient will be compared to the lift coefficient in the final aerodynamic model, resulting from flight test data analysis.

For the a priori engine model, data were obtained from the General Installed Turbofan Performance Program, issued by United Aircraft of Canada Ltd for the commercial version of the Pratt & Whitney (Canada) JT15D turbosfan. This computer program was used to generate power setting values of fan speed, resulting in not less than minimum rated thrust on production engines. The program, which is of the curve reading type, was adapted to run on the CDC Cyber of NLR as well as on the Gould 32/87 of DUT. An example of the calculations performed using this program is presented in Fig. 64, where corrected net thrust is plotted versus fan speed as a function of MACH ( $M$ ) and flight level ( $FL$ ).

The major further development of the engine model was the transient model to incorporate realistic variations of all engine parameters with Power Lever Angle (PLA) command, including start-up and shut-down.

The mass properties model, which describes the centre of gravity (c.g.) position and the moments of inertia of the Citation 500 for several loading conditions, was developed using the Weight and Balance Manual of the Citation.<sup>(65)</sup> The moment and product of inertia envelopes were calculated for several configurations, using calculated fuel inertia and inertia data of the complete aircraft, received by early 1987. Figure 65 shows the yawing moment of inertia envelope resulting from these calculations.

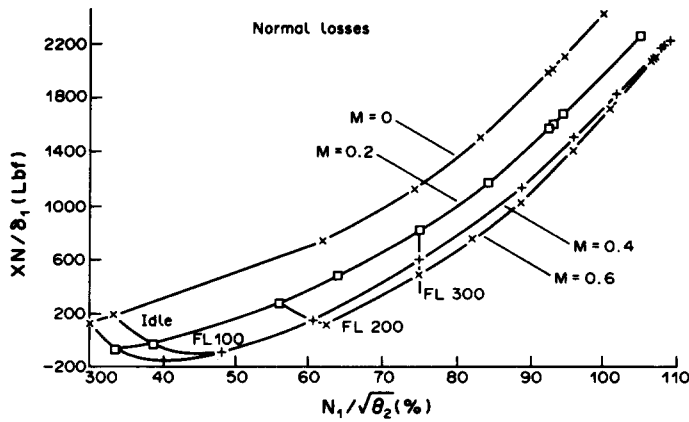


FIG. 64. Net thrust vs fan speed as a function of Mach and flight level.

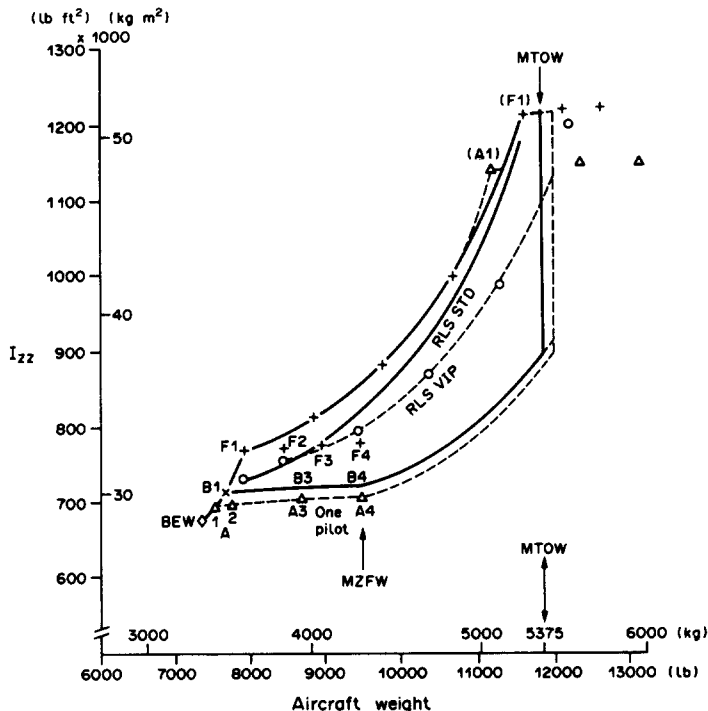


FIG. 65. Yaw moment of inertia envelope.

To describe the Citation 500 flight control system, which is fully mechanical, a simple second order system was used in the a priori control force system model.<sup>(45)</sup> Below, the final flight control system model will be described which resulted from the identification of the Citation 500 flight controls, using flight test measurements.<sup>(57)</sup>

In the a priori landing gear model, describing the conventional tri-cycle landing gear of the Citation, three submodels are being considered, i.e. those for the vertical forces, the side forces and the longitudinal forces due to aircraft ground contact, see Section 5.4. For the simulation of 'minimum unstick speed' a tailscraper was added to the model. The final landing gear model, identified from flight and taxi tests, will be briefly described below.

The a priori models were implemented on the Gould 32/87 Super Mini computer driving the moving-base visual flight simulator of DUT, see Fig. 11. After integration of the models within the DUT flight simulation software, see Section 4.2, it was possible to fly the 'a priori

Citation' on-line with the pilot-in-the-loop. This gave the opportunity to check the functioning and flyability of the models at an early stage by our pilot-engineers and pilots from the Civil Aviation School.

### 5.5.2. Flight Test Measurement System

One of the RLS Citations was equipped with an advanced high accuracy flight test measurement system. The rack of the measurement system, as installed in the Citation cabin, which is identical to the racks used in the Fokker-100 and Fokker-50 flight test programs, contains a Honeywell laser-gyro Inertial Reference System (IRS) to measure specific aerodynamic or ground reaction forces and aircraft body rotation rates and accelerations. High accuracy pressure transducers in a temperature controlled box were used to measure airspeed and altitude variations in quasi steady flight. A variety of other variables was measured in addition, such as primary control forces and displacements,

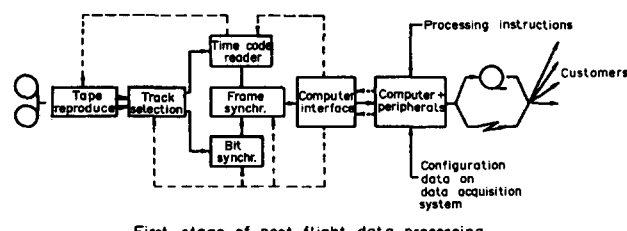
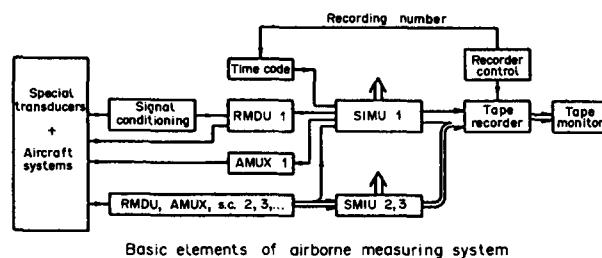
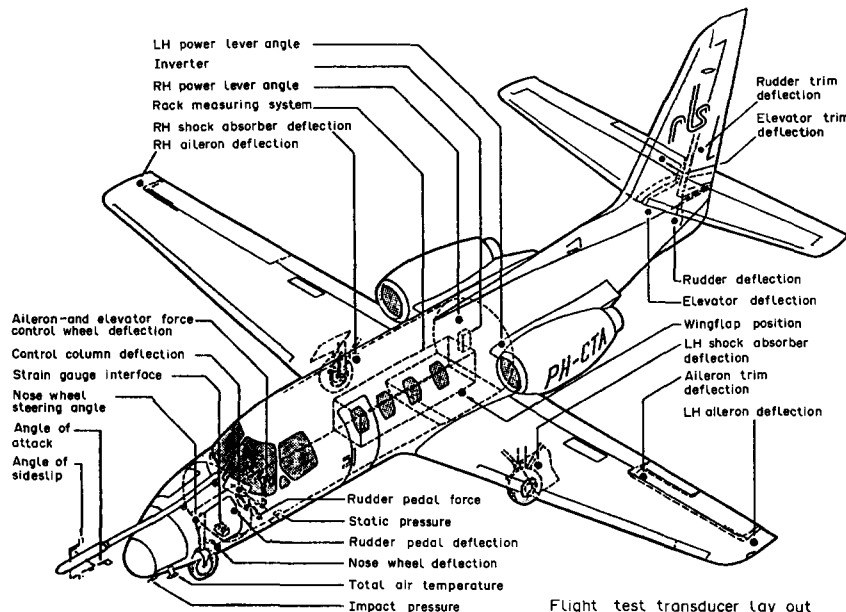


FIG. 66. Transducer lay out, airborne measuring system and post flight data processing.

elevator, aileron, rudder and trimtab deflections, angle of attack and side-slip angle, using a specially designed nose boom. Where possible, standard onboard systems were used, such as for the measurement of engine speeds, inter-turbine temperature (ITT) and fuel flow, fuel quantity, stick shaker, anti-skid warning, landing gear down- and up-locks, speed brakes extended/retracted and radar altitude.<sup>(85)</sup> All these physical quantities were converted into electrical signals, which after signal conditioning are digitized using a Remote Multiplexer Digitizer Unit, RMDU, see Fig. 66. Data from modern avionics that complied with the ARINC standard were processed using an ARINC multiplexer (AMUX). Digitized data were stored on a 14 track magnetic tape recorder with enough capacity to allow continuous recording of all transducer outputs during the complete test flight, from before engine start until after engine shut down. A reference time signal was recorded on a separate track for correlation of the data tracks. Transducer signals were, depending on frequency contents, sampled with sample frequencies ranging from 2 to 50 Hz. However, for vibration measurements, three accelerometers positioned in the cockpit were sampled at a frequency of 256 Hz. Also sound measurements were recorded in another Citation cockpit, using two microphones.<sup>(88)</sup>

The first stage of post flight data processing consisted of adding the time to the measured data, using a frame synchronizer and expressing the recorded data in engineering units. The recorded data were corrected according to the calibration information of the measured channel and properly grouped to be used in the second stage of data analysis concerned with aircraft state reconstruction and mathematical model identification.

#### *5.5.3. Flight Test Program*

A flight test program was carried out with the instrumented Citation, the objectives of which were the execution and measurement of different kinds of flight test maneuvers for the identification of the FAA Phase II flight simulation model and also for the measurement of input-output time histories, as required in the Approval Test Guide (ATG).<sup>(66)</sup> The flight test program for model identification was designed such that flight test maneuvers were evenly distributed in the admissible flight envelope. Two types of flight test maneuvers were applied for model identification:

- quasi-stationary maneuvers for large but slow variations of input and state variables;
- dynamic maneuvers for fast but small variations of input and state variables.

The quasi-stationary maneuvers were performed to evaluate non-linear effects in the aerodynamic and flight control system models. Examples of quasi-stationary maneuvers were accelerations and decelerations at constant thrust and altitude, 'slow' pull-up-push-down maneuvers, side slips with varying side-slip angles, trimtab excursions at a constant nominal flight condition and wind-up turns.

The dynamic maneuvers were carried out to determine the performance and stability characteristics of the aircraft. Examples of dynamic maneuvers were the responses to manually implemented, approximately block-shaped control displacements. These so-called doublets were sequentially implemented on the elevator, ailerons, rudder and left and right power levers, starting from steady, straight flight.

Quasi-stationary and dynamic maneuvers were executed for all relevant and admissible flight conditions and aircraft configuration combinations. In addition, extensive measurements were taken of dynamic engine responses, airplane stalls, aerodynamic ground effects, take-off and landing performance and ground handling characteristics.

The Approval Test Guide (ATG) prescribes measurements in stationary flight conditions as well as in special dynamic maneuvers. The measurement results of the ATG maneuvers were to be used in the 'Proof of Match'. Some results will be presented below.

#### *5.5.4. System Identification Techniques*

Two different types of system identification techniques<sup>(72)</sup> were applied to develop the mathematical models of the aerodynamic forces and moments, static and dynamic engine

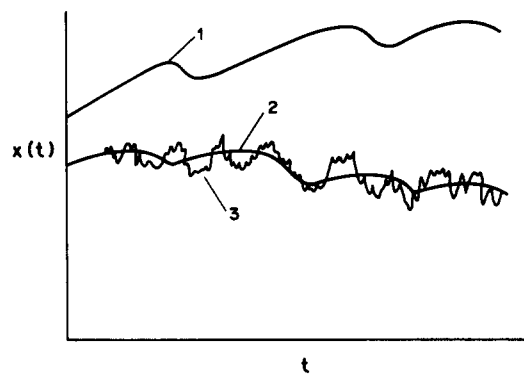


FIG. 67. Principle of model-adjustment technique.

performance, the flight control system including aerodynamic control surface hinge moments and the landing gear, including nose wheel steering and main wheel brakes.

The first type (type 1) of system identification technique may be characterized as 'model-adjustment technique' (Fig. 67). The idea is to implement a simulation model in the computer and to drive the model with the same inputs as the actual system. If the simulated output differs from the output of the actual system (curve 1 in Fig. 67), this must be caused by a difference in initial conditions and/or the parameters in the simulation model, having wrong values. Next, some—usually quadratic—function of the difference between actual and simulated output is minimized with respect to both initial conditions and model parameter values. The technique may be interpreted in terms of statistical estimation theory. The optimal parameter values produce the minimum value of the so-called Likelihood Function and may result in the simulation curve 2 in Fig. 67.

The second type (type 2) of system identification technique is based on explicit mathematical relations, expressing parameter values in terms of system input and output measurements. The so-called 'equation error' methods fall in this category. The explicit mathematical relations follow immediately from regression analysis. In cases where the model structure is not yet precisely known, the type 2 identification technique results in a much easier model developments process than the type 1 identification technique.

In the present series of flight test measurements, the presence of virtually perfect accelerometers and rate gyros in the measurement system was fully exploited. The corresponding signals i.e. specific external forces and body rotation rates were interpreted as input signals to a dynamic system model describing the evolution of the aircraft's state.<sup>(84)</sup> A state reconstruction problem was defined, which was readily solved by applying a type 1 system identification technique. Computed time histories, of for instance airspeed and side slip angle, were matched to corresponding measured time histories by selecting 'optimal' initial conditions and estimating (very small) transducer bias errors. This resulted in an accurate and complete state vector trajectory estimate. As the model was almost exactly known, the state reconstruction needed to be solved only once for each particular flight test maneuver. The main advantage of carrying out a state reconstruction is that next, a type 2 system identification technique may be applied to estimate the aerodynamic derivatives (Table 10). All identified models are shown in this table, below the system identification

TABLE 10. CLASSIFICATION OF IDENTIFICATION PROBLEMS

| System Identification Technique |  |
|---------------------------------|--|
| Type 1                          | Type 2                                   |
| aircraft state trajectory       | aerodynamic forces and moments           |
| dynamic engine response         | static engine performance                |
| flight control system           | flight control system                    |
| landing gear side forces        | landing gear strut and wheel compression |
| nose wheel steering             | main wheel brakes                        |

technique applied. The performance of this 'two step' method to identify the aerodynamic derivatives is demonstrated in the 'Proof of Match' time histories, which will be discussed below.

### 5.5.5. Flight Test Data Analysis

The application of the above two-step identification method is now discussed, taking the analysis and modelling of the aerodynamic lift coefficient ( $C_L$ ) as an example. At the start of the analysis it was decided to concentrate in the first instance on the quasi-stationary-horizontal symmetrical reference conditions and the corresponding dynamic maneuvers at the test conditions in the entire flight envelope. The analysis of these test conditions was used both for the evaluation of the performance model as well as for the additional stability and control parts. The test points for the clean configuration are presented in a  $C_L$ -MACH plot in Fig. 68. As a reference, also plotted herein are  $M^2 C_L$  over corrected aircraft weight curves at four test altitudes. The aircraft weight ( $W$ ) is chosen to represent the mean value of the test weights at that particular altitude. Additionally, in Fig. 68 the  $C_L$  excursions as a result of elevator doublets with large amplitude are depicted. The figure also shows the low speed stall and the high speed buffet boundaries for the clean configuration. For each test point in the flight envelope, a submodel was postulated for the three aerodynamic forces ( $C_D$ ,  $C_L$ ,  $C_Y$ ) and moment coefficients ( $C_m$ ,  $C_i$ ,  $C_n$ ) in the model axes reference frame,  $F_{mo}$ .

The submodel for the lift coefficient, expressed in Eq. (5.50), is valid within the normal flight envelope, which means that stall phenomena, buffeting, ground effect etc. are not represented.

$$C_L = C_{L_0} + C_{L_a} \cdot \alpha + C_{L_{a^2}} \cdot \alpha^2 + C_{L_q} \cdot \frac{q\bar{c}}{V} + C_{L_{\delta_e}} \cdot \delta_e \quad (5.50)$$

Because of the size of the aircraft and the speed regime of interest, the aircraft was assumed to be rigid. This eliminated the dynamic modelling of additional degrees of freedom due to flexibility. Quasi-static modelling of elastic effects was considered only by making coefficients dependent on Mach.

In Fig. 69 test points at constant altitude and c.g. position are presented in a  $C_L$ - $\alpha$  plot. Because different Mach numbers are attached to each  $C_L$  value, Mach effects are embedded.

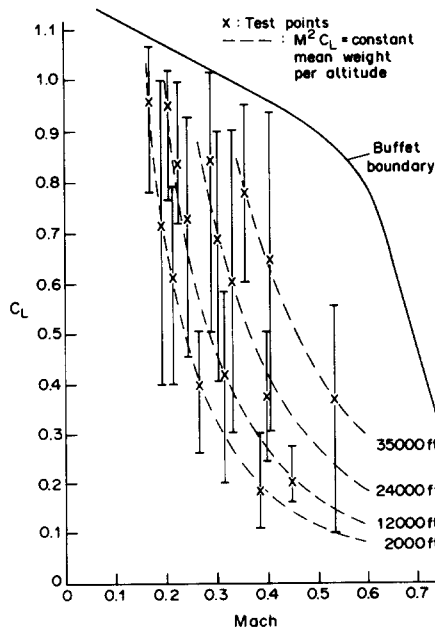


FIG. 68. Angle of attack sweeps for the clean configuration.

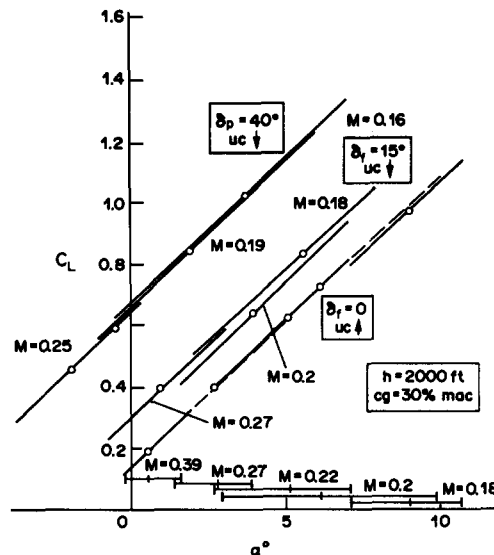


FIG. 69.  $C_L-\alpha$  curves following from submodels for various flap settings.

Apart from the reference conditions, the  $\alpha$ -sweeps are shown as a result of the elevator doublets.

Because the  $\alpha$ -sweeps were performed at approximately constant Mach number, Fig. 69 shows that  $C_L$  is described by different curves for each aircraft configuration. The flight test results therefore confirm that straight, rather thick wings encounter Mach-effects at low Mach numbers.

After integration of the submodels for the lift, drag and pitching moment, it was possible for example to construct  $C_L/C_D$  curves for various Mach numbers. Figure 70 shows these curves for the clean configuration resulting from the analysis. Also presented in this figure are the test points at the four flight test altitudes. For all configurations of interest, the coefficients in the submodels were determined using regression analysis and subsequently

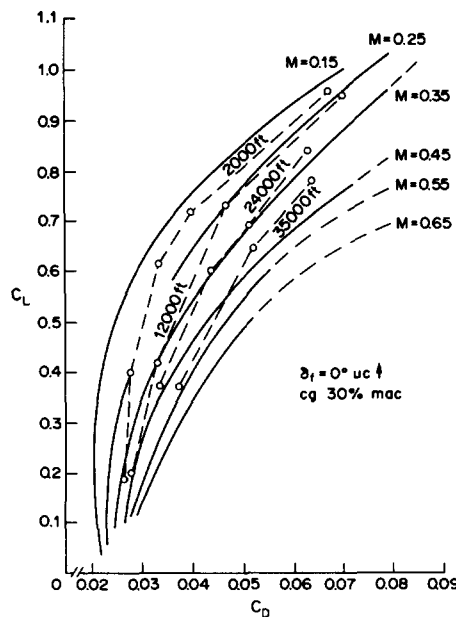


FIG. 70.  $C_L/C_D$  curves for constant Mach numbers derived from flight test data.

integrated to  $C_L(M)-\alpha$ ,  $C_D(M)-\alpha$  and  $C_m(M)-\alpha$  plots for increasing Mach numbers. The clean configuration was considered as a base. Effects due to flap, gear and speedbrake extension were modelled as incremental contributions, which were superimposed on the base model.

As a result of the data processing, a large data set of stability and control coefficients was obtained, valid for the individual test conditions. In accordance with the performance model for the lift coefficient, these coefficients were formulated as global functions of angle of attack.

#### 5.5.6. Final Models

As a result of the flight test data analysis the a priori aerodynamic lift coefficient has been compared in detail to the final lift coefficient in Ref. 45. Some results of this comparison are discussed below.

The a priori lift coefficient  $C_L(\alpha, M)$  was subdivided into  $C_{L_0}(M)$  at  $\alpha$  equal to zero and  $C_{L_\alpha}(M)$  multiplied by  $\alpha$  (see Figs 71 and 72) respectively. In the final lift coefficient for the clean configuration, these figures are replaced by Fig. 73, showing  $C_L$ -curves as a function of angle of attack for increasing Mach numbers.

Figures 74 and 75 present the comparison for  $\Delta C_L$  as a function of angle of attack and flap setting, showing that the a priori model was not too bad for this case. The comparison

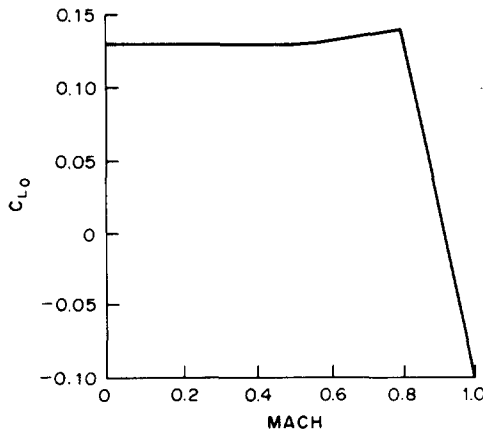


FIG. 71.  $C_{L_0}$  as a function of Mach.

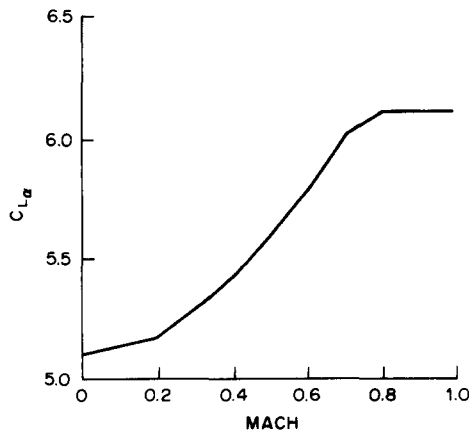
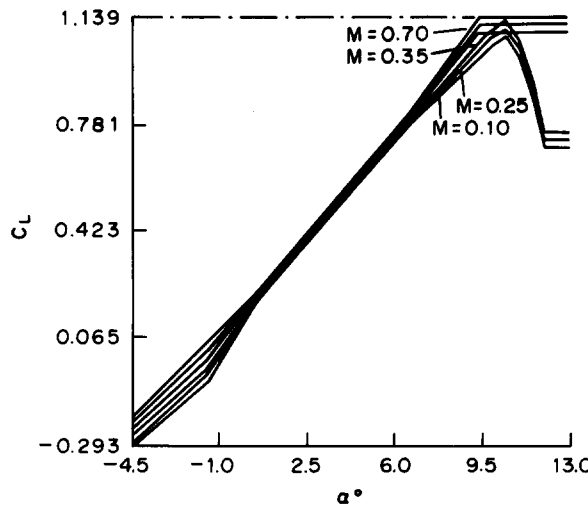
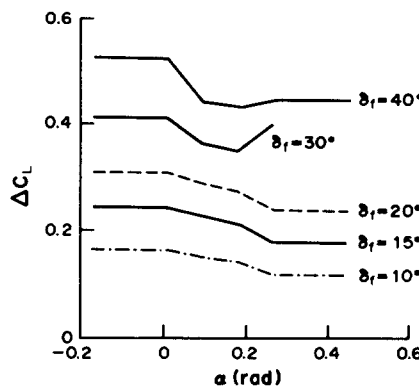
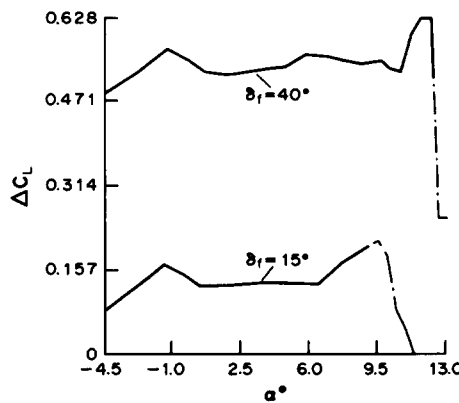
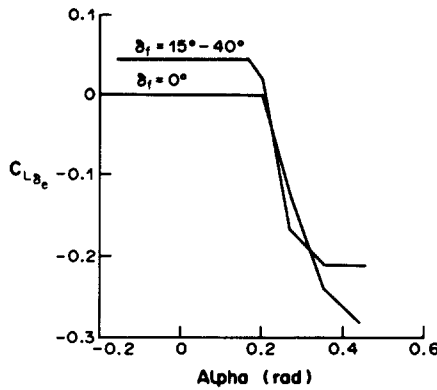
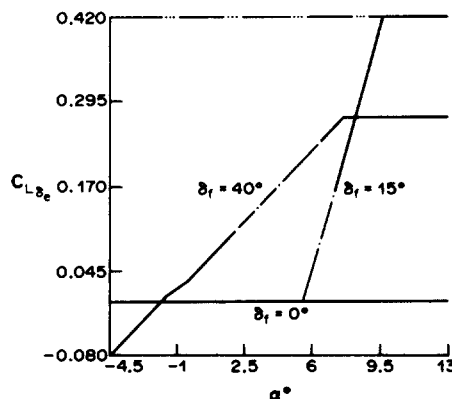


FIG. 72.  $C_{L_\alpha}$  as a function of Mach, clean configuration.

FIG. 73.  $C_L$ - $\alpha$  curves for increasing Mach numbers, clean configuration.FIG. 74.  $\Delta C_L$ - $\alpha$  curves for various flap settings.FIG. 75.  $\Delta C_L$ - $\alpha$  curves for  $\delta_f = 15^\circ$ , resp.  $40^\circ$ .

of the increment in lift coefficient due to elevator deflection ( $C_{L_{\delta_e}}$ ) as a function of angle of attack and flap setting (Figs 76 and 77) results in quite different curves for  $C_{L_{\delta_e}}$ . For the increment in lift coefficient due to pitch rate (Fig. 78a) very little information was available for the a priori model. However, for the final aerodynamic model, this coefficient could be identified as a function of angle of attack and flap position, see Fig. 78b.

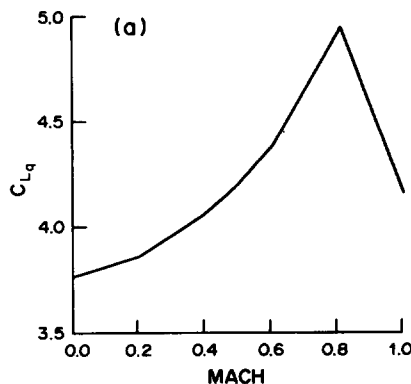
FIG. 76. Increment in  $C_{L_{\alpha}}$  as a function of  $\alpha$  and flap extension.FIG. 77.  $C_{L_{\alpha}}-\alpha$  curves for various flap settings.

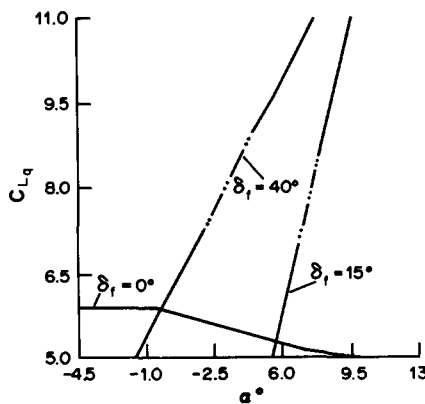
Results of the identification of the complete aerodynamic model will be presented below as 'Proof of Match' time histories.

The final engine model for the P&W JT15D-1 engines was decomposed into two submodels:

- static engine thrust model;
- dynamic engine model.

For the final static engine performance model, the curve reading computer program was used, complemented with existing testbank data from the RLS. From a comparison of

FIG. 78a.  $C_{L_q}$  as a function of Mach and altitude.

FIG. 78b.  $C_{l_4}$ - $\alpha$  curves for various flap settings.

partial climb recordings of the aircraft and the simulation model, it turned out that for engine settings above 90% fan rpm (N1) the model showed superior climb performance relative to the aircraft. Because the angle of attack in flight and simulation corresponded very well in these cases, a discrepancy in the engine model was suspected at high power settings. From an analysis of both partial climb and aircraft acceleration measurements, a correction was applied to the static thrust performance data at the higher power settings.

The dynamic engine model, which is very important in real-time simulation, was developed in a joint cooperation between NLR and CAE. Starting from a basic turbofan engine model, made available by CAE, the operation of the fuel control unit (FCU), governing the LP and HP rotor speeds, the fan and core airflow regulator, the turbine temperature controller etc. was modelled for the JT15D-1. Flight test data during throttle chops and slams were available for the analyses of the engine dynamics. From these data the characteristic functions, parameters and time constants in the model were determined. Power change dynamics of the final engine model are demonstrated in the form of a 'Proof of Match' below.

As the Citation 500 is equipped with a fully manual flight control system (FCS) (Fig. 79) the aerodynamic hinge moments on the control surfaces must be counter balanced by pilot generated control forces. Therefore a model of the aerodynamic hinge moments was an essential part of the FCS model, and the identification<sup>(57)</sup> had to be based on measurements in flight. Model development started from a small set of flight test measurements in one flight condition and for one aircraft configuration. Fourth order models of the elevator and rudder FCS, where only the masses of the forward system (control column and rudder pedals respectively) and the aft system (elevator and rudder) were taken into account, were found to result in an adequate fit to the measured control and surface displacements. The aileron FCS required a 6th rather than a 4th order system model, to account for the masses of the control wheel and each of the ailerons. Since the FCS model represents a dynamical system, type 1 identification methods were applied for selection and estimation of the model parameters at DUT. An alternate approach at NLR, using second order FCS models and type 2 identification techniques (see Table 10) resulted in aerodynamic hinge moment derivatives similar to those obtained by DUT. In the analysis of the flight test maneuvers in all other flight conditions and aircraft configurations, the form of the FCS models was kept constant. This analysis resulted in a detailed map of aerodynamic hinge moment derivatives, which was subsequently implemented in the global FCS simulation model of the Citation. Results in the form of a 'Proof of Match' of the final FCS model are presented below.

The final landing gear model of the Citation consists of four submodels, i.e. the wheel compression and gear strut model, the landing gear side force model, the main wheel brake model and the nose wheel steering model. Type 1 and type 2 identification techniques were used to identify these landing gear submodels (Table 10). Due to the availability of the IRS,

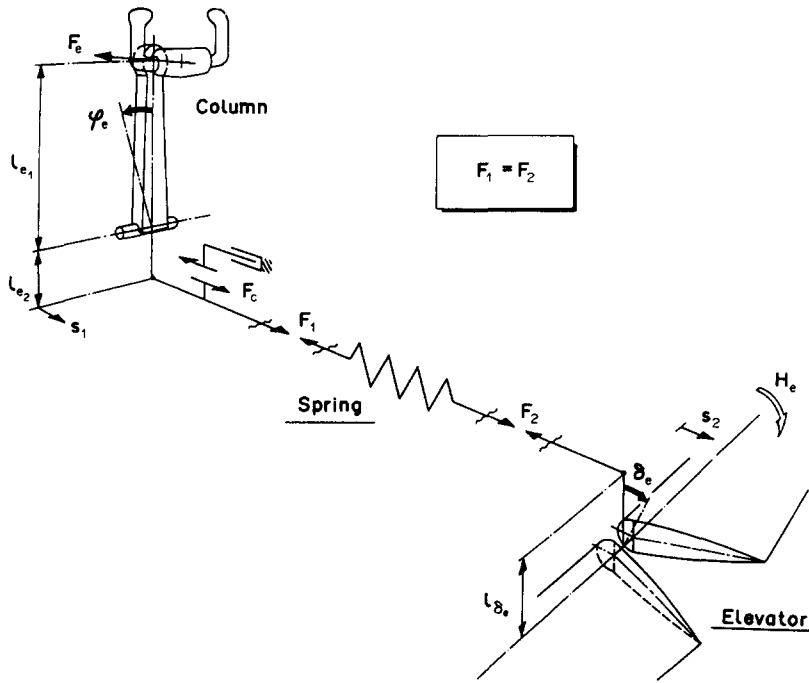


FIG. 79. Cessna Citation 500 elevator control system.

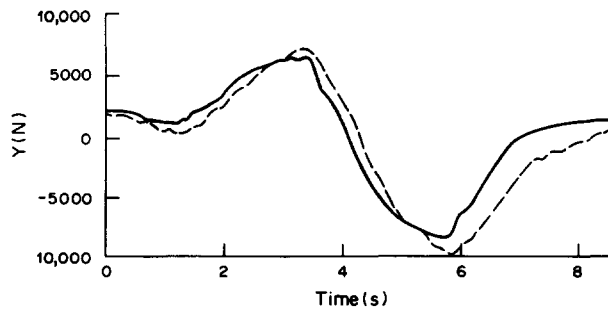


FIG. 80. Total side force during a nose wheel doublet taxi maneuver. — measured; - - - computed.

providing for high accuracy time histories of the external specific forces on the aircraft, the body rotation rates, accelerations and attitude angles, type 2 identification techniques could be applied to identify the wheel compression/gear strut and main wheel brake models. The landing gear side force model could be identified using type 1 identification techniques on a dynamical model, wherein the tyre ground-slip angles were explicitly calculated. A typical result of measured and computed landing gear side force time histories is presented in Fig. 80.

The nose wheel steering system of the Citation is connected via springs to the rudder pedals. Type 1 identification techniques were applied to identify second and fourth order dynamical nose wheel steering models. However, it turned out that a quasi-static model performed surprisingly well (Fig. 81).

In the final landing gear simulation model, the tyre and strut deflections and rates of deflection are computed first, providing for the vertical forces, which play a crucial role in the computation of the side forces and the longitudinal landing gear forces. Parameters related to the condition of the runway surface may have large effects on the magnitudes of these forces and consequently on the landing gear behavior. As the ground measurements during taxi tests were performed on dry concrete, no effects of runway condition could be

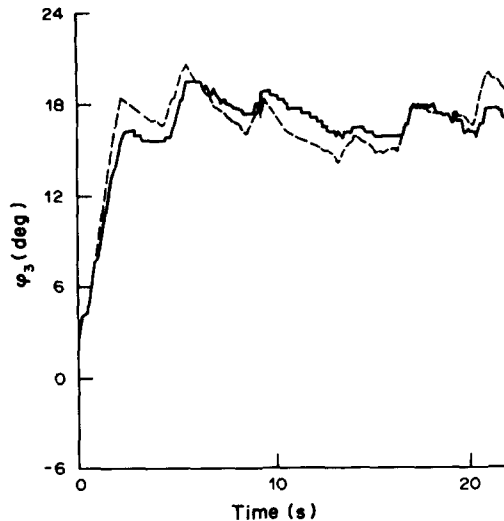


FIG. 81. Nose wheel angle during initiation of turn. ——measured; - - - computed.

determined. Therefore, relevant data from available literature<sup>(91)</sup> was incorporated in the model.

To prevent unrealistic behavior of the simulated landing gear at zero aircraft speed, so called zero-speed models were added to the brake force, the side force and the nose wheel steering models. The performance of the landing gear model is demonstrated in 'Proof of Match' time histories below.

#### 5.5.7. Evaluation and Testing of the Final Models

At the Faculty of Aerospace Engineering of DUT the moving-base visual flight simulator was used for the evaluation and testing of the a priori model and the final mathematical models of the Citation 500. The existing, modular real-time simulation software was adapted to the aircraft related Citation models. The software was optimized to minimize the required CPU-time, using common breakpoint routines in non-linear function generation.

An interactive software routine was developed for the generation of the 'Computer Generated Checkout' (CGC) and 'Proof of Match' (POM) files. This interactive routine handles the information exchange between the user and the simulation software (Fig. 82) and allows different kinds of control inputs to the engineering simulation. These control inputs may be generated using the computer keyboard or the flight simulator cockpit controls, or they may be read from a flight test (ATG) data tape. The keyboard and simulator cockpit options allow the operator to 'fly' the simulated aircraft through different

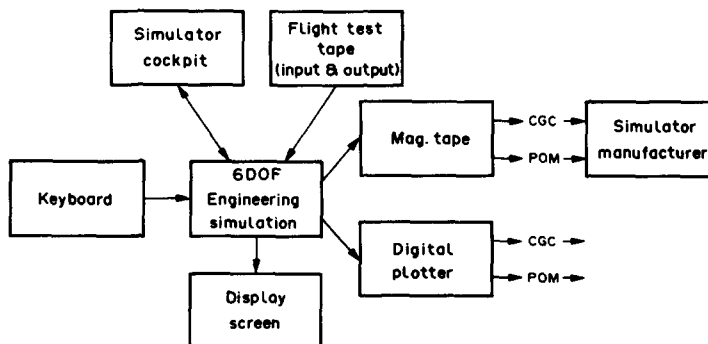


FIG. 82. Basic elements of CGC and POM-data generation.

kinds of maneuvers, such as required for the generation of CGC-files. The third option becomes essential in the generation of POM-files, where the simulation must be driven by the measured control input signals (control forces or displacements) from the actual flight test maneuver to which the simulated response must be matched. As a consequence, the generation of POM-files is always performed off-line. Examples of the off-line generation of CGC-files are the CGC of the short period motion, the phugoid and the Dutch roll. Examples of the on-line generation of CGC-files are the CGC of different stalls, normal and emergency descent and minimum unstuck speed, the latter being performed in the simulator only. The interactive subroutine turned out to be an indispensable tool in the evaluation and validation of the final mathematical model for the Citation simulation.

The Dutch Government Civil Aviation School ordered a Citation simulator with a FAA Phase II certificate. As a consequence, the mathematical model delivered by NLR and DUT must be Phase II approved. Therefore on top of the mathematical model and data package two kinds of data-files were delivered to the simulator manufacturer:

- ‘Computer Generated Checkout’ (CGC) data-files,
- ‘Proof of Match’ (POM) data-files.

The purpose of the CGC-data is to support tests, which will demonstrate that the mathematical model and data package have been correctly implemented in the computer by the simulator manufacturer. To this end a number of on-ground and in-flight checks were carried out, using the six DOF engineering simulation at DUT. The CGC-data were initially provided for the a priori mathematical model and updated later for the flight test derived model of the Citation 500.

In addition, a quantitative validation of the quasi-stationary and dynamic characteristics of the mathematical model was carried out. This resulted in the prescribed POM-data files.<sup>(66)</sup> In the POM, simulated responses are directly compared to aircraft flight traces permitting an objective examination of the fidelity of the mathematical model. For this purpose special ATG maneuvers were carried out in the flight test program.

Examples of the ‘Proof of Match’ of the different Citation 500 submodels are presented in Figs 83–90. In these figures, the admissible ‘Phase II’ tolerances, are indicated.<sup>(21)</sup> These tolerances are used in the comparison of the flight test data with the mathematical model responses, to determine whether or not a match has actually been achieved.

The purchase of a Phase II flight simulator may sometimes be hampered by an inadequate aircraft simulation model, or even by the non-existence of such a model. The execution of a flight test program and the identification of a mathematical model from flight test data may provide a solution to this problem. Such a program was carried out by NLR

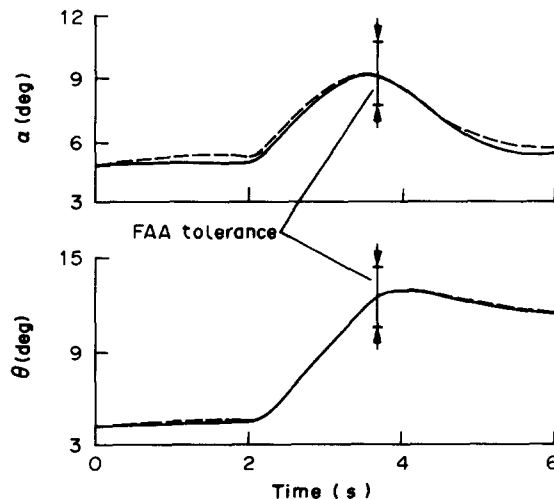


FIG. 83. Short period motion. ——measured; - - - computed.

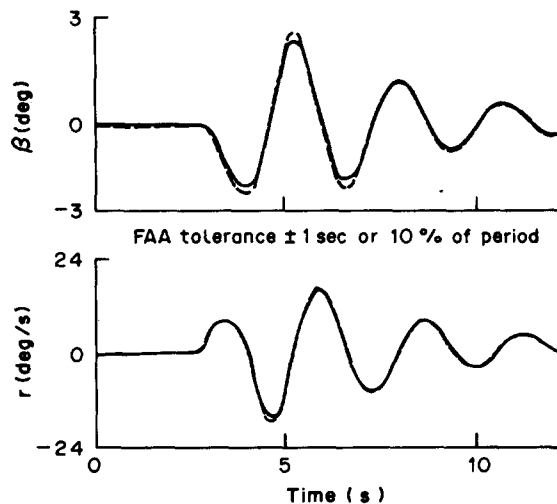


FIG. 84. Dutch roll dynamics. ——measured; - - - computed. FAA tolerance  $\pm 1$  sec or 10% of period.

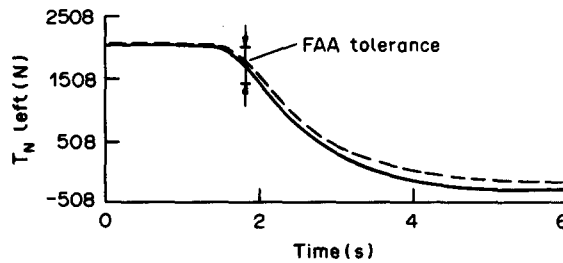


FIG. 85. Dynamic net thrust response. ——measured; - - - computed.

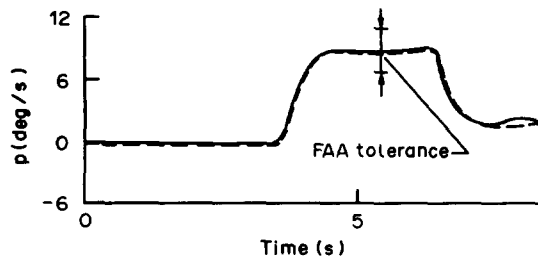


FIG. 86. Roll rate response on aileron doublet. ——measured; - - - computed.

and DUT to develop the mathematical model and data package of a Cessna Citation 500. An advanced high accuracy measurement system was used to generate a database from which the simulation model was identified, using different types of identification techniques. The development of a priori models provided a smooth transition to the flight test-derived aerodynamic, engine, flight control system and landing gear models.

A 'Proof of Match' was generated, using separate flight test maneuvers, from which it could be concluded that the identified mathematical model provided a fully satisfactory simulation of the actual airplane characteristics.

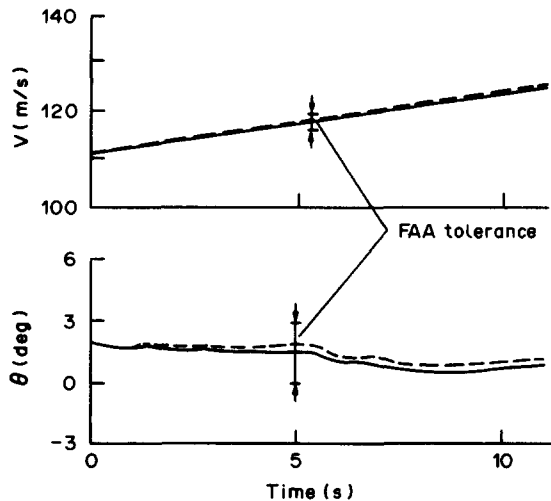


FIG. 87. Level flight acceleration. ——measured; - - - computed.

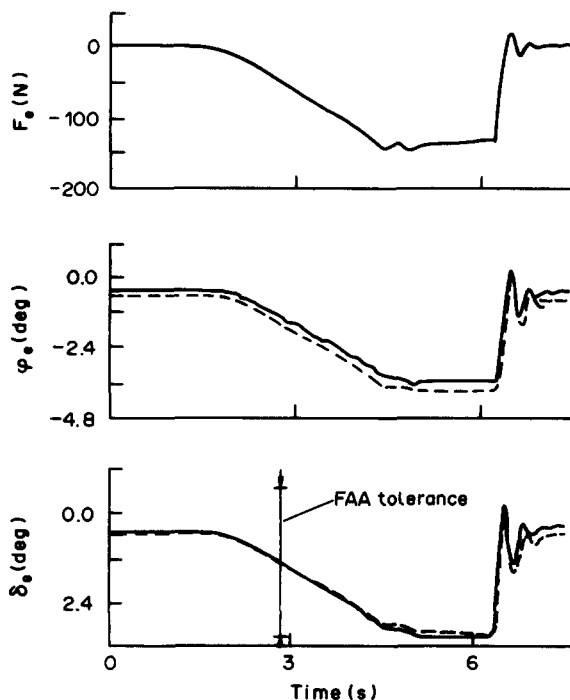


FIG. 88. Elevator release. ——measured; - - - computed.

## 6. OUT-OF-THE-WINDOW VISUAL SIMULATION

### 6.1. GENERAL

Out-of-the-window visual simulation is—as mentioned already in Section 4.4—a formidable challenge, because of the terrific performance of the human eye. The eyes are the most important senses of the human for gaining information about the world around him. Over 90% of the information he receives during normal daily activities comes through the eyes and this may be even more, when a pilot performs his tasks during flight.

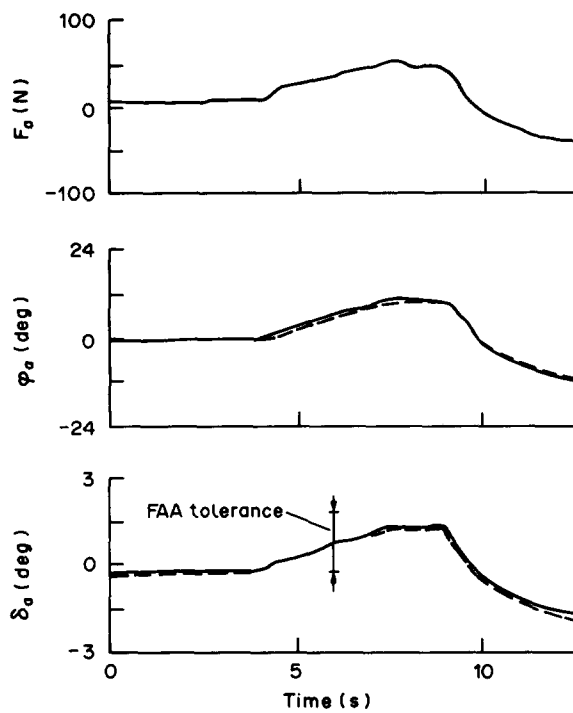


FIG. 89. Aileron wheel force, position and surface position. — measured; - - - computed.

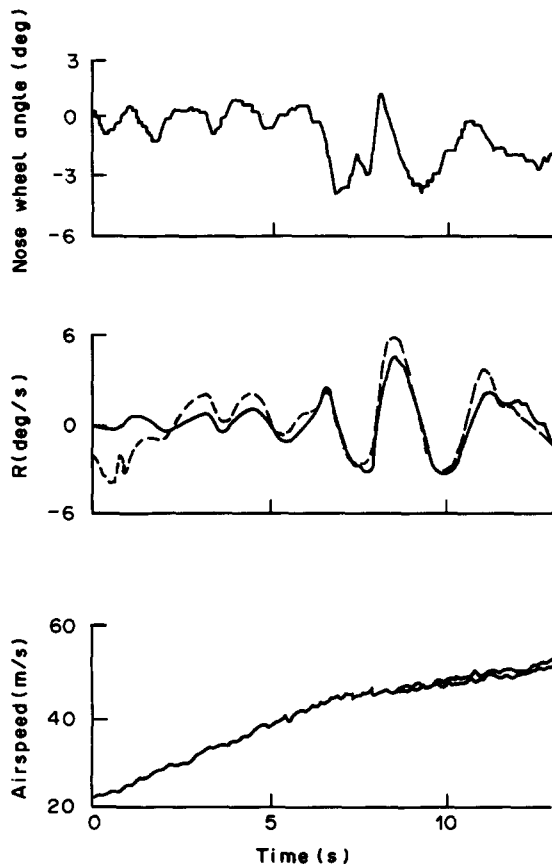


FIG. 90. Minimum control speed on ground. — measured; - - - computed.

To set the requirements of a visual simulation system to match the performance of the human eyes seems totally impractical, because a few calculations show that visual systems meeting the human eye characteristics require a performance of 10 to 100 times the performance of currently used visual simulation systems. Therefore the crew's simulated visual stimuli will be compromised, resulting in the simulation of the outside world and not in its duplication.

However, the problem is that our understanding of how the human pilot uses the visual information he perceives, is insufficient to provide clear guidelines for setting requirements and determining specifications for simulator visual systems. The successful use of out-of-the-window visual simulation systems, however, is stimulating the development of improved equipment as well as the research to provide data and insights into visual system requirements. The next section describes the properties of out-of-the-window visual simulation equipment under the following headings:

- Luminance/brightness
- Contrast
- Resolution and visual acuity
- Color
- Field of view
- Viewing region
- Depth and range effects
- Mapping factors
- Scene content
- Refresh and update rate.

## 6.2. VISUAL SIMULATION SYSTEM CHARACTERISTICS

Although defined under separate headings, the performance of a visual simulation system in each of the above areas depends upon the range and level of the other properties, which in turn are defined by the prevailing visual situation. The scene color, for example, may modify the perception of contrast in the picture. Similarly, luminance/brightness, contrast and resolution are interrelated to such an extent that they cannot be considered in isolation of each other. Below, however, a short discussion of each property from the perspective of that individual characteristic is presented.

### *Luminance/brightness*

Candela is defined<sup>(59)</sup> in terms of the amount of light emanating from a blackbody surface at the temperature of melting platinum (2042 K). Luminance is usually measured, using photometers, in candelas (cd) per unit area or foot-lamberts, where  $1 \text{ cd}/\text{ft}^2 = \pi \text{ foot-lamberts (ft-L)}$ .

The human eye can operate over an extremely wide range of luminance levels, having a variable aperture pupil to control the amount of light reaching the retina. It uses different detector cells (rods and cones) for different luminance levels and it has the ability to adapt to longer term exposure to very high or very low light intensities. The range of luminances normally encountered in real life<sup>(95)</sup> is shown in Fig. 91. Brightness is used as the perceptual correlate of luminance. It is in a logarithmic fashion related to luminance intensity.<sup>(59)</sup>

The luminance intensity of current 'day-light' visuals is in the range of  $20\text{--}30 \text{ cd}/\text{m}^2$  ( $7\text{--}10 \text{ ft-L}$ ), which is also the screen luminance level in the film industry, to depict a bright sunny day.

### *Contrast*

In order to describe the difference between the brightness of a scene element and its immediate background, the word 'contrast' is used. In order to visually perceive an object as

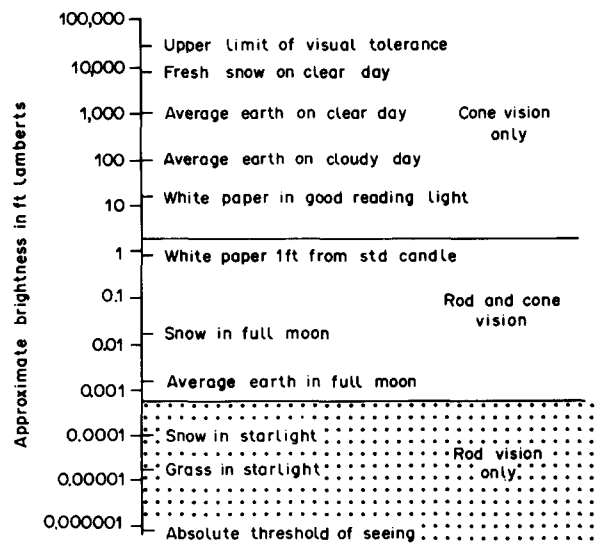


FIG. 91. Examples of various levels of luminance.

distinct from its background, it must have some contrast, either in the form of a luminance difference or a color difference. A high-contrast picture is not necessarily better than a low-contrast picture and may actually contain less detail. Most observers prefer a high-contrast picture.

The intelligent use of contrast in a visual simulation system may provide visual cues for depth perception, target acquisition and environmental conditions.<sup>(59)</sup>

#### *Resolution and visual acuity*

One of the most important characteristics of a visual system is resolution. A general definition of the resolution of a visual system is its ability to present small, recognizable scene details. The ability of the human eye to recognize fine detail is called 'visual acuity'. Different types of visual acuity are:<sup>(59)</sup>

- Minimum separable acuity, which is the smallest distance between two objects that allows them to be recognized as separate rather than as a single unitary object. Medical eye testing charts measure this type of visual acuity and it is the most useful metric to examine the quality of images and the information they provide.
- Minimum perceptible acuity refers to the ability of the human eye to detect 'the smallest object' in a large field of view.
- Vernier acuity is the accuracy with which two objects, such as two straight lines, can be aligned (to within 5 arc sec for an average eye).
- Stereoscopic acuity is the ability of the human observer to perceive depth in a scene due to the separation of the eyes.
- One further type of acuity is the ability of the eye to detect motion. The slowest motion the human eye is able to detect is about 1–2 arc min/sec.<sup>(98)</sup>

Visual acuity interacts with both luminance level and contrast. Figure 92 shows that visual acuity increases in a fairly linear way with increasing luminance, but tailing off at both ends of the luminance scale. Reducing the object contrast also reduces the visual acuity of the human eye (Fig. 93). The relationships between resolution, contrast and luminance is shown in Fig. 94, in the form of a three-dimensional surface of their interactive effects on perceptual performance. It is apparent from this figure that contrast has a much greater effect on usable resolution than luminance. Lower than real-world luminance levels may be compensated by higher than real-world contrast ratios in order to provide a specific spatial resolution.

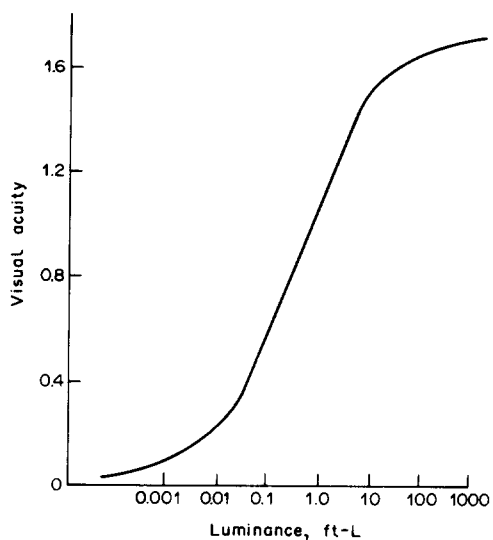


FIG. 92. Variation in V.A. with object luminance.

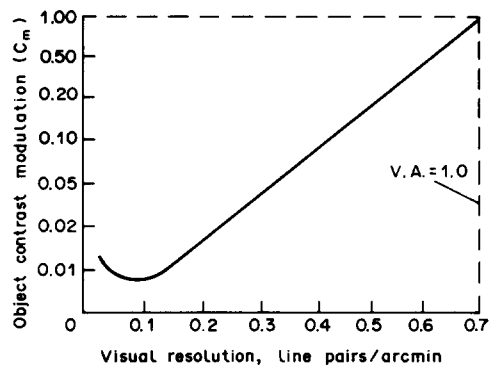


FIG. 93. Object contrast modulation, necessary for an eye to resolve a pattern of alternating dark and bright bars of equal width.

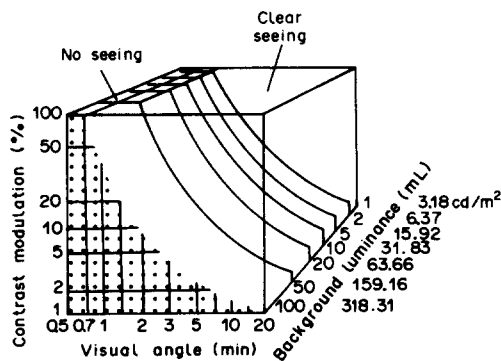


FIG. 94. This curved three-dimensional surface shows the relationship between visual angle, contrast, and background brightness. When a combination of these factors falls on a point below the curve, we cannot discriminate; a combination falling on a point above permits easy seeing.

### Color

The normal human eye is stimulated by electromagnetic radiation in the range of wavelengths of light from 400–700 nm, known as the visible spectrum. The visual sensation produced by this spectrum corresponds to the perceived colors from violet through blue to

green, yellow and red. Figure 95 shows that maximum sensitivity is in the green-yellow region (550 nm), although the three types of cone receptors in the retina<sup>(94)</sup> are individually most sensitive to blue (445 nm), green (535 nm) and red (570 nm). A mixture of light across the total visible spectrum causes a sensation of no color at all, which is called white light. Objects reflecting or transmitting white light as a function of wavelength are colored, the dominant color being the reflected or transmitted light.

In a visual system the mixing of three primary colors, usually red, green and blue, generates the color in the scene. As an example, the chromaticity chart<sup>(59)</sup> of some Cathode Ray Tubes (CRT) is shown in Fig. 96. In a chromaticity chart, the *y* values of all possible colors along the vertical axis are plotted against the *x* values of the same colors along the horizontal axis. The chromaticity coordinates, *x* and *y*, define a point on the chromaticity chart inside the locus of the pure spectral colors. For example, *x* = 0.313 and *y* = 0.329, define point *D* in Fig. 96, which is white. If a line is drawn from *D* through *P* to meet the locus of the spectral color at *Q*, the dominant wavelength will be given by *Q* and the color purity by *DP/QD*. All colors within the color triangle *B* (blue), *G* (green), *R* (red) in Fig. 96, can be generated using a suitable mixture of the primary colors. When viewed through infinity optics (see Section 4.4) this triangle will be shifted due to the spectral transmission of the optics and may vary as a function of viewing angle.

As for resolution, the perception of color cannot be considered in isolation. It interacts with luminance, contrast and visual acuity in a complex manner.

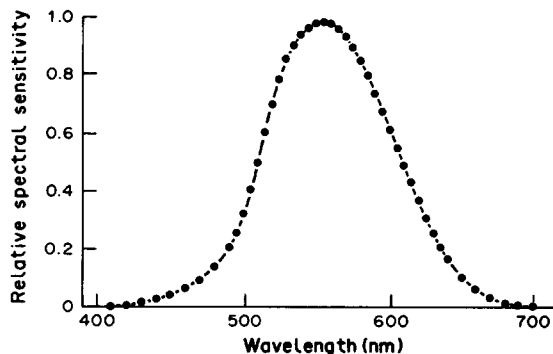


FIG. 95. A foveal spectral sensitivity function for a normal observer.

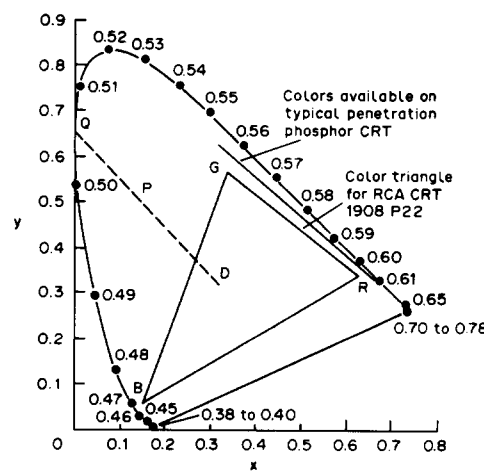


FIG. 96. Chromaticity chart; wavelengths along the spectral line are in microns.

### *Field of view*

Field of view describes the extent or coverage of a visual system. It produces a scene within the field-of-view boundary, which can be considered as a simple window, and generally darkness is evident outside the field-of-view.

The angular dimensions of the field of view of a flight simulator visual system can range from a few degrees to angles equivalent to the limits of human vision (see Section 4.4). Commercial airline simulator-type display units (Fig. 29) produce scenes having field boundaries that cover angles of, at most, about  $50^\circ$  horizontally and  $35^\circ$  vertically. This field size is approximately 4% of full field.<sup>(59)</sup> As far as the human eye is concerned, the maximum resolution capability is centered around the fovea, a retinal area aligned with the eye's optical axis and covering about  $2^\circ$  in the centre of the field of view. Outside this area the resolution/visual acuity progressively decreases (Fig. 97). The use of almost unlimited eye, head and body movements, however, allows the high resolution foveal area to be brought to bear on any region of visual space around the human observer.

### *Viewing region*

The limitation of all visual simulation systems is that they can produce good imagery only when viewed from within a specific region of space. The so-called 'viewing region' is the region of space wherein an acceptable simulated image is received by the human eye. Outside the boundary of the viewing region, the simulated image disappears or its quality becomes unacceptable. This effect is due simply to the geometrical relationship between the optical elements and the viewing point. In Section 4.4 the viewing region of a spherical mirror beam-splitter display unit is indicated in Fig. 29. In the case of a 'WIDE' visual display (Fig. 30) the viewing region is substantially larger, providing each cockpit crew member with an almost undistorted outside view.

### *Depth and range effects*

The property of human vision which results in perceiving images of an accurate three-dimensional rather than a flat outside world is depth perception. Many mechanisms are involved in the perception of depth but they cannot all be simulated effectively. These mechanisms can be separated into two groups: those associated with binocular vision and those associated with monocular vision (one eye only).

Fortunately there are quite a number of depth and range cues which do not require both eyes. Examples of these monocular effects are:

- Size constancy, which cue is based on the constant size of real world objects and so retinal image size relates to object distance, providing strong depth information.

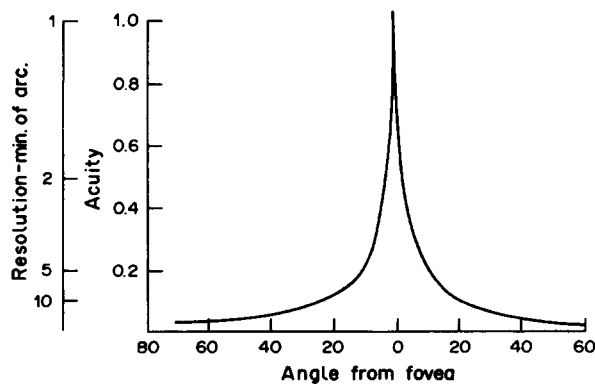


FIG. 97. Lateral resolution of the eye.

- Motion parallax, which describes a change in relative position of objects due to either observer or object motion.
- Linear perspective, which cue is based on the perspective transformation leading to the geometrical aspect of a vanishing point (perceived convergence of parallel lines with increasing distance).
- Interposition or masking of objects, which arises when a closer object overlaps another, being at a greater distance from the observer.
- Aerial perspective, which is the loss in contrast due to atmospheric conditions, like haze or fog, at increasing distance from an observer.
- Shadows, which are important depth cues giving a strong impression of the three-dimensionality of objects as well.

For an observer using both eyes, the viewing point of each eye is different and consequently the corresponding retinal images are also slightly different, forming the impression of depth. This is called binocular disparity which results in the most accurate mechanism of depth perception, the stereopsis.<sup>(97)</sup> Convergence is a further binocular cue of range, which is produced by the slight 'toeing-in' of the eyes when looking at a near object.

Most visual simulation systems provide only monocular cues. They enjoy a level of success, implying that binocular depth and range effects are not very important for most flying tasks.

#### *Mapping factors*

Mapping is the term which describes the position of an object within the field of view, using angular measures. For example, a runway threshold light may be truly located 30° in right azimuth and 20° negative (down) elevation from the longitudinal body axis reference of a landing airplane. Due to CRT or optical imperfections, however, the light appears displaced from the above coordinates in the simulated scene. This 'remapping' of the simulated scene causes the scene to appear distorted which may also introduce anomalous movements in dynamic conditions.

#### *Scene content*

Scene content is the amount of detail which can be included in a generated image. The content of a visual image may be quantified in terms of 'luminance transition'.<sup>(96)</sup> Even the most expensive CGI systems (see Section 4.4) have limits on the number of luminance transitions which they can deal with. This reduces the realism of the scene and many of the depth and range effects, described above.

#### *Refresh and update rate*

Television-based visual systems must generate and display a new picture at a sufficiently high rate, in order to create the illusion of smooth continuous motion. One of the effects of generating moving pictures using TV-based systems is the creation of a perceptible 'flicker' of the picture luminance, if the refresh rate is below a certain frequency. In raster scan systems refresh rate is the same as field rate, so for an interlaced picture,<sup>(59)</sup> the frame rate is half the refresh rate. In calligraphic systems the refresh rate is used to describe the number of complete pictures drawn each second. The 'flicker suppression refresh rate' is the refresh rate at which flicker is just imperceptible. It depends on the type of phosphor used in the display and varies between 25 and 60 Hz.

The update rate is, in contrast to the refresh rate, the generation frame rate or the frequency at which a complete new image is generated. Using a faster update rate results in improved image quality of dynamic scenes. For example, a raster-scan, digital-computer generated image system having refresh and update rates of 60 Hz, will produce minimum

anomalies in its pictures. Reducing the update rate to 30 Hz, however, results in increasing picture anomalies depending on the scene dynamics.

The visual system is often the most expensive component of a flight simulator. The constraints which limit the use of simulators to particular tasks, often lie in the performance of the visual system. Therefore the appearance of 'low cost' visual systems<sup>(93)</sup> is of great advantage for two reasons. Firstly, a low cost visual reduces the total cost of a flight simulator by a significant amount. Secondly, more visual capability can be bought for the same investment, thereby reducing visual performance constraints.

Medium cost visual systems, like Singer Link's 'Image 3' and Rediffusion's 'SPX' (\$ 1-2 million in 1989 prices) now show some of the high cost features such as modularity, cell texturing, large number of polygons per second etc. The significant breakthrough, however, occurred as graphic work-stations, initially intended for other users, achieved 'real-time' image generation performance. Today, visual simulation systems are available over a large price spectrum. As performance is clearly related to price, the challenge remains to match the requirements, available budget and visual performance.

## 7. MOTION CUE GENERATION

### 7.1. GENERAL

The generation of motion cues in flight simulation is based on (Fig. 98):

- (1) The motion system hardware and in particular its dynamic characteristics, see Section 7.2.
- (2) The motion drive software, controlling simulator cockpit motion and as a matter of fact, in combination with the hardware, generating the 'motion cues'.

Before starting to elaborate on the generation of motion cues, it seems appropriate to present a definition of a 'cue' and to specify what types of cues are important in flight and flight simulation. A definition of a cue may read: "A cue is a cluster of sensory stimuli—acting on the pilot via any of his sensory channels—closely correlated with a characteristic of the airplane and its behavior, which is relevant to the pilot when flying the airplane" (in Webster's Dictionary, a cue is defined as "a feature indicating the nature of something perceived").

Relevant types of cues in flight and flight simulation may be distinguished, according to Section 4.3, as follows:

- (1) Environmental cues, which may be subdivided into:
  - (a) Alerting cues, due to the initial effects of disturbance motions, like the airplane's response to turbulence, runway rumble, engine failure etc.

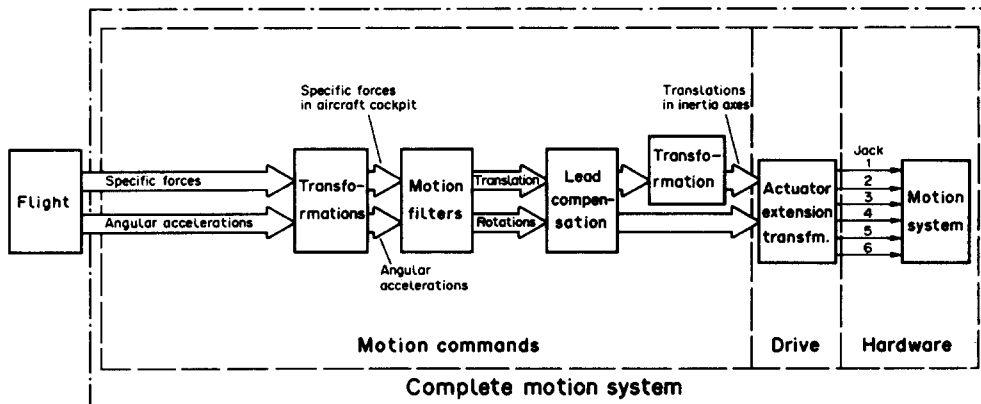


FIG. 98. Basic elements of motion cue generation.

- (b) On-set cues, due to the initial effects of pilot-generated motions immediately after the start of a 'flight' maneuver.
  - (c) Sustained cues, due to prolonged or quasi-static effects of both disturbance motions and pilot-generated motions.
  - (d) Transient cues,<sup>(99)</sup> covering the time-span between on-set ( $t = 0^+$ ) and sustained cues ( $t = \text{large}$ ).
- (2) Equipment cues, which confirm to the pilot that he is in actual flight and motivate him to behave accordingly. It may well be, that the transient, sustained and equipment cues all fulfill a similar function. Together these cues might be called 'confidence cues'.

False cues occur in piloted flight simulation only. They are clusters of sensory stimuli resembling any of the above cues, but they are *not correlated* with the corresponding aspects of the airplane's characteristics. The *absence of a cue*, expected by the pilot on the basis of his internal model<sup>(104)</sup> of the airplane's characteristics, is also considered a false cue.

Section 7.3 describes the generation of drive commands controlling simulator cockpit motion. Section 8.5 presents the so-called 'flight simulator critical maneuvers', which are used to compare motion cues in the actual aircraft cockpit to those in the simulator cockpit.

## 7.2. DYNAMIC CHARACTERISTICS OF THE MOTION SYSTEM HARDWARE

High fidelity six degrees-of-freedom (6 DOF) motion cues are generated using a balanced combination of motion system hardware and motion drive software (Fig. 98). Before this software can be optimized to control a specific motion system, the dynamic characteristics of the hardware should be measured and documented in detail. A systematic and uniform method to do this has been published by AGARD in 1979,<sup>(55)</sup> and is briefly summarized below.

The motion system characteristics recommended to be measured are:

- Excursion limits for single degree of freedom operation.
- Describing functions (Bode plots) for each degree of freedom for the uncompensated as well as for the lead-compensated motion system, see Section 7.3.
- Linearity and acceleration noise.<sup>(20)</sup>
- Hysteresis.
- Dynamic threshold (output acceleration time-delays).<sup>(54)</sup>

The above measurements are performed, using standardized sinusoidal and step input signals, respectively. For a hydraulic motion system with hydrostatic bearings, correctly compensated for dynamic lag, a bandwidth of 6 Hz (phase-lag less than 45°), an acceleration noise level of 0.01  $g$  and a dynamic threshold of less than 50 msec can be obtained in each degree of freedom.

A software package which performs the measurements according to Ref. 55, has been developed for the DUT 3 DOF and for 6 DOF motion systems, on the Gould SEL 32/87 computer. The program generates the standardized input signal which, after digital to analogue conversion, drives the motion system in one of its degrees of freedom (Fig. 99). Accelerometer outputs, measuring the motion system response, are filtered by analogue presampling filters (in order to prevent a.o. aliasing) before analogue to digital conversion and response analysis. Forcing function update and motion system response sampling are carefully synchronized by using the same clock-pulse.

The following figures present a few examples of the complete DUT motion system performance measurements.

Figure 100 shows two examples of measured heave acceleration response:

- At 0.1 Hz with the input acceleration amplitude (ANOM) at 0.1 m/sec<sup>2</sup> ( $\approx 0.01 g$ , which is about the threshold of perception).
- At 1.0 Hz with ANOM = 3 m/sec<sup>2</sup>.

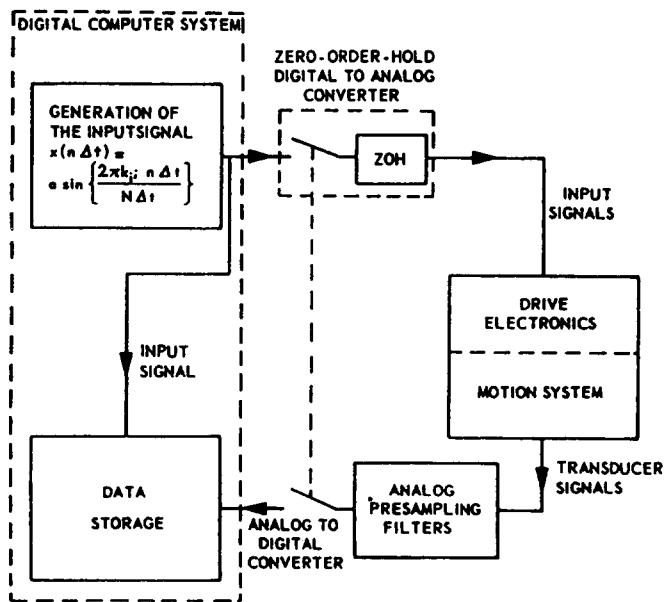


FIG. 99. Signal generation and datalogging.

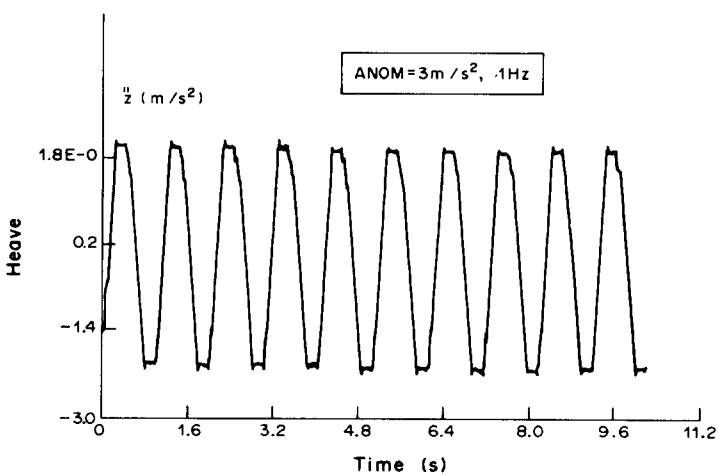
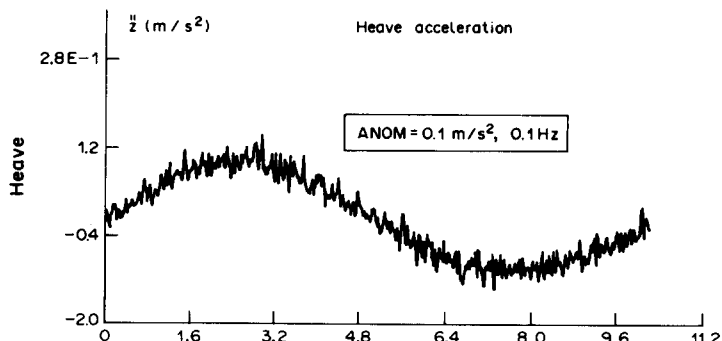


FIG. 100. Reconstructed time histories of heave acceleration.

The latter heave acceleration response clearly shows the deformation of the input sinusoid, due to the system limits (maximum output acceleration is  $2.22 \text{ m/sec}^2$ ). The corresponding power spectra are presented in Fig. 101. Heave acceleration noise and parasitic pitch angular accelerations are shown in the Figs 102 and 103 for both cases, respectively.

Apart from these plots, the software package also generates a rather complete print-out, featuring the following items:

- Gain and time-constants of the pre-sampling filters.
- Standard deviations of the fundamental frequency, the acceleration noise and the parasitic accelerations.
- Peak accelerations in each degree of freedom.
- Amplitude-ratio and phase-shift of the describing function.
- Peak ratio, noise ratio<sup>(55)</sup> and nominal versus actual accelerations, velocities and displacements in the driven degree of freedom.

The software package can also be applied to identify the dynamic characteristics of the complete motion system, including the motion filters (see Fig. 98 and Section 7.3). In this way, the frequency range for 'high fidelity motion',<sup>(101)</sup> where phase distortion should be less than 20 degrees (either lead or lag), can be determined.

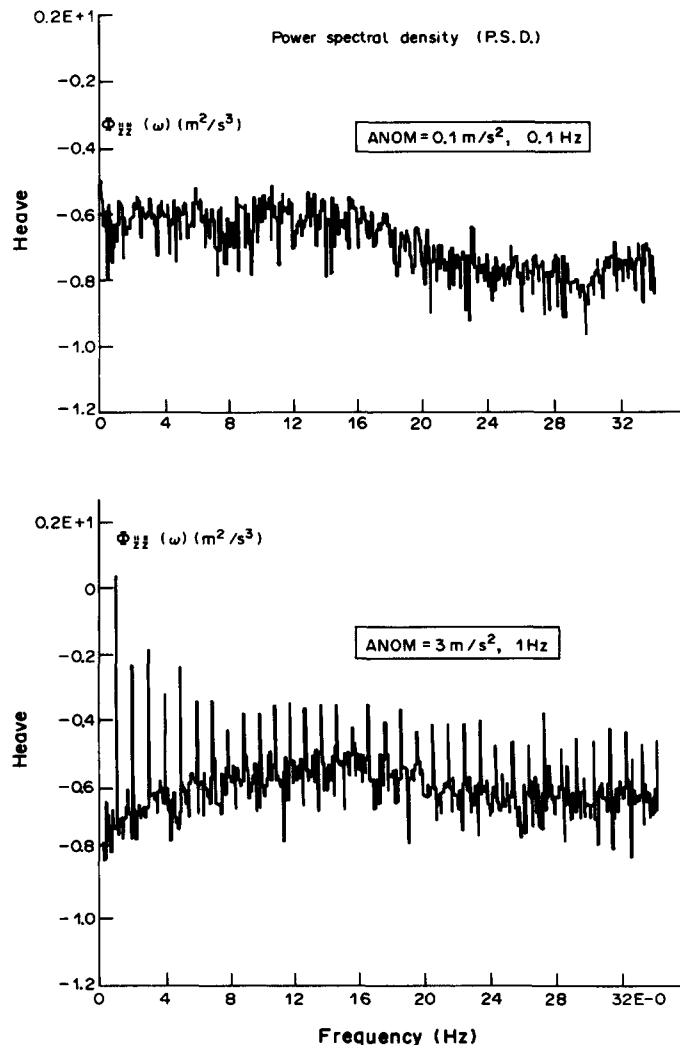


FIG. 101. Heave acceleration power spectra, sinusoidal heave inputs.

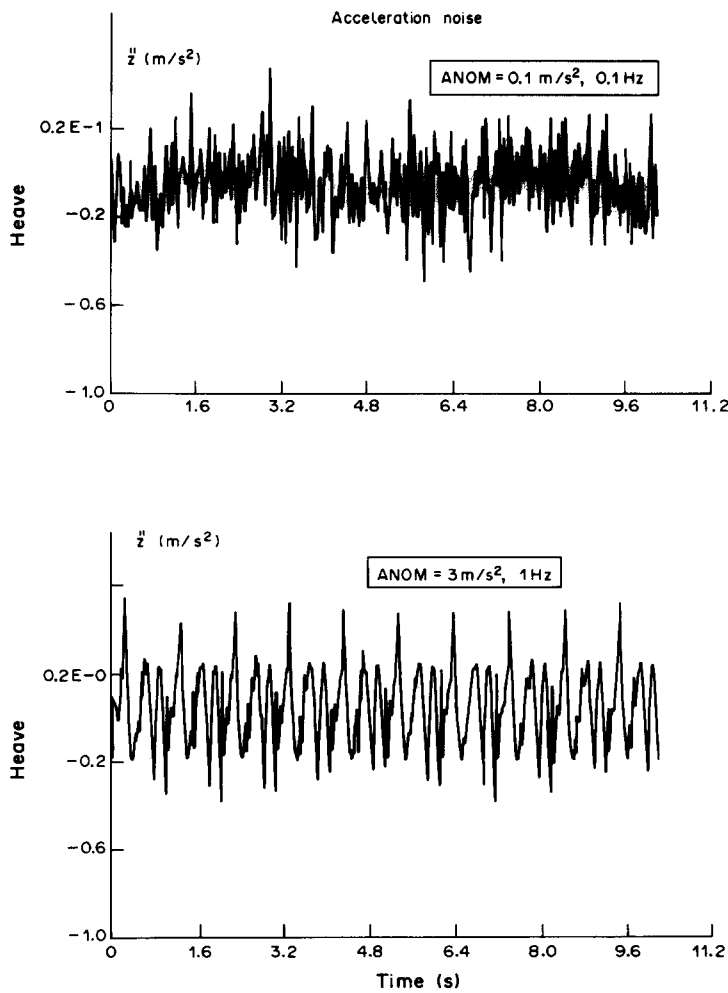


FIG. 102. Reconstructed time histories of heave acceleration noise.

### 7.3. MOTION DRIVE COMMANDS CONTROLLING SIMULATOR COCKPIT MOTION

The generation of adequate motion cues in a limited space is based on the characteristics of the non-visual sensors, in particular the semi-circular canals and the otoliths, see Section 4.5. They only function as adequate transducers of angular acceleration and specific force, respectively, over a limited frequency range. Therefore, simulator-cockpit motion needs to match aircraft-cockpit motion only within this range. In particular, the low-frequency characteristics of the semi-circular canals and the otoliths, below about 0.1 Hz,<sup>(54)</sup> make it possible to 'wash out' motion platform tilt and linear acceleration, respectively, by slowly returning the platform to its neutral position, without allowing the pilot to detect this motion disparity. The efficiency of so-called washout algorithms (motion filters) depends on the effective thresholds<sup>(105)</sup> of the semi-circular canals and otoliths and their respective responses to different combinations of accelerations and velocities. The use of vestibular models<sup>(102)</sup> to match simulator-cockpit motion to aircraft-cockpit motion is a well-known approach.

Sustained linear acceleration cannot be achieved in a limited motion simulator. But the graviceptors, including the otoliths, being sensitive to specific force rather than to kinematic acceleration, are incapable of distinguishing between linear acceleration and gravitational acceleration with respect to inertial space. Therefore steady pitch and roll attitude (tilt) of the motion platform is used as a substitute for linear acceleration. Care should be taken, however, that the rate of pitch or roll, used in performing the 'g-tilt', be such as to avoid the

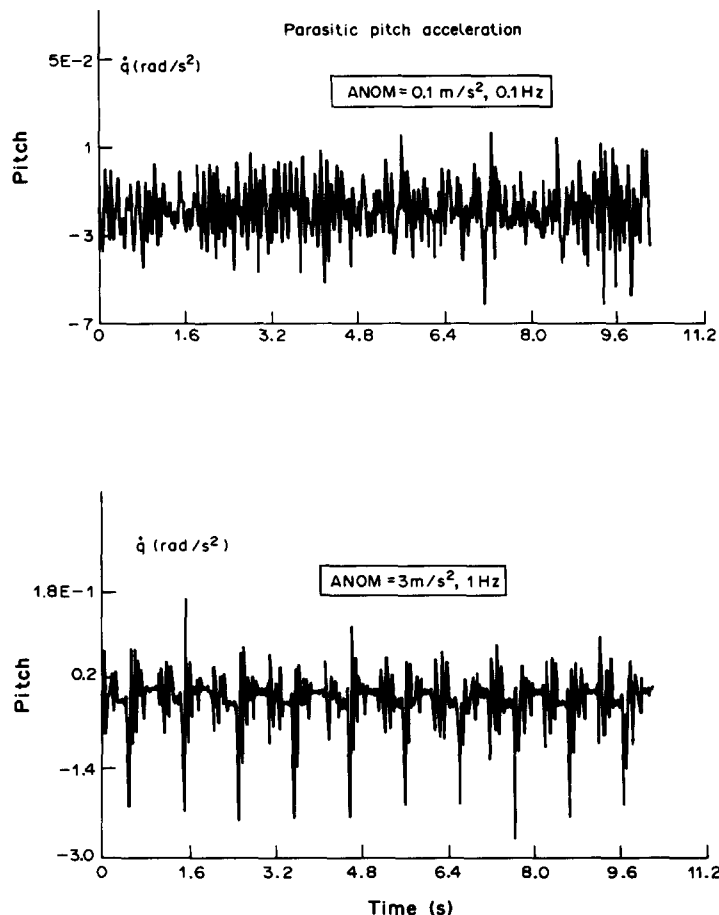


FIG. 103. Reconstructed time histories of parasitic pitch acceleration, due to sinusoidal heave input.

generation of inadvertent false (rotation) cues. By rolling or pitching at slightly superthreshold rates to tilt angles less than ideally required, compromises are achieved to minimize the generation of false cues. Visually induced motion sensations using peripheral vision<sup>(106)</sup> may be a partial substitute for non-visual motion cues.

Over the past 20 years several types of motion drive algorithms have been developed.<sup>(109)</sup> The most common forms of these algorithms are:

- Linear second-order high and low-pass filters, applied in airline flight simulators.<sup>(100)</sup>
- Coordinated adaptive washout, applied in some research simulators.<sup>(107)</sup>
- The optimal control approach, applied a.o. to the Vertical Motion Simulator (VMS), at NASA Ames,<sup>(102)</sup> see Section 3.3.
- The higher-order filter approach, applied at DUT.

As an example, the motion drive algorithms applied at DUT to drive synergistic 6 DOF motion systems, are briefly described below. These algorithms use first- and second-order linear filters, supplemented by non-linear elements, depending on the system excursion limits and the simulator task. The block diagram of Fig. 104 presents an overview of the basic operations performed by the motion drive algorithms.

The specific forces ( $A_{x_b}$ ,  $A_{y_b}$ ,  $A_{z_b}$ ) and the angular accelerations ( $\dot{p}$ ,  $\dot{q}$ ,  $\dot{r}$ ), computed by the real-time simulation software (FLIGHT, see Section 4.2) in the body axes reference frame, are the basic inputs to the motion drive algorithms.

The *centroid transformation*<sup>(108)</sup> transforms the specific forces from the airplane c.g. to the centroid location of the motion platform (resulting in  $A_{x_c}$ ,  $A_{y_c}$ ,  $A_{z_c}$ ), providing for

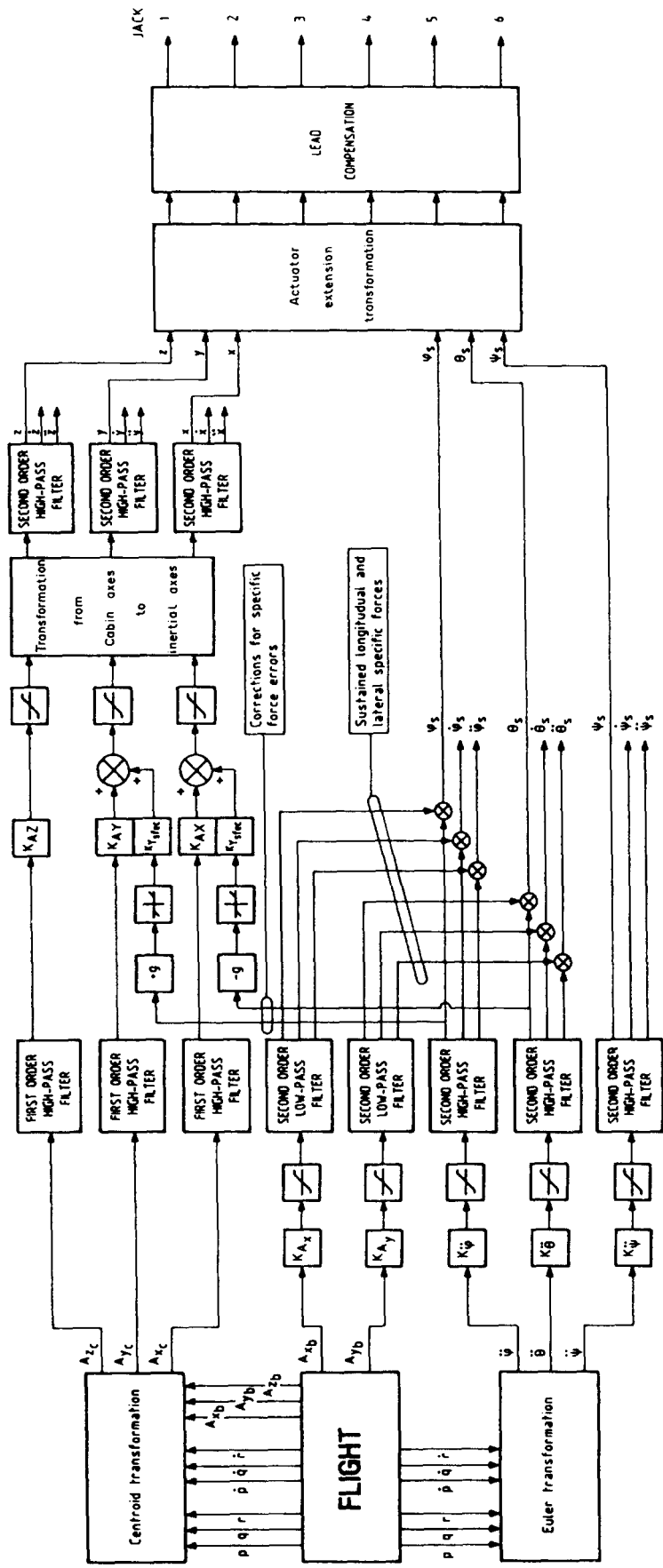


FIG. 104. Basic operations in DUT motion drive algorithms.

additional normal and lateral specific forces due to airplane pitch and yaw accelerations, respectively.

The *Euler transformation* transforms the airplane's angular accelerations to inertial axes, resulting in the Euler angular accelerations ( $\ddot{\phi}$ ,  $\ddot{\theta}$ ,  $\ddot{\psi}$ ). These angular accelerations are attenuated, limited and high-pass filtered, to generate the alerting and on-set angular motion cues.

The specific force errors (false cues), generated as a result of the simulation of the above roll and pitch accelerations, are corrected using lateral and longitudinal motion platform linear accelerations, respectively, see below. In this way the specific force error, in e.g. coordinated turns, is kept below the pilot's perception.

In order to simulate the sustained part of the longitudinal ( $A_x$ ) and lateral ( $A_y$ ) specific forces, using motion platform tilt, these specific forces are attenuated, limited and low-pass filtered. The motion platform tilt angles ( $\theta$  and  $\varphi$ ), generated in this way, are added to the platform roll and pitch angles resulting from the generation of the alerting and on-set angular motion cues above (Fig. 104).

Accelerating the motion platform linearly in the appropriate direction, generates the high-frequency parts of the specific forces  $A_x$ ,  $A_y$  and  $A_z$  at centroid location. At least a third-order high-pass filter should be applied to these signals, in order to warrant that the motion platform returns to its neutral position after some time, even in the case of a (prolonged) sustained specific force input (e.g. during take-off). The three third-order high-pass filters, used to filter  $A_{x_c}$ ,  $A_{y_c}$  and  $A_{z_c}$ , are divided into first- and second-order high-pass filters (Fig. 104). After first-order high-pass filtering, the longitudinal and lateral specific forces are added to the corrections for the longitudinal and lateral specific force errors, respectively, resulting from the generation of the alerting and on-set angular motion cues.

Now, the resulting specific forces are limited, transformed to inertial axes, and filtered, using second-order high-pass filters. These high-pass filter outputs generate the alerting and on-set longitudinal and lateral linear motion cues and also the longitudinal and lateral specific force error corrections (sfec), respectively. The specific force along the Z body axis is, after first-order high-pass filtering, also transformed to inertial axes and filtered, using a second-order high-pass filter as well. This high-pass filter output generates the heave alerting and on-set motion cue.

The *actuator extension transformation*<sup>(103)</sup> calculates the length of each of the six motion system hydraulic jacks. *Lead compensation* is required to compensate for motion hardware dynamic lag. It is achieved by adding first- and second-order lead terms to the position signal of each hydraulic jack.

Provisions are being made that specific forces and angular accelerations result in platform displacements only, if they are above the effective threshold levels of the pilot's perception.

The DUT motion simulation software, described above, has been installed a.o. in the P3C ORION flight simulator of the Royal Netherlands Navy in 1987. As an illustration of the above, the performance of the motion simulation software is shown in Fig. 105 for an accelerate-stop and in Fig. 106 for a side-step maneuver of a passenger transport. In Fig. 105a, the longitudinal specific force in the aircraft-cockpit (MAXBC) and in the simulator-cockpit (MAXSIM) are presented. Figure 105b shows the corresponding pitch acceleration (MQDSIM) of the simulator-cockpit, to obtain the motion platform tilt for the simulation of the sustained longitudinal specific force.

Figure 106b presents the roll accelerations in the airplane (VPD) and in the simulator (MPDSIM), being nicely in phase during the side-step maneuver. The lateral specific forces in the airplane (MAYBC) and in the simulator-cockpit (MAYSIM) are shown in Fig. 106a, showing a specific force error of less than 2.5 ft/sec<sup>2</sup>.

Time delays for the alerting and on-set motion cues, generated by the above algorithms, are kept below 80 msec by using a 30 Hz computer update rate and a high-bandwidth, lead-compensated hydrostatic motion system. The motion software can be easily optimized for any motion system and/or simulation task and it runs on the simulator host computer (Subroutine MOtion Drive Laws, MODL, see Section 4.2).

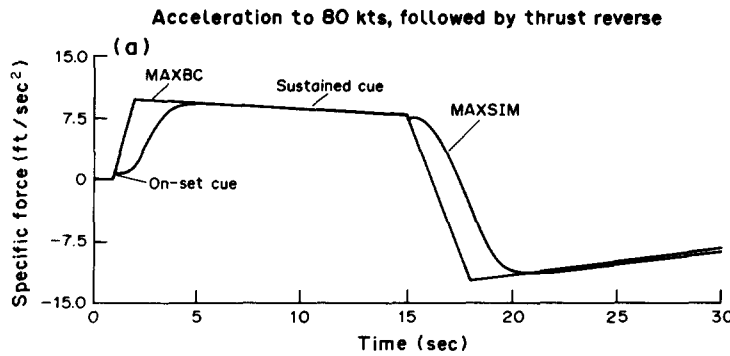


FIG. 105a. Comparison of the longitudinal specific forces in the aircraft-cockpit (MAXBC) and in the simulator-cockpit (MAXSIM), during an aborted take-off.

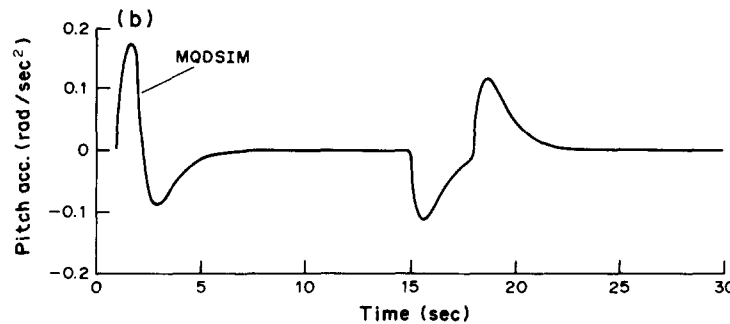


FIG. 105b. Pitch angular acceleration in the simulator-cockpit (false cue) needed to generate the sustained longitudinal specific force (MAXSIM) in Fig. 105a.

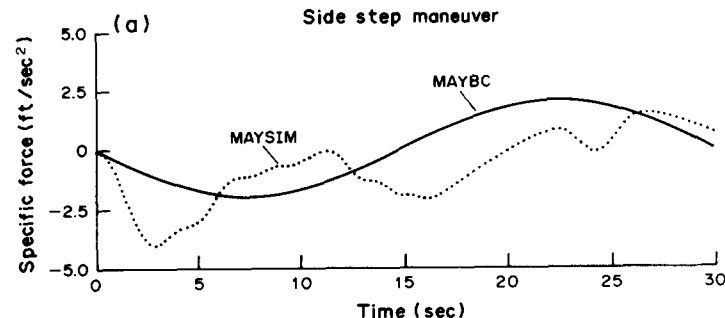


FIG. 106a. Comparison of the lateral specific forces in the aircraft-cockpit (MAYBC) and in the simulator-cockpit (MAYSIM), during a side-step maneuver.

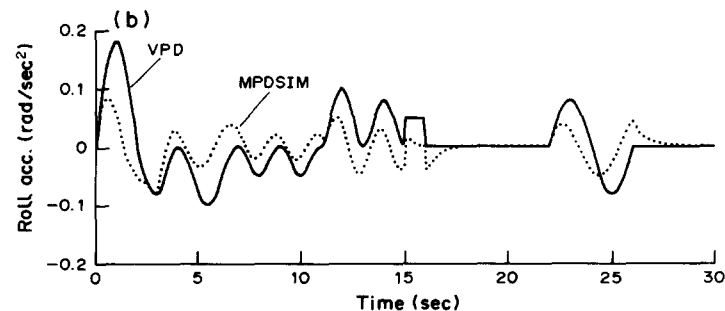


FIG. 106b. Comparison of the roll accelerations in the aircraft-cockpit (VPD) with those in the simulator-cockpit (MPDSIM), during a side-step maneuver.

#### 7.4. SPECIAL MOTION EFFECTS

The motion simulation software, described above, only computes motion cues on the basis of the specific forces and angular accelerations, available in the flight simulation software (Section 5.2.2). However, some of the motion cues, experienced in the real airplane, are *not* programmed in the flight simulation software and so they are not available as inputs to the motion software.

Examples of these special motion effects, some of which have a more or less stochastic character, are:

- Vibrations due to taxiing and take-off/landing roll.
- Motion due to runway roughness.
- Tyre, landing gear failure dynamics.
- Engine vibrations.
- Buffet due to stall-onset, stall and recovery.
- Buffet due to flap and landing gear extension/retraction.

In order to provide these special motion effects in the flight simulator, they are added to the motion drive algorithms, discussed in the previous section. Computation of the special motion effects occurs as simple functions of airplane/flight conditions, such as airspeed, angle of attack, engine r.p.m., flap and landing gear position, etc. Oscillations, computed in this way, are realistic to the degree that amplitude as well as frequency are correctly simulated, using the six motion system hydraulic jacks. The special motion effects should be carefully correlated with the sounds, reproduced by the sound simulation system in the simulator-cockpit (see Section 4.3).

### 8. FLIGHT SIMULATOR INTEGRATION, TESTING AND ACCEPTANCE

#### 8.1. GENERAL

The complexity of a 'full flight simulator', either for training or research and development, is obvious from the elaborations in the previous chapters. Figure 21, which presented a block diagram of software and hardware modules for piloted flight simulation, already showed an overview of this complexity.

In the following discussion the integration of the individual modules, as shown in this block diagram and resulting in a complete operative flight simulator, is described.

Section 4 discussed the main components of a piloted flight simulator. Before integration, these components are initially tested on a stand-alone basis. From the discussions in Section 4.2, it is obvious that the real-time digital computer forms the 'brain' of the entire simulation. So individual testing of the simulator components starts by establishing a functioning computer, which controls all remaining flight simulator components. Next the modular, real-time simulation software is implemented in the digital computer and each software module, e.g. the aerodynamic forces and moments acting on the airplane (FAIR4, Section 4.2), is individually tested. Linking all the individual software modules and the corresponding data-files results in one or more 'Load Modules' (LM), running in real-time as high-priority (foreground) tasks on the digital computer. Testing of the integrated simulation software may now start, using the so-called 'Computer Generated Checkout' (CGC) and 'Proof of Match' (POM), see below.

Simultaneously with the simulation software testing above, stand-alone testing of the remaining flight simulator components may be carried out, starting with the individual components, accommodated in the flight simulator cockpit (see Section 4.3). The flight instruments, either electromechanical or electronic (EFIS) often consist of flight hardware. This should be tested according to the instructions of the manufacturers, probably in the same manner as the flight hardware used in the real airplane. From the control loading systems, the basic control forces and displacements (Section 4.3) can be tested stand-alone by measuring force versus position in accordance with the basic airplane control system

characteristics in a particular airplane/flight condition. From the sound simulation system, the frequency and amplitude of the sound generator/speaker(s) combination is calibrated and optimized for speaker position(s) in the simulator cockpit.

The out-of-the-window visual simulation system can be tested stand-alone with the display CRT(s) or projector(s) separated from the infinity optics (see Section 4.4). The combination of image generator and display device should be optimized, using the visual simulation system characteristics as described in Section 6.2. In the case of a computer generated image (CGI), the image generator is tested for scene content and update rate. The display CRT or projector, connected to the image generator, is adjusted for luminance/brightness, contrast, resolution and color. The display optics and the display device should be carefully aligned on the simulator cockpit, starting from the pilot's nominal eyepoint, using a theodolite and airplane reference eyepoint data.

Cockpit motion generation systems are tested stand-alone, using the procedure described in Section 7.2. Before integration of the motion system hardware, the hydraulic actuators are tuned individually to their specifications. Before integrating the motion system with the simulator cockpit and visual display, the hardware dynamic characteristics should be measured and documented,<sup>(55)</sup> using dummy loads which represent the weight, c.g. and moments of inertia of the simulator cockpit and visual display device(s).

The computer-simulator interface which consists of input-output (I/O) processors, analogue to digital and digital to analogue converters, connects the flight simulator components with the digital computer. Before these connections are made, the interface is tested, using the digital computer, by running a test program which uses input channels to read output channels (i.e. outputs are directly connected to inputs). After completion of these tests, the interface is linked to the flight simulator components and integrated testing of these components may start, using the digital computer.

Now, the digital computer can drive the flight instruments, visual simulation system and the motion generation system. The calibration of these components can be performed by implementing the correct scale factors into the software, in order to achieve optimal correlation between computed and displayed parameter values.

After completion of the calibration, the real-time flight simulator software may be loaded into the digital computer and the flight simulator is ready for 'flight' testing, following the procedures as prescribed in the so-called 'Acceptance Test Manual' (ATM) (see Section 8.5).

## 8.2. APPROVAL TEST GUIDE (ATG)

For Phase II or III approval,<sup>(21)</sup> the FAA requests the flight simulator operator to provide an 'Approval Test Guide' (ATG) in order to objectively demonstrate that the flight simulator accurately duplicates the flight test data of the airplane to be simulated. The ATG describes a number of specific flight test maneuvers needed to compare the characteristic behavior of the actual airplane and its systems with that of the flight simulator. As an example, one out of many FAA Phase II ATG flight test maneuvers, performed during the Citation 500 flight test program<sup>(85)</sup> (see Section 5.5) is described below. The pertinent ATG maneuver concerns the Citation 500 'Dutch Roll Dynamics'. First, the initial airplane/flight conditions, like gross weight, total fuel, moments of inertia, indicated airspeed, engine speed and thrust, flap- and landing gear position, etc. are carefully documented. A list of recording details is added to the prescribed ATG maneuver. Parameters, to be digitally recorded against time during the maneuver, are e.g.:

- Control wheel position, aileron position, aileron trim deflection.
- Column position, elevator position, elevator trim deflection.
- Rudder pedal deflection, rudder position, rudder trim deflection.
- Roll angle, roll rate, roll acceleration.
- True heading angle, yaw rate, yaw acceleration.
- Side-slip angle, angle of attack, indicated airspeed, etc.

The 'Pilot Test Procedure' for the Dutch Roll Dynamics reads:<sup>(66)</sup>

- (1) Trim the airplane in straight and level flight at the prescribed initial conditions (e.g. yaw damper on).
- (2) Initiate the dutch roll oscillation by means of a symmetrical rudder pedal doublet of a magnitude so that the resultant roll angle excursions do not exceed  $\pm 20^\circ$ .
- (3) Use control column to maintain the initial pitch attitude.
- (4) Leave control wheel in its centered position.
- (5) Test terminates when the dutch roll oscillation damps out.
- (6) Repeat above steps (1)–(5) with the yaw damper switched off.

The *solid curves* of side-slip angle ( $\beta$ ) and yaw rate ( $r$ ) against time in Fig. 84 show a few results of this ATG flight test maneuver with yaw damper off. These airplane responses are used later for the 'Proof of Match' (see Section 8.4).

In the case of the Citation 500 ATG flight test program (Section 5.5), a total of 114 recordings of ATG maneuvers were made during 9 test flights, some results of which may be found in the solid curves of Figs 83–90.

### 8.3. COMPUTER GENERATED CHECKOUT (CGC)

Computer generated checkout data are intended to verify correct implementation in a digital computer of the real-time airplane model and data, e.g. the 'BEAVER' model as defined in Section 5.2.2. CGC data are defined as records of the airplane model developer's implementation, in his own engineering simulation, of that model and its associated numerical data. These records may be in the form of time histories, snapshot printout of simulation variables and graphical presentations of processed data (e.g. control column force versus position). Tests of the real-time simulation software should be sufficiently comprehensive to allow detailed scrutiny of the entire flight envelope of the simulated airplane, and of the effects of each element within the simulation. In the case of the Citation 500 mathematical model development in Section 5.5, CGC-data of the a priori models as well as of the final mathematical models were delivered to the simulator manufacturer. Since this checkout documentation may form the basis of the contractual acceptance testing by a simulator purchaser, it is critical that the relative revision levels of the various models are carefully controlled and documented.

### 8.4. PROOF OF MATCH (POM)

Proof of match data—as mentioned already in Section 5.5—compare the ATG flight test data of Section 8.2 with the performance and dynamics of the airplane engineering simulation. In this case the control inputs (control forces or displacements), recorded during the ATG flight tests, drive the engineering simulation. FAA Phase II flight simulator approval requires POM-data of all the ATG flight test maneuvers mentioned in Section 8.2. To this end, time selections were made of these maneuvers in order to generate POMs (Figs 83–90) of the most significant parts of the ATG-maneuvers. As an example, for the FAA Phase II approval of the Citation simulator, 50 maneuvers from the ATG data were selected for the POM of the aerodynamic model and engine model, 15 maneuvers for the POM of the flight controls model, 8 maneuvers for the POM of the landing gear model and 32 maneuvers for the integrated Citation 500 mathematical model.

In order to improve the environmental fidelity of flight simulators, POMs should also be produced of the visual and motion simulation systems. In the case of a motion system POM, the specific forces and angular accelerations, measured objectively in the aircraft-cockpit in flight, should be compared to the same quantities measured in the simulator-cockpit on top of the motion system. Also here, tolerances to be agreed upon, should be applied. Figure 105, see Section 7.3, may serve as an example of a motion system POM, which compares the longitudinal specific force, measured in the aircraft-cockpit, with that measured in the simulator-cockpit during an aborted take-off.

### 8.5. FLIGHT SIMULATOR CRITICAL MANEUVERS (FSCM)

After completion of the above POMs of the airplane mathematical model and data package, providing objective data on the model quality, subjective 'flight' testing of the simulator may start using the 'Acceptance Test Manual' (ATM). The ATM describes, on a step-by-step basis, all the tests applied to the simulator over the entire operational envelope of the simulated airplane, including ground handling, starting with a 'dead ship'. Usually a knowledgeable customer pilot performs these tests, which consist of flight performance checks (e.g. take-off rotation speeds, stabilizer speeds, stabilizer versus power settings for different gross weights and c.g., etc.) and reproduction of the ATG flight test maneuvers (Section 8.2).

Differences between the behavior of the actual airplane and the Phase II/III approved flight simulator representing it, however, may remain. Very often, the simulator will be more difficult to fly than the airplane, as a consequence of reduced environmental fidelity (Section 4.3), visual and motion constraints, time delays etc. As a result, pilot performance for some maneuvers in the simulator may be inferior relative to the performance for the same maneuvers in real flight. The most demanding of those maneuvers, which tax both the pilot and the simulator to the utmost, may be called: 'Flight Simulator Critical Maneuvers'. Clearly, the exact type and shape of the critical maneuvers depend on the application and task of a particular flight simulator. Obviously the objective fidelity of the simulator will be compromised, during these maneuvers.

An important application of Flight Simulator Critical Maneuvers (FSCM) could be the approval of flight simulators to perform specific tasks.<sup>(21)</sup> Flight simulator operators should identify the most appropriate FSCMs for their particular simulator and task, so these FSCMs can be used to optimize the simulator characteristics for maximum perceptual fidelity. Suitably chosen and agreed FSCMs could also be used as basic input maneuvers in the Approval Test Guide (ATG, Section 8.2) for a particular flight simulator.

Examples of FSCMs for airline training simulators could be:

- outboard engine failure during take-off, just before and after V1,
- side-step maneuver in the final approach to landing (Fig. 106),
- turns, in the air as well as on the ground during taxi,
- go around with one engine failed,
- accelerated stop (aborted take-off),
- flare and touchdown.

## 9. CONCLUDING REMARKS

Real-time flight simulation technology has reached the level, where the aircraft performance and dynamics in the air, as well as on the ground, can be simulated with the fidelity, required for 'Total Simulation'. Prerequisites to reach this fidelity are:

- A well developed data base of the airplane performance and handling characteristics.
- An extensive airplane mathematical model, wherein the database fits.
- Sufficient computer power to satisfy the required computational duty cycle as a function of airplane natural frequency.
- Adequate objective fidelity inside the simulator cockpit to represent the character and workload of the pilot's task as it is in flight.
- A visual simulation system, which has sufficient scene content, resolution, update rate and an adequate collimated field of view.
- A complete motion generation system, optimized for maximum perceptual fidelity.
- Maximum latency, in particular for motion cue generation, less than 50 msec.

Future research efforts in the area of flight simulation techniques should encompass the following topics:

- Minimum essential visual and motion cueing requirements for a particular flying mission.
- Microprocessor architectures.

- Airplane ground handling.
- Real-time rotorcraft simulation, in particular rotor modelling and the interaction between main rotor, fuselage and tail rotor.
- Flexibility of large airplanes and the interaction with atmospheric turbulence and wind shear.
- CGI daylight visual systems, producing more scene content (up to a million luminance transitions), a resolution of 1 arc min, and a refresh/update rate of 60 Hz.
- Definition of flight simulator critical maneuvers for particular simulator applications and tasks.
- The application of ADA in real-time flight simulation, to provide machine independent, low life-cycle-cost flight simulation software.

Future improvements in flight simulation technology will be used to make simulation better or to make it cost less. The appearance of 'low cost' flight simulators may open new markets, such as general aviation training.

## ACKNOWLEDGEMENTS

The author would like to thank Prof. Otto H. Gerlach of Delft University of Technology and Mr Nico van Dam of the National Aerospace Laboratory for reading the manuscript, and for their valuable advice and discussions during the preparation of this review.

## REFERENCES

1. ADRIAN, P., STAYNES, W. N. and BOLTON, M. (1979) The evolution of the flight simulator. In: *50 Years of Flight Simulation*, Conf. Proc., Session 1, pp. 1-23, The Royal Aeronautical Society, London.
2. ANON. (1919) Article on Gabardini in *Janes Aircr.* 386.
3. ANON. (1942) *Illustrated Catalogue of Synthetic Training Devices*, Directorate of Operational Training, Air Ministry, London (Public Record Office ref. AIR 20/6058).
4. ANON. (1945) *Notes on the History of RAF Training 1939-1944*, Air Ministry, Air Member for Training, London (Public Record Office ref. AIR 20/1347).
5. BAARSPUL, M. and DOOREN, J. P. VAN (1976) The Hybrid simulation of aircraft motions in a piloted moving-base flight simulator, Rept. VTH-178, Delft University of Technology, Delft, The Netherlands.
6. BILLING, E. (1910) An improved machine for teaching the art of flying without leaving the ground, *Br. Pat. Spec. 16773*.
7. BLOK, P. (1976) Das hydrostatische keilspaltlager (conical hydrostatic Bearings), Thesis, Delft University of Technology, Delft, The Netherlands.
8. DEHMEL, R. C. (1941) *U.S. Pat. 2,494,508, 2,366,603*.
9. DUMMER, G. W. A. (1945) Monograph on radar synthetic training devices (6 Vols).
10. ELSON, B. M. (1967) Colour TV generated by computer to evaluate spaceborne systems, *Aviat. Week and Space Technol.*, October 30, 78-82.
11. FLOREZ, L. DE (1949) Synthetic aircraft, *Aeronaut. Eng. Rev.* 26-29.
12. HELLINGS, G. and EMMS, E. T. (1960) A visual system for flight simulators, *Br. Commun. Electron.* 7 (5) 334-337.
13. HILL, N. and GUILLENCHMIDT, P. DE (1955) The possibility of the flight simulator as a training aid to helicopter pilots, *J. Helicopter Assoc. Great Britain* 8 (4), 133-157.
14. KELLY, L. L. (1970) as told to R. B. Parke, The Pilot Maker, Grosset and Dunlap, New York.
15. LINK, E. A., JR. (1930) Combination Training Device for Student Aviators and Student Entertainment Apparatus, *U.S. Pat. Spec. 1,825,462*.
16. MAISEL, A. Q. (1944) They bombed Berlin in Binghamton, *Reader's Digest*, 45, 46.
17. MURRAY, F. J. (1971) Training devices computing systems, *Naval Training Device Center 25th Anniversary Commemorative Tech. J.*, 221-230, Naval Training Device Center, Orlando, Florida.
18. SHOHAT, M. (1975) From submarine to satellite. Diverse applications for digital image generation techniques. In: *8th Naval Training Equipment Center/Industry Conf. Proc.*, pp. 173-182, Orlando, Florida.
19. VIERNSMA, T. J. (1980) *Analysis, Synthesis and Design of Hydraulic Servosystems and Pipelines*, Elsevier, Amsterdam.
20. VIERNSMA, T. J. and BAARSPUL, M. (1980) Development and application of a moving-base visual flight simulator, including the design of hydraulic actuators with hydrostatic bearings. In: *ICAS-80-9.2, 12th Congr. Int. Council Aeronaut. Sci.*, Munich, F.R.G.
21. ANON. Federal Aviation Administration (FAA), Advisory Circular AC No: 120-40A (draft) on Airplane Simulator and Visual System Evaluation, US Department of Transportation, U.S.A.
22. BLATT, P. E. and GUM, D. R. (1985) Trends in ground-based and in-flight simulators for development applications. In: *AGARD Conf. Proc. No. 408 on 'Flight Simulation'*, Cambridge, U.K.
23. BUHRMAN, J. (1984) Future requirements for airborne simulation, AGARD Adv. Rept. No. 188, North Atlantic Treaty Organization.

24. FACONTI, V. (1979) Evolution of flight simulator instructional capabilities: The first fifty years. In: *50 Years of Flight Simulation*, Conf. Proc., Session 2, pp. 51–74, The Royal Aeronautical Society, London, U.K.
25. HANKE, C. R. (1971) The simulation of a large jet transport aircraft, Vol. I: Mathematical model, NASA CR-1756.
26. HANKE, C. R. and NORDWALL, D. R. (1970) The simulation of a jumbo jet transport aircraft, Vol. II: Modeling Data, NASA CR-114494.
27. HANKE, D. and LANGE, H. H. (1988) Flight evaluation of the ATTAS digital fly-by-wire/light flight control system. In: *ICAS-88-3.6.1, 16th Congr. Int. Council Aeronaut. Sci.*, Jerusalem, Israel.
28. HANKE, D. and BROUWER, G. (1985) DFVLR in-flight simulators ATTAS and ATTHEES for flying qualities and flight control research. In: *AGARD Conf. Proc. No. 408*, pp. 23.1–23.13, North Atlantic Treaty Organization.
29. JANSEN, C. J. (1988) Present and future developments of the NLR moving base research flight simulator. In: *AIAA Flight Simulation Technologies Conf.*, Pap. 88-4584-CP, Proc. CP 8812, The American Institute of Aeronautics and Astronautics, Atlanta, Georgia, U.S.A.
30. JUSTIZ, C. R. and PATEL, S. M. (1988) NASA Shuttle Training Aircraft Flight Simulation Overview. In: *AIAA Flight Simulation Technologies Conf.*, Pap. 88-4608-CP, Proc. CP 8812, pp. 182–190, The American Institute of Aeronautics and Astronautics, Atlanta, Georgia, U.S.A.
31. KNOTTS, L. H. and BAILEY, R. E. (1988) Ground Simulator Requirements Based on In-Flight Simulation. In: *AIAA Flight Simulation Technologies Conf.*, Pap. 88-4609-CP, Proc. CP 8812, pp. 191–197, The American Institute of Aeronautics and Astronautics, Atlanta, Georgia, U.S.A.
32. LEYMAN, C. S. (1986) A review of the technical development of Concorde, *Progr. Aerosp. Sci.* **23**, 185–238.
33. MARKMAN, S. R. (1985) Capabilities of airborne and ground based flight simulation, *SAE Pap. 851944*, Society of Automotive Engineers.
34. NICHOLAS, O. P., GILES, J. A. and WILLIAMS, D. A. (1985) Development of in-flight simulation aircraft for research and training in U.K. In: *AGARD Conf. Proc. No. 408 on 'Flight Simulation'*, pp. 24.1–24.13, North Atlantic Treaty Organization.
35. REID, L. D. and NAHON, M. A. (1988) Response of airline pilots to variations in flight simulator motion algorithms, *J. Aircr.* **25**, (7), 639–646.
36. ROLFE, J. M. and STAPLES, K. J., eds (1986) *Flight Simulation*, Cambridge Aerospace Series, Cambridge University Press, Cambridge, U.K.
37. SKANS, N. S. and BARNES, A. G. (1979) Fifty years of success and failure in flight simulation. In: *50 Years of Flight Simulation*, Conf. Proc., Session 1, pp. 33–49, The Royal Aeronautical Society, London, U.K.
38. SNYDER, C. T., BRAY, R. S., DRINKWATER III, F. J. and FORREST, R. D. (1971) Simulation studies for development of certification criteria applicable to SST takeoff. In: *Proc. NASA Safety and Operating Problems Conf.*, NASA SP-270, Vol. 1, pp. 277–290, Hampton, Virginia, U.S.A.
39. SPITZER, R. E., RUMSEY, P. C. and QUIGLEY, H. C. (1972) Use of the flight simulator in the design of a STOL research airplane. In: *Proc. AIAA 4th Conf. Aircraft Design, Flight Tests and Operations*, Los Angeles, California, U.S.A.
40. TOMLINSON, B. N. (1986) Motion software for a research flight simulator. In: *Advances in Flight Simulation—Visual and Motion Systems*, Int. Conf. Proc., pp. 64–80, The Royal Aeronautical Society, London, U.K.
41. ABBINK, F. J. and PIJPERS, E. W. (1985) Trends in airliner flight deck design, Rept. NLR MP 85007U, National Aerospace Laboratory NLR, The Netherlands.
42. ANON.—AERONAUTICAL RADIO, INC.—(1986) Guidance for design and integration of aircraft avionics equipment in simulators, Draft 1 of Project Paper 610, prepared for AEEC.
43. ANON.—AGARD—(1984) Report of the working group on large-scale computing in aeronautics, AGARD Advisory Rept. No. 209, North Atlantic Treaty Organization.
44. ANON.—IATA—(1986) Flight simulator design and performance data requirements (final draft of proposed revision A, 01 February 1986).
45. BAARSPUL, M., MULDER, J. A., NIEUWPOORT, A. M. H. and BREEMAN, J. H. (1988) Mathematical model identification for flight simulation, based on flight and taxi tests. In: *Flight Simulation—Recent Developments in Technology and Use*, Int. Conf. Proc., The Royal Aeronautical Society, London, 12 and 13 April 1988.
46. BARBER, B. (1986) AOI displays using laser illumination. In: *Advances in Flight Simulation—Visual and Motion Systems*, Int. Conf. Proc., The Royal Aeronautical Society, London, U.K.
47. BARNES, A. G. (1986) The integration of a six axes motion system and a wide angle visual system inside a dome. In: *Advances in Flight Simulation—Visual and Motion Systems*, Int. Conf. Proc., The Royal Aeronautical Society, London, U.K.
48. BOFF, K. R., KAUFMAN, L. and THOMAS, J. P., eds (1986) *Handbook of Perception and Human Performance*, Vol. I: *Sensory Processes and Perception*, John Wiley.
49. COOK, A. M. (1988) The helmet mounted visual display system in flight simulation. In: *Flight Simulation—Recent Developments in Technology and Use*, Int. Conf. Proc., The Royal Aeronautical Society, London, 12 and 13 April 1988.
50. CORT, A. and HAWTIN, R. (1984) Wide-angle, low altitude flight simulator vision system for cockpit research and aircrew training. In: *Tenth European Rotorcraft Forum*, The Hague, The Netherlands.
51. DAVIES, J. L. (1986) Considerations for FLIR simulation in pilot training. In: *Advances in Flight Simulation—Visual and Motion Systems*, Int. Conf. Proc., The Royal Aeronautical Society, London, U.K.
52. HOOGSTRATEN, J. A. and MOESDIJK, G. A. J. VAN DE (1983) Modular programming structure applied to the simulation of non-linear aircraft models. In: *IMACS Conf. Proc. 'Simulation in Engineering Sciences'*, Nantes, France.
53. HOLT, A. P., JR., NONEAKER, D. O. and WALTHOUR, L. (1980) A survey of new technology for cockpit application to 1990s transport aircraft simulators, NASA Contractor Rept. 159330, Lockheed-Georgia Company, Marietta, Georgia, U.S.A.
54. KEY, D. L. et al. (1980) Fidelity of simulation for pilot training, AGARD Advisory Rept. No. 159, North Atlantic Treaty Organization.

55. LEAN, D., GERLACH, O. H. et al. (1979) Dynamic characteristics of flight simulator motion systems, AGARD Advisory Rept. No. 144, North Atlantic Treaty Organization.
56. MULDER, J. A. (1987) Design and evaluation of dynamic flight test manoeuvres, Rept. LR-497, Delft University of Technology, Delft, The Netherlands.
57. MULDER, J. A. (1988) Aircraft flight control system identification. In: *Proc. 8th IFAC-IFORS Symp. Identification and System Parameter Estimation*, Beijing, China.
58. PARKINSON, D. (1988) Functionally distributed simulation. In: *Flight Simulation—Recent Developments in Technology and Use*, Int. Conf. Proc., The Royal Aeronautical Society, London, 12 and 13 April 1988.
59. STATLER, I. C. et al. (1981) Characteristics of flight simulator visual systems, AGARD Advisory Rept. No. 164, North Atlantic Treaty Organization.
60. WALL, R. L., TATE, J. L. and MOSS, M. J. (1980) Advanced flight deck/crew system functional requirements, NASA Contractor Rept. 159330, Lockheed-Georgia Company, Marietta, Georgia, U.S.A.
61. WILLIAMS, L. (1985) Real time blade element rotor modelling. In: *Flight Simulation of Helicopters—Status and Prospects*. Int. Conf. Proc., pp. 17–30, The Royal Aeronautical Society, London, U.K.
62. ANON.—AGARD—(1975) Approach and Landing Simulation, AGARD Rept. No. 632, North Atlantic Treaty Organization.
63. ANON. (1960) *Handbook of Geophysics, USAF Air Research and Development Command*, McMillan, New York.
64. ANON. (1970) Airworthiness requirements for automatic landing in restricted visibility down to Category III, British Civil Airworthiness Requirements Pap. No. 367, Issue 3.
65. ANON. (1986) *Cessna Model 500 and 501 Citation. Weight and Balance Manual*, Revision 20, Cessna Aircraft Company 500WB20.
66. ANON. (1987) Citation 500 aircraft pilot test procedures for FAA Phase II ATG manoeuvres, Revision 1, CAE Electronics Ltd, Montreal, Canada.
67. BARNES, A. G. and YAGER, T. J. (1985) Simulation of aircraft behavior on and close to the ground. AGARDograph No. 285, North Atlantic Treaty Organization.
68. BARNES, A. G. and KOIVISTO, C. J. (1981) Simulation of the landing approach and flare manoeuvre, LUTAB-R-3046.2.
69. BARNES, A. G., KOIVISTO, C. J., HOLM, G., HYDEN, A. and SUNDQVIST, R. (1982) Further simulation of the landing approach and flare manoeuvre, LUTAB-R-3046.3.
70. DRYDEN, H. L. (1961) A review of the statistical theory of turbulence. In: *Turbulence Classic Papers on Statistical Theory*, Interstate, New York.
71. ETKIN, B. (1972) *Dynamics of Atmospheric Flight*, John Wiley, New York.
72. EIJKHOF, P. (1974) *System Identification*, John Wiley, New York.
73. FROST, W., CROSBY, B. and CAMP, D. W. (1979) Flight through thunderstorm outflow, *J. Aircr.* **16** (11).
74. FROST, W., CHANG, H. P., McCARTHY, J. and ELMORE, K. L. (1984) Simulated flight through JAWS wind shear: In-depth analysis results. Pap. AIAA-84-0276.
75. GERLACH, O. H. (1983) Lecture notes on airplane stability and control I, Part II, Rept. LR-384-II, Delft University of Technology, Delft, The Netherlands.
76. GERLACH, O. H. (1966) Calculation of the response of an aircraft to random atmospheric turbulence. Part I: Symmetric motions. Rept. VTH-138, Delft University of Technology, Delft, The Netherlands.
77. GERLACH, O. H. and BAARSPUL, M. (1968) Calculation of the response of an aircraft to random atmospheric turbulence. Part II: Asymmetric motions. Rept. VTH-139, Delft University of Technology, Delft, The Netherlands.
78. IVAN, M. (1986) A ring-vortex downburst model for flight simulations, *J. Aircr.* **23** (3).
79. KURKOWSKI, R. L. et al. (1971) Development of turbulence and wind shear models for simulator applications. In: *NASA Aircraft Safety and Operating Problems Conf.*, NASA SP-270, National Aeronautics and Space Administration, Washington D.C., U.S.A.
80. LAPPE, O. U. (1965) A low altitude turbulence model for estimating gust loads on aircraft. In: *AIAA 2nd Aerosp. Sci. Meet.*, Pap. No. 65-14.
81. LUERS, J. K. (1973) A model of wind shear and turbulence in the surface boundary layer, NASA CR-2288, National Aeronautics and Space Administration, Washington D.C., U.S.A.
82. MOESDIJK, G. A. J. VAN DE (1975) The description of patchy atmospheric turbulence, based on a non-Gaussian simulation technique, Rept. VTH-192, Delft University of Technology, Delft, The Netherlands.
83. MOESDIJK, G. A. J. VAN DE (1978) Non-Gaussian structure of the simulated turbulent environment in piloted flight simulation, Memorandum M-304, Delft University of Technology, Delft, The Netherlands.
84. MULDER, J. A. and HOLLANDER, J. G. DEN (1981) Status of dynamic flight test technology—model identification for flight simulation, SAE Pap. No. 810597, Wichita, U.S.A.
85. NIEUWPOORT, A. M. H., BREEMAN, J. H., BAARSPUL, M. and MULDER, J. A. (1988) Phase II Flight Simulator Mathematical Model and Data-Package, Based on Flight Test and Simulation Techniques. In: *ICAS-88-19.2, 16th Congr. of Int. Council Aeronaut. Sci.*, Jerusalem, Israel.
86. REEVES, P. M. (1969) A non-Gaussian turbulence simulation, Air Force Flight Dynamics Tech. Rept. AFFDL-TR-69-67.
87. REEVES, P. M., JOPPA, R. G. and GANZER, V. M. (1976) A non-Gaussian model of continuous atmospheric turbulence for use in aircraft design, NASA CR-2639, National Aeronautics and Space Administration.
88. RUIJGROK, G. J. J. and PAASSEN, D. M. VAN (1987) Sound measurements of the Cessna Citation PH-CTE, Memorandum M-565, Delft University of Technology, Delft, The Netherlands.
89. SYNGE, J. L. and GRIFFITH, B. A. (1959) *Principles of Mechanics*, McGraw-Hill, New York.
90. TJEE, R. T. H. and MULDER, J. A. (1988) Stability and control derivatives of the De Havilland DHC-2 "BEAVER" aircraft, Rept. LR-556, Delft University of Technology, Delft, The Netherlands.
91. WAHI, M. K. and YOURKOWSKI, F. M. (1980) 757-200 crew training simulator-ground handling data, Boeing Commercial Airplane Company, Seattle, U.S.A.

92. ZOERB, M. C. et al. (1976) Landing gear ground handling mathematical models and data for flight training simulators (B707, 727, 737, 747), Boeing Doc. No. D6-44062.
93. BARNES, A. G. (1988) User requirements in research and development simulators. In: *Low Cost Visual Systems*, Conf., The Royal Aeronautical Society, London, U.K.
94. BROWN, P. K. and WALD, G. (1964) Visual pigments in single rods and cones of the human retina, *Science* **144**, 145–151.
95. BUFFET, A. R. (1986) Visual cueing requirements in flight simulation. In: *Advances in Flight Simulation—Visual and Motion Systems*, Int. Conf. Proc., The Royal Aeronautical Society, London, U.K.
96. COHEN, R. W., GOROG, I. and CARLSON, C. R. (1975) Image descriptors for displays, Office of Naval Research Tech. Rept. AD A007585, Arlington, Va.
97. FARRELL, R. J. and BOTH, J. M. (1975) *Design Handbook for Imagery Interpretation Equipment*, Boeing Aerospace Company, D180-19063-1.
98. WEBB, P., ed. (1964) Bioastronautics Data Book, NASA SP-3006, National Aeronautics and Space Administration.
99. BAARSPUL, M., HOSMAN, R. J. A. W. and VAART, J. C. VAN DER (1986) Some fundamentals of simulator cockpit motion generation. In: *Advances in Flight Simulation—Visual and Motion Systems*, Int. Conf. Proc., The Royal Aeronautical Society, London, U.K.
100. BAARSPUL, M. (1977) The generation of motion cues on a six-degrees-of-freedom motion system, Rept. LR-248, Delft University of Technology, Delft, The Netherlands.
101. BRAY, R. S. (1985) Visual and motion cueing in helicopter simulation. In: *AGARD Conference Proceedings No. 408 on 'Flight Simulation'*, Cambridge, U.K.
102. BUSSOLARI, S. R., SULLIVAN, R. B. and YOUNG, L. R. (1986) Vestibular models for design and evaluation of flight simulator motion. In: *Advances in Flight Simulation—Visual and Motion Systems*, Int. Conf. Proc., The Royal Aeronautical Society, London, U.K.
103. DIEUDONNE, J. E., PARRISH, R. V. and BARDUSCH, R. E. (1972) An actuator extension transformation for a motion simulator and an inverse transformation applying Newton–Raphson's Method, *NASA TN D-7067*.
104. GERLACH, O. H. (1980) The biomorphic model of the human pilot, Rept. LR-310, Delft University of Technology, Delft, The Netherlands.
105. HOSMAN, R. J. A. W. and VAART, J. C. VAN DER (1978) Vestibular models and thresholds of human perception. Results of tests in a flight simulator, Rept. LR-265, Delft University of Technology, Delft, The Netherlands.
106. HOSMAN, R. J. A. W. and VAART, J. C. VAN DER (1985) Motion cues: The influence on manual flight control. In: *Flight Simulation of Helicopters, Status and Prospects*, Int. Conf. Proc., The Royal Aeronautical Society, London, U.K.
107. PARRISH, R. V., DIEUDONNE, J. E., BOWLES, R. L. and MARTIN, D. J. JR. (1975) Coordinated adaptive washout for motion simulators. *J. Aircr.* **12**, 1, 44–50.
108. PARRISH, R. V., DIEUDONNE, J. E. and MARTIN, D. J. JR. (1973) Motion software for a synergistic six-degree-of-freedom motion base, *NASA TN D-7350*.
109. REID, L. D. and NAHON, M. A. (1985, 1986) Flight simulation motion-base drive algorithms: Part 1—Developing and testing the equations, UTIAS Rept. No. 296, CN ISSN 0082-5255; Part 2—Selecting the system parameters, UTIAS Rept. No. 307, CN ISSN 0082-5255; Part 3—Pilot evaluations, UTIAS Rept. No. 319, CN ISSN 0082-5255, Institute for Aerospace Studies, University of Toronto, Canada.